

A Numerical and Experimental Study of Flow and Heat Transfer from a Flush, Inclined Film Cooling Slot

By

David M. Sinitin

B.A.Sc., (Mechanical Engineering), The University of British Columbia, 1983

A Thesis Submitted in Partial Fulfillment

of the Requirements for the degree of

Master of Applied Science

in

The Faculty of Graduate Studies
(Mechanical Engineering)

We accept this thesis as conforming

to the required standard

The University of British Columbia

October 1988

© David Murray Sinitin, 1988

In presenting this thesis in partial fulfilment of the requirements for an advanced degree at the University of British Columbia, I agree that the Library shall make it freely available for reference and study. I further agree that permission for extensive copying of this thesis for scholarly purposes may be granted by the head of my department or by his or her representatives. It is understood that copying or publication of this thesis for financial gain shall not be allowed without my written permission.

Department of MECHANICAL ENGINEERING

The University of British Columbia
Vancouver, Canada

Date APRIL 6, 1989

Abstract

Numerical and experimental results are presented for a simple, two dimensional flow from a flush, inclined slot in a flat plate. The geometry and mass flow conditions represent film cooling flows issuing from flush, inclined slots. The numerical velocity field predictions compare favourably with detailed flow measurements. Preliminary calculations of the heat transfer downstream of injection are also presented. Work done subsequent to this thesis indicates that the slot flow rate calibration may have been incorrect by 13 percent during the experiments. No correction for this possibility has been made here but a change, if made, would reduce the measured mass flow rates by 13 percent and would probably improve the agreement between measured and calculated velocity distributions.

Experimental observations and measurements indicate that the velocity of the flow exiting the slot is non-uniform in both magnitude and direction. The variation of flow direction in the slot could not be measured in this study. Consequently, several assumed distributions are used to elucidate the effect of flow angle variation on film cooling performance. The flow field is shown to be essentially insensitive to the non-uniformities in magnitude and direction of the slot flow. However, the predictions of wall shear stress and wall heat transfer downstream of injection are significantly affected by the non-uniformities in the slot. Differences of 80 to 100 percent are predicted depending on the flow angle distribution. These effects are shown to be most significant within 40 slot widths of the slot.

The results presented here may have important implications in prediction of the performance of various film cooling schemes. Furthermore, they point to a need for detailed flow measurements within and near modern film cooling orifices.

TABLE OF CONTENTS

	page
ABSTRACT	ii
LIST OF TABLES	v
LIST OF FIGURES	vi
NOMENCLATURE	x
1.0 INTRODUCTION	1
1.1 Background Information	1
1.2 Previous Work	3
1.2.1 Experimental	4
1.2.2 Numerical & Theoretical	6
1.3 Purpose and Scope of the Present Work	7
2.0 EXPERIMENTAL INVESTIGATION	8
2.1 Apparatus	8
2.1.1 Wind Tunnel Facility	8
2.1.2 Instrumentation & Measurement Techniques	11
2.1.2.1 Velocity & Turbulent Intensity	13
2.1.2.2 Temperature	17
2.1.2.3 Plenum Mass Flow Rate	17
2.1.2.4 Static Pressure	18
2.1.2.5 Hot Wire Probe Position	20
2.1.3 Experimental Models	20
2.2 Experimental Procedures	23
2.2.1 Velocity & Turbulent Intensity Profiles	23
2.2.2 Two Dimensionality of the Flow	25
2.3 Typical Experimental Results	27
2.3.1 Two Dimensionality Tests	27
2.3.2 Mean Velocity Profiles	29
2.3.3 Mass Flow Verification	38
2.3.4 Flow Visualization	41

3.0 NUMERICAL INVESTIGATION	44
3.1 Background	44
3.2 Problem Definition	51
3.2.1 The Heated Flat Plate	51
3.2.2 The Flush, Inclined Slot	54
3.2.3 The Plenum-Mainstream Interaction	59
3.3 Method of Solution	59
3.3.1 Main Features of the Computer Code	61
3.3.2 Grid Selection	64
4.0 COMPARISON OF RESULTS	69
4.1 The Flat Plate	69
4.1.1 Laminar Flow & Heat Transfer	70
4.1.2 Turbulent Flow & Heat Transfer	70
4.2 The Flush, Inclined Slot	79
4.2.1 The Flow Field	80
4.2.2 The Thermal Field	98
4.3 The Plenum-Mainstream Interaction	103
5.0 CONCLUSIONS	109
6.0 RECOMMENDATIONS	112
REFERENCES	114
APPENDIX A. Reproduction of Table 4.1 for Easy Cross-reference of Cases	119

LIST OF TABLES

	page
2.1 Hot Wire Calibration Constants for Two Probe Inclinations	16
2.2 Experimental Conditions	29
3.1 Empirical Constants Used in the Standard k- ϵ Turbulence Model	50
4.1 Tabulation of Various Flow Cases Used to Study the Flow, and Sensitivity of the Flow, to the Flow Angle Distribution in the Slot	80
4.2 Table of Values of β_{\max} in the Linear-Uniform Flow Angle Distribution	89
4.3 Table of Values of β_{\max} in the Linear-Uniform-Linear Flow Angle Distribution	89
A.1 Reproduction of Table 4.1 for Easy Cross-Reference of Cases	120

LIST OF FIGURES

		page
1.1	Illustration of Film Cooling	2
2.1	Wind Tunnel Schematic	9
2.2	Photograph of the Plenum Module	10
2.3	Photograph of the Experimental Setup	12
2.4	Hot Wire Probe Orientations	15
2.5	Schematic of Pressure Instrumentation Reproduced with Permission of ref. [36]	19
2.6	Plates for the 20 Degree Slot Experiments	21
2.7	Plates for the 40 Degree Slot Experiments	22
2.8	Streamwise Locations of Velocity Profiles	24
2.9	Locations of the Two Dimensionality Measurements	26
2.10	Mean Velocity and Speed Profiles for $\alpha = 20$ Degrees and $M = 0.90$ a) upstream and b) across the slot	28
2.11	Mean Speed Profiles for 5 Streamwise Locations, $M = 0.5$ and x/s Measured from the Slot Leading Edge	30
2.12	Mean Speed Profiles For 5 Streamwise Locations, $M = 0.9$ and x/s Measured from the Slot Leading Edge	31
2.13	Mean Speed Profiles For 5 Streamwise Locations, $M \cong 1.3$ and x/s Measured from the Slot Leading Edge	32
2.14	Surface Pressure Coefficients for $\alpha = 20$ Degrees	35
2.15	Slot Mean Speed Profiles for $\alpha = 20$ Degrees	36
2.16	Slot Mean Speed Profiles for $\alpha = 40$ Degrees	37
2.17	Slot Velocity Profile Integrations for $\alpha = 20$ and 40 Degrees	39
2.18	Illustration of Flow Visualization with Smoke	42
2.19	Ink Smear Pattern from the Oil of Wintergreen Visualization	43

	page
3.1 Flow Domain for the Heated Flat Plate Problem	52
3.2 Flow Domain for the Flush, Inclined Slot Problem	55
3.3 Various Schemes Used for the Angular Variation in the Slot (a) Uniform, (b) Linear-Uniform, (c) Linear-Uniform-Linear; Note that $\beta_{\max} = \alpha$ for all case (a) calculations	57
3.4 Location of Points 'A' and 'B' for $\alpha = 40$ Degrees and $M = 0.91$	58
3.5 Flow Domain for the Plenum-Mainstream Interaction Problem	60
3.6 Relative Locations of the Staggered Grids and Calculated Variables	62
3.7 Typical Numerical Grid for the Heated Flat Plate Problem	65
3.8 Typical Numerical Grid for the Flush, Inclined Slot Problem	66
3.9 Typical Numerical Grid for the Plenum-Mainstream Interaction	67
3.10 Demonstration of Grid Independance for the Flush, Inclined Slot Problem	68
4.1 Laminar Boundary Layer Velocity and Temperature Profiles for $x/L = 0.50$	71
4.2 Turbulent Boundary Layer Mean Velocity Profiles for a) $x/L = 0.68$ and b) $x/L = 0.84$	73
4.3 Turbulent Boundary Layer Variation of Shear Stress Coefficient	75
4.4 Turbulent Boundary Layer Mean Temperature Profiles at a) $x/L = 0.68$ and b) $x/L = 0.84$	76
4.5 Turbulent Boundary Layer Variation of Stanton Number	78
4.6 Comparison of Experimental and Numerical Mean Speed Profiles at 5 Streamwise Positions, for Mass Flow Ratio of 0.5 and x/s Measured from the Slot Leading Edge	81

	page
4.7 Comparison of Experimental and Numerical Mean Speed Profiles at 5 Streamwise Positions, for Mass Flow Ratio of 0.9 and x/s Measured from the Slot Leading Edge	82
4.8 Comparison of Experimental and Numerical Mean Speed Profiles at 5 Streamwise Positions, for Mass Flow Ratio Near 1.3 and x/s Measured from the Slot Leading Edge	83
4.9 Surface Pressure Coefficients for a) the 20 Degree Slot and b) the 40 Degree Slot	86
4.10 Shear Stress Coefficients for a) the 20 Degree Slot and b) the 40 Degree Slot	87
4.11 Comparison of the Mean Speed Profiles at the Slot Trailing Edge for Three Flow Angle Distributions, $\alpha = 20$ Degrees and a) $M=0.46$, (case 201) and b) $M=1.4$, (case 203)	91
4.12 Comparison of the Mean Speed Profiles at the Slot Trailing Edge for Three Flow Angle Distributions, $\alpha = 40$ Degrees and a) $M = 0.46$, (case 401) b) $M = 1.2$, (case 403)	92
4.13 Comparison of Surface Pressure Coefficients for Three Flow Angle Distributions, $\alpha = 20$ Degrees and a) $M = 0.46$, (case 201) b) $M = 1.4$, (case 203)	94
4.14 Comparison of Surface Pressure Coefficients for Three Flow Angle Distributions, $\alpha = 40$ Degrees and a) $M = 0.46$, (case 401) b) $M = 1.2$, (case 403)	95
4.15 Comparison of Shear Stress Coefficients for Three Flow Angle Distributions, $\alpha = 20$ Degrees and a) $M = 0.46$, (case 201) b) $M = 1.4$, (case 203)	96
4.16 Comparison of Shear Stress Coefficients for Three Flow Angle Distributions, $\alpha = 40$ Degrees and a) $M = 0.46$, (case 401) b) $M = 1.2$, (case 403)	97
4.17 Typical Streamwise Development of the Temperature Profiles for a) $\alpha = 20$ Degrees and $M = 0.90$, (case 202-U) b) $\alpha = 40$ Degrees and $M = 0.91$, (case 402-U)	99

	page
4.18 Comparison of Temperature Profiles at the Slot Trailing Edge for a) $\alpha = 20$ Degrees and b) $\alpha = 40$ Degrees	100
4.19 Comparison of Stanton Number Variation for a) $\alpha = 20$ Degrees and b) $\alpha = 40$ Degrees	102
4.20 Comparison of Stanton Number Variation for Three Flow Angle Distributions for $\alpha = 40$ Degrees and a) $M = 0.46$, (case 401) b) $M = 1.2$, (case 403)	104
4.21 Vector Field Showing the Predicted Variation of Magnitude and Direction of the Velocity at the Interface	106
4.22 Predicted Speed Variation Across the Slot for Normal Injection and $M = 0.4$	107
4.23 Predicted Distribution of Flow Angle for Normal Injection and $M = 0.4$	108

NOMENCLATURE

Dimensional Quantities:

α	Slot Angle Relative to the Horizontal
β	Flow Angle in the Slot
$\delta_{.995}$	Momentum Boundary Layer Thickness
δ_{ij}	Kronecker Delta, (i,j = 1, 2, 3)
ϵ	Dissipation of Turbulent Kinetic Energy
ϕ	General Scalar Variable
Φ	Dissipation of Thermal Energy
η	Film Cooling Effectiveness
κ	Von Karman Constant
μ	Molecular Viscosity
μ_T	Turbulent (Eddy) Viscosity
ν	Kinematic Viscosity
ρ	Density
σ_k	Prandtl Number for Turbulent Kinetic Energy
σ_ϵ	Prandtl Number for Dissipation of Turbulent Kinetic Energy
T	General Stress Tensor
l	Dissipation Length Scale
c_p	Specific Heat Capacity
C_1, C_2, C_μ	Constants for the k - ϵ model
e	Internal Energy
f_b	Body Force per Unit Mass

q	Heat Flux per Unit Area
q_w	Wall Heat Flux
H, h	Enthalpy
L	Length of the Flow Domain
P, p	Pressure
S	Source Term
s	Slot Width
T	Temperature
T_{aw}	Adiabatic Wall Temperature
T_c	Temperature of the Slot Flow
T_f	Freestream Temperature
T_w	Wall Temperature
t	Time
U, u	Streamwise Velocity Component
U_f	Freestream Velocity
V, v	Cross-Stream Velocity Component
V_c	Mean Slot Speed
V	Total Velocity Vector
x	Streamwise Distance Measured from the Slot Leading Edge or the Plate Leading Edge
y	Vertical Distance Measured Normal to x

Non - Dimensional Quantities:

C_{fx}	Shear Stress Coefficient
Gr_x	Grashof Number

Nomenclature

xii

M	Mass Flow Ratio
Re_x	Reynolds Number
St_x	Stanton Number
y⁺	Nondimensional Vertical Distance from a Wall

Common Notation:

–	Time Averaged Quantity
num (subscript)	Numerical Calculation Result
expt (subscript)	Experimental Measurement

ACKNOWLEDGEMENT

This thesis could not have been successfully completed without the help of many people. At times, the amount of work seemed insurmountable. The unending support of my family and friends has been a great motivating force in the completion of this work. Their help has been and remains much appreciated.

Special thanks are due to my supervisors, Dr. Ian Gartshore and Dr. Martha Salcudean. Their guidance, insight and amiable nature have made this project a thoroughly enjoyable experience. Without Dr. Salcudean's financial assistance I would not have had the opportunity to participate in this project.

Special thanks are also due to Dr. Ned Djilali, Dr. Zia Abdullah and Dr. Peri Sabhapathy who have provided unfailing patience and advice. The numerical work in this thesis is largely the result of many of Ned's and Zia's suggestions.

The construction of the wind tunnel modifications and the experimental models was made easier by the helpful suggestions and work of Mr. Ed Abel and Mr. John Hoar. Mr. Shu Oshika has also been very instructive in the setup and use of the experimental apparatus and instrumentation.

1. INTRODUCTION

"Employ your time in improving yourself by other men's writings, so you shall come easily by what others have laboured hard for."

Socrates

1.1 Background

Film cooling is a technique that has long been used to protect surfaces exposed to hot external flows. This technique involves injection of coolant into the boundary layer developing on an exposed surface as illustrated in Figure 1.1.

The first documented research on this topic was produced by Koppers in 1944 [1,2]. Experimental research on film cooling seems to have peaked between 1965 and 1977; the first numerical predictions appeared about 1969 [3]. The majority of this research has been directed towards application in gas turbines where film cooling is used to protect components and improve performance. Film cooling also finds application in re-entry vehicles and rocket motors [4]. The present study is concerned with application of film cooling to gas turbine blades.

Film cooling is used to cool gas turbine blades because it allows a higher exhaust temperature and a longer component life. The higher exhaust temperature translates to higher power production [5]. Longer component life is obtained by removing, reducing or redistributing thermal strains in the highly stressed blades [6]. The individual cooling orifices promote these improvements in two ways. Firstly, the coolant passing through an orifice provides internal convective cooling of the component wall. Secondly, the

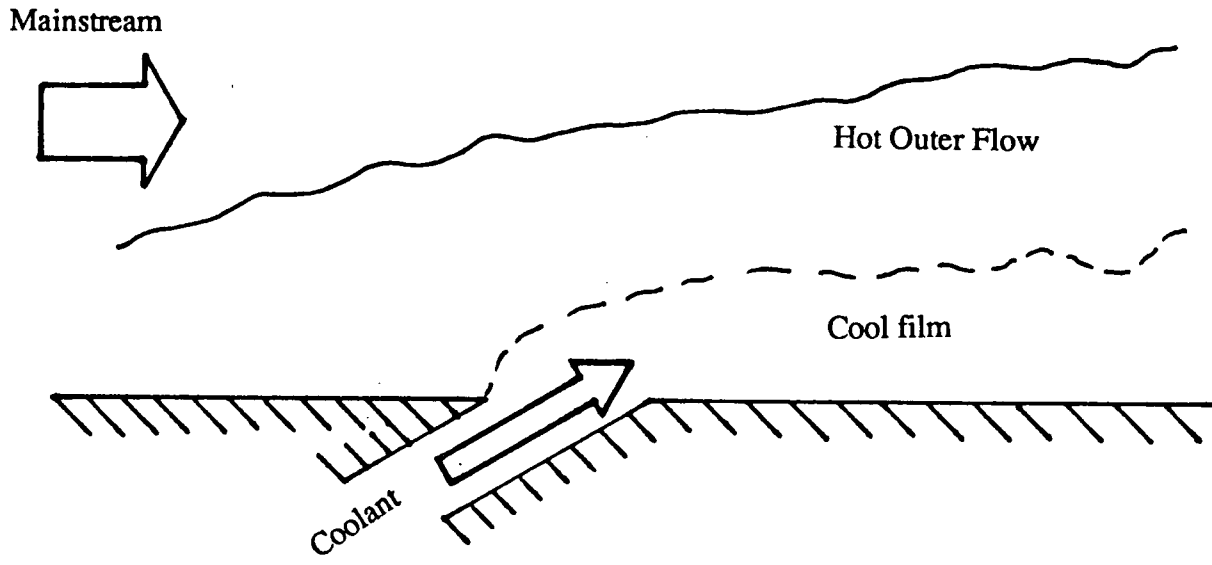


Figure 1.1 Illustration of film cooling

coolant distribution over the wall surface insulates the wall from the hot outer flow. Unfortunately film cooling orifices are also sources of stress concentrations and high cost. Thus a compromise must be reached where the minimum number of cooling orifices are used to provide maximum, uniform blade cooling.

In order to predict the thermal stresses in a turbine blade, designers must accurately predict the thermal boundary conditions surrounding the blade [4,6]. Accurate numerical prediction of this convective heat transfer boundary condition is the eventual goal of the present U.B.C. research program. Achievement of this goal is complicated by flow features like transition [7,8,9,10], strong pressure gradients [7,11,12], unsteady combustion, [6], large temperature differences [13,14,15], high turbulence levels [16,17,18], three dimensional flow [19,20,21,22,23], end wall effects [24], and separation [11].

The complexity of such a flow necessitates a stepwise elucidation of the film cooling process and its governing parameters. As a first step towards understanding and predicting film cooling behavior, the present study examines two dimensional flow ejected from a flush inclined slot. The flush, inclined slot geometry is chosen because it is the logical precursor of the flush, inclined, three dimensional orifice typically used in modern film cooling applications.

1.2 Previous Work

The competitive nature of the gas turbine industry precludes publication of many important findings. Unfortunately film cooling information, in particular, is carefully guarded. For this reason, the open literature may not be representative of the film cooling knowledge base.

1.2.1 Experimental Work

Goldstein [4] provides a critical, detailed review of film cooling research up to 1971. This review indicates that, except for the work of Sivasegaram and Whitelaw [25], Papell [26] and Metzger et al. [27,28], all work relating to cooling slots is done for normal, tangential or near tangential injection. Small variations of the injection slot geometry are found to have significant effects on film cooling, even far downstream of injection, i.e. $x/s > 40$. Goldstein [4] comprehensively summarizes these works and their empirical correlations of 'film cooling effectiveness'. Film cooling effectiveness, η , is defined as the ratio $(T_{aw} - T_f)/(T_c - T_f)$. This ratio is defined to allow a standard comparison of calculated or measured results for various injection schemes. In these correlations, the film cooling effectiveness, η , is correlated with the mass flow ratio, M , and the distance downstream of the slot, x/s . The mass flow ratio, M , is defined as the ratio $(\rho V)_c/(\rho U)_f$.

Sivasegaram and Whitelaw [25] report the effect of injection angle on film cooling effectiveness. Their work considers slot angles of 30, 60 and 90 degrees for mass flow ratios between 0.1 and 5. Sivasegaram and Whitelaw report that a larger injection angle produces significantly smaller film cooling effectiveness at any given downstream location. This behavior appears to be due to greater mixing of the main and secondary streams at the injection point. Increasing the mass flow ratio, for a given slot, is shown to increase the film cooling effectiveness at locations downstream of each slot. This latter effect only applies to mass flow ratios less than two. Increasing the mass flow ratio beyond two is shown to have little effect on the film cooling effectiveness. The results of Papell [26], and Metzger et al. [27,28] are in good, qualitative agreement with those of Sivasegaram and Whitelaw [25].

Metzger et al. [28] also provide correlations for the average heat transfer coefficient in the near region downstream of the slot, i.e. $x/s < 40$. Metzger emphasizes the downfalls associated with the common practice of predicting wall heat transfer using adiabatic wall temperature distributions. This point is important in the region immediately downstream of the injection location, which is the region of interest in most practical situations. In this region, the secondary fluid significantly alters the surface pressure distribution so the heat transfer can be increased or decreased depending on the strength and nature of injection.

Sivasegaram and Whitelaw [25] note that ",for a given injection angle, the detailed geometry of an angled slot is also likely to be an important parameter, especially if it results in a velocity profile at the slot exit which is asymmetric." For this reason, it is important to note that the experiments of references 25, 26, 27 and 28 use small slots which have length to width ratios of the order of 10. Also, the entrances to these slots are designed to minimize entrance effects on the flow in the slot. Such geometries do not realistically represent the geometries found in film cooled turbine blades.

Film cooling research is focussed on determination of film cooling effectiveness values and heat transfer coefficients. Surprisingly little work has been done to measure the flow field surrounding non-tangential injection slots. As with the majority of slot injection experiments, Metzger et al. [27,28], Papell [26] and Sivasegaram and Whitelaw [25] provide very little information regarding flow quantities such as streamwise velocity, temperature and turbulent intensity profiles. Similarly, very little, if any, information is given about the slot flow. Slot velocity, temperature and turbulent intensity profiles are not given. The state of flow development within the slot is not described, eg. it is not said whether the slot flow is fully developed. The lack of this critical flow field information makes the understanding and computation of flow from an inclined slot, difficult. The missing information also makes quantitative comparisons of

numerical and previous experimental results impossible.

The majority of film cooling works published since 1971 deal with discrete-hole cooling and full coverage film cooling. Full coverage film cooling is an extension of discrete-hole cooling where arrays of holes are used to cool the entire blade surface. These topics involve three dimensional orifice geometries and are considered more practical than two dimensional slots which cannot be used in gas turbine blades. Consequently, two dimensional film cooling slots have not been examined since 1971 except for tangential injection studies by Mayle, Kopper, Blair and Bailey [29], and Ko and Liu [30].

1.2.2 Numerical and Theoretical Work

The review article of Goldstein [4], presents several theoretical correlations for film cooling effectiveness. These results are obtained by assuming the secondary stream acts as a heat sink without altering the flow in the boundary layer. In general the correlations agree with experiment for small, impractical mass flow ratios, e.g. $M < 0.1$. Disagreement for larger mass flow ratios is presumably due to the failure of this assumption near the slot.

More recent work has focussed on the numerical solution of the mass, momentum and energy equations. Kacker, Pai and Whitelaw [3], successfully computed the behavior of various wall jet flows, e.g. tangentially injected flows. Bergeles, Gosman and Launder [31,32,33], Demuren, Rodi and Schonung [34] and Yavuzkurt, Moffat and Kays [35] have computed the three dimensional flows of discrete-hole cooling and full coverage film cooling with qualified success. Each of these numerical works have relied upon experimental results for boundary conditions.

A calculation of two dimensional film cooling from a flush inclined slot has not been reported. The lack of such a calculation is probably due to the lack of adequate

flow field measurements which are required for boundary conditions.

1.3 Purpose and Scope of the Present Investigation

The present study establishes a foundation from which further experimental and numerical film cooling studies can grow. To this end, the two dimensional, inclined slot geometry is chosen for study here. Understanding of the two dimensional film cooling behavior is a prerequisite for the understanding of more complicated three dimensional film cooling flows. The lack of experimental data and numerical computations are evidence of a real need for the results presented here.

The experimental investigation has two goals. The primary goal is to provide reliable data for comparison with computational results. The secondary goal is to gain a physical understanding of the flow.

The primary goal of the numerical investigation is to predict (compute) the turbulent flow and heat transfer for a fundamental film cooling arrangement. To this end, laminar and turbulent flat plate boundary layers are calculated as test cases of the computer code. The film cooling flow is calculated using experimental data for boundary conditions. A secondary goal of the numerical investigation is to develop an understanding of the experimentally observed interaction of the main and secondary streams at the point of injection. Neither a detailed discussion nor a calculation of this interaction is found in the literature.

2. EXPERIMENTAL INVESTIGATION

"Make your choice adventurous stranger. Strike the bell and bide the danger, or wonder 'til it drives you mad what would have followed if you had..."

Anonymous

The experiments described in this chapter provide detailed data previously unavailable in the open literature. Some of these data are used as boundary conditions for the computational investigation of injection from a flush, inclined slot. The remaining experimental data are used for comparison with the computational results and as a guide to understanding this complicated flow.

2.1 Apparatus

2.1.1 Wind Tunnel Facility

The experiments have been conducted at UBC in the low speed boundary layer wind tunnel. A schematic diagram of this blower type wind tunnel is shown in Figure 2.1. The wind tunnel has a test section 40.64 cm wide by 25.4 cm high by 4.01 m long. The blower is capable of producing airflow in the range of 1 m/s to 20 m/s.

The test section is lengthened for these experiments by the addition of a 97.79 cm long plenum module, shown in Figure 2.2. Lengthening of the test section required

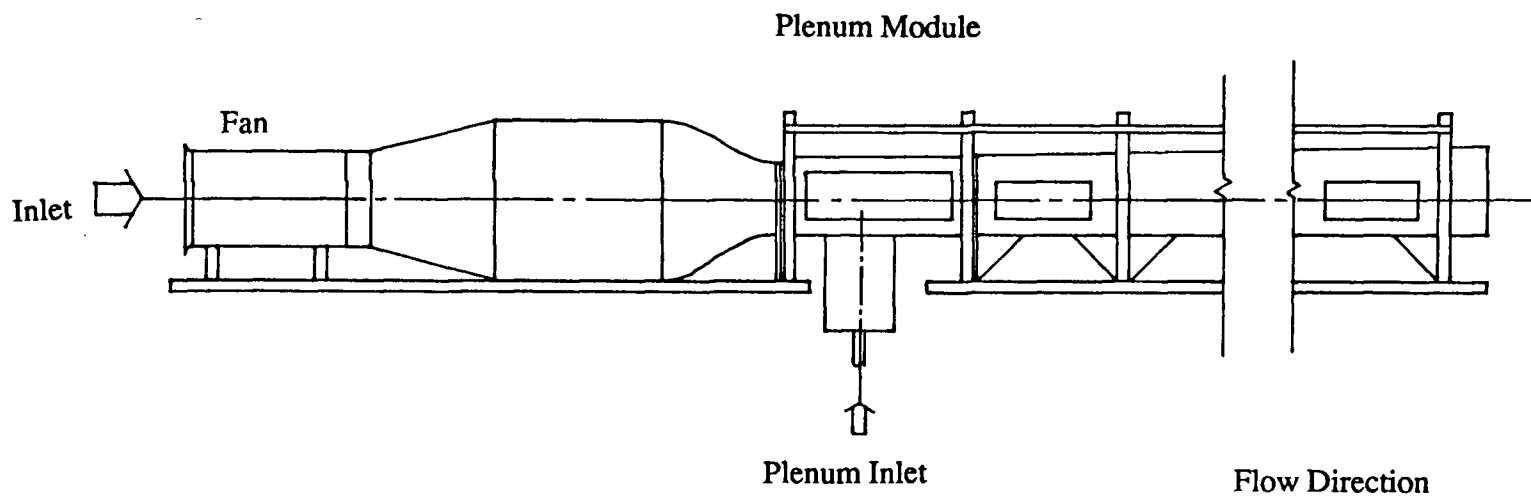


Figure 2.1 Wind tunnel schematic

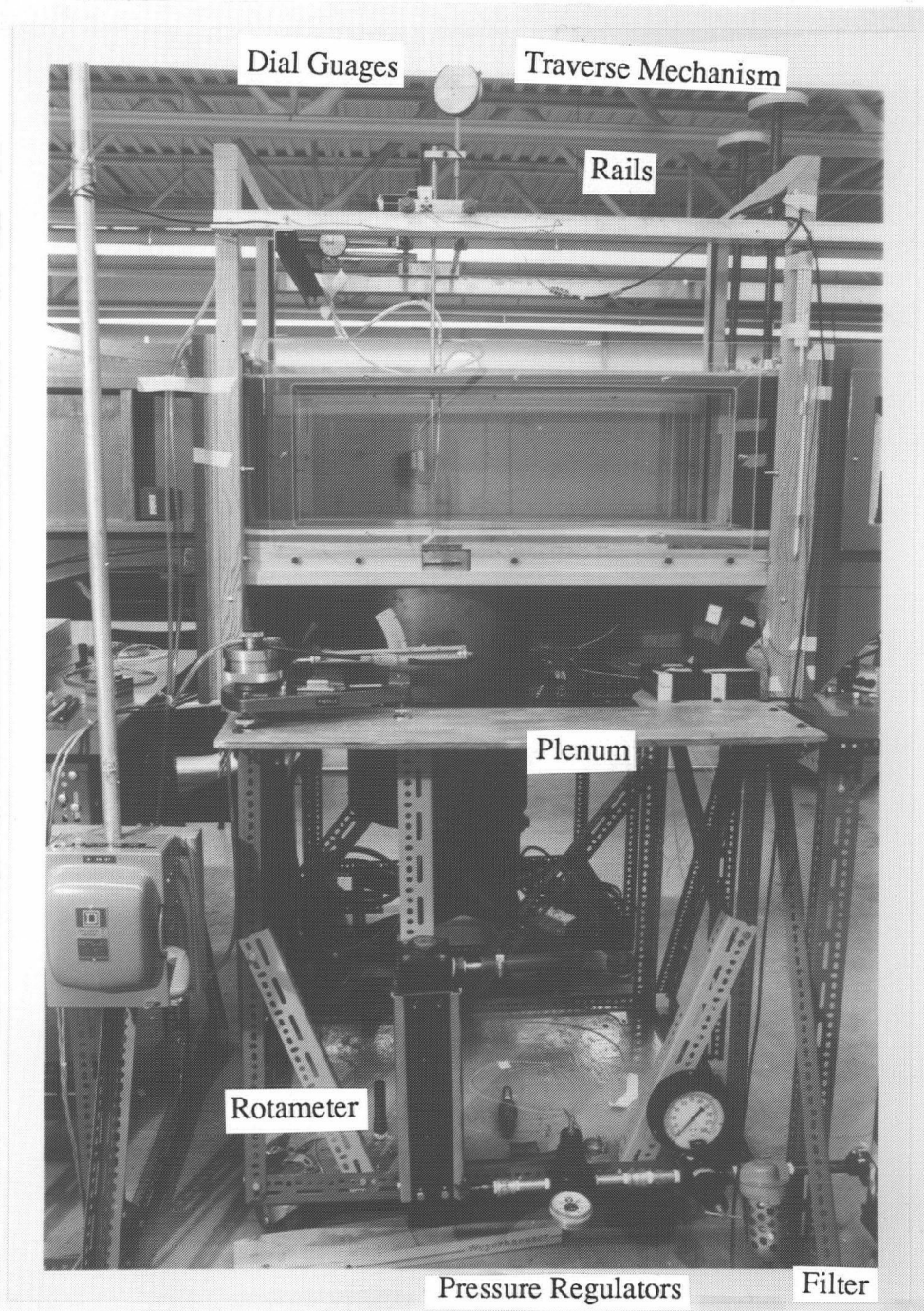


Figure 2.2 Photograph of the Plenum Module

installation of a new, full-length, adjustable wind tunnel roof. The roof adjustment allows imposition of various pressure gradients on the flow.

The plenum module facilitates controlled injection of a uniform secondary stream into the mainstream. The plenum floor is designed to accommodate a wide variety of slot and orifice geometries. The plenum air is supplied from the building's main air compressor. This compressor has a rated capacity of 250 scfm at 150 psi. Before reaching the plenum, the compressed air travels a long distance through piping, a condensing filter, two pressure regulators and a rotameter. The condensing filter removes water and oil from the compressed air. The two pressure regulators are used in series to reduce pressure fluctuations in the supply line. Flowrate fluctuations are less than ± 0.25 scfm at standard conditions. The rotameter is used to measure the mass flowrate of air into the plenum and therefore into the mainstream.

Above the wind tunnel roof are two rails which support the hot wire anemometer traverse mechanism. These rails, indicated in Figure 2.3, run the full length of the test section. The traverse mechanism is capable of movement in the longitudinal, lateral and vertical directions. Good quality bearings are used throughout the traverse mechanism to allow a positioning accuracy of ± 0.0127 mm in these 3 directions. Movement of the traverse mechanism is done by hand with the aid of two dial gauges, indicated in Figure 2.2. The wind tunnel roof has 3 streamwise slots, spaced equally across the span. These slots allow two-dimensionality checks at 3 spanwise positions.

2.1.2 Instrumentation and Measurement Techniques

The quantities measured in this study include temperature, mean flow velocity, turbulent intensity, static pressure, dynamic pressure, total pressure. These quantities

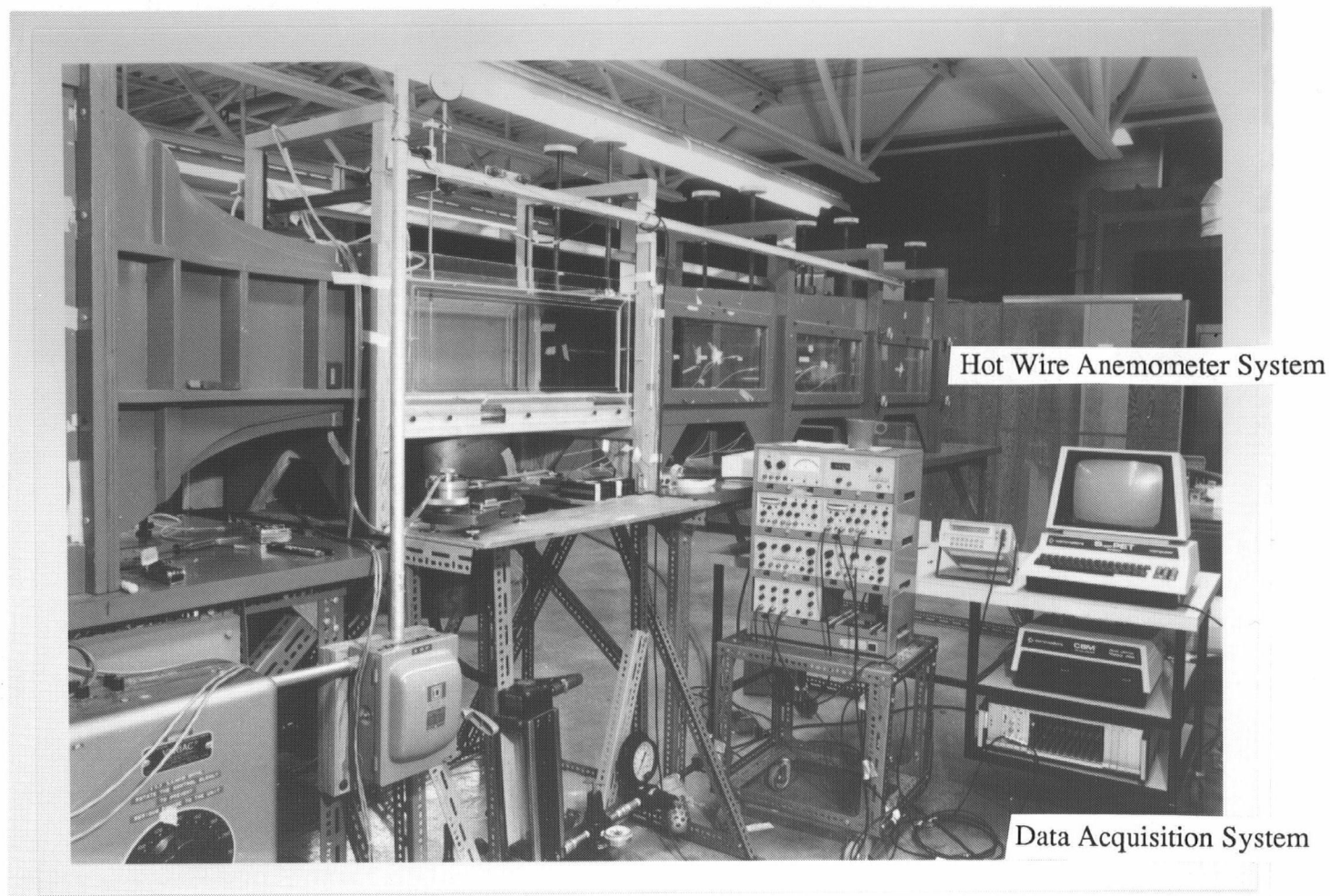


Figure 2.3 Photograph of the Experimental setup

were measured using a combination of digital and analog devices. A general outline of the techniques and equipment used follows.

2.1.2.1 Velocity and Turbulent Intensity

Velocity and turbulent intensity are the principal quantities measured in these experiments. The mean and fluctuating velocities are measured using a DISA constant temperature hot wire anemometer system, shown in Figure 2.3. This anemometer system is coupled with a microcomputer, also shown in Figure 2.3, to facilitate and improve data acquisition.

The hot-wire probes are standard DISA single wire probes. The wire itself is a $5\mu\text{m}$ diameter, 1.25 mm long platinum-coated tungsten filament. The DISA anemometer bridge is operated at an overheat ratio of 1.6. This ratio is 20 percent lower than the ratio recommended by DISA; the lower ratio allows a longer useful life of the wire.

The voltage signal, produced by the anemometer bridge, is passed through a 10 kHz low pass filter before reaching a 12 bit Microlink analog to digital convertor and a CBM Super PET microcomputer. The 10 kHz frequency was chosen to eliminate high frequency noise without affecting the lower frequency signal components.

The Microlink convertor contains an amplifier, A/D convertor and a power supply. The amplifier is adjusted so the incoming analog signal makes maximum use of the analog to digital converter's resolution. The Microlink convertor requires periodic calibration checks. These checks are done using a wave generator to produce various d.c. signals.

The CBM microcomputer receives the digital information from the Microlink and converts it to velocities and turbulent intensities using look-up tables generated during

hot-wire calibration. The look-up tables are generated using King's Law with an exponent of 0.45. In all measurements, a digital sampling frequency of 3 kHz is used to obtain 24000 samples. This sample frequency is limited by the hardware characteristics of the CBM-microlink system. Consequently, any frequency analyses of the data are only valid up to 1.5 kHz. Above 1.5 kHz, Nyquist's sampling criterion is not obeyed and aliasing becomes more likely. Fortunately frequency analysis is not used here so this problem does not arise.

The complete measuring system, described above, produces very reliable and repeatable results. Measurements of mean velocity are usually repeatable within 1.0 percent. Measurements of turbulent intensity are usually repeatable within 1.5 percent.

For a given set of test parameters, i.e. slot angle and mass flow ratio, eight streamwise velocity and turbulent intensity profiles are measured. The measuring system calibration is checked against a standard pitot tube before and after each series of profiles. If the measured mean velocity deviates from the pitot tube measurement by more than 2 percent, the system is recalibrated. Each profile consists of 35 to 50 measurements normal to the plate. The exception to this is the slot profile which consists of 39 to 81 points parallel to, and 0.127mm above, the plate surface. It should be noted that because of the complex nature of the flow at the slot opening, the hotwire measurements within, (and possibly near), the slot region only represent velocity magnitude, not the streamwise velocity component. Flow direction in this region must be measured, inferred or assumed from other observations.

A simple test has shown the hotwire calibration constants are negligibly affected by small changes in the direction of the mean flow approaching the wire. Two calibrations have been done with the hotwire probe oriented as shown in Figure 2.4. The King's law calibration constants obtained from these two orientations are listed in Table 2.1. These results confirm the ability of the

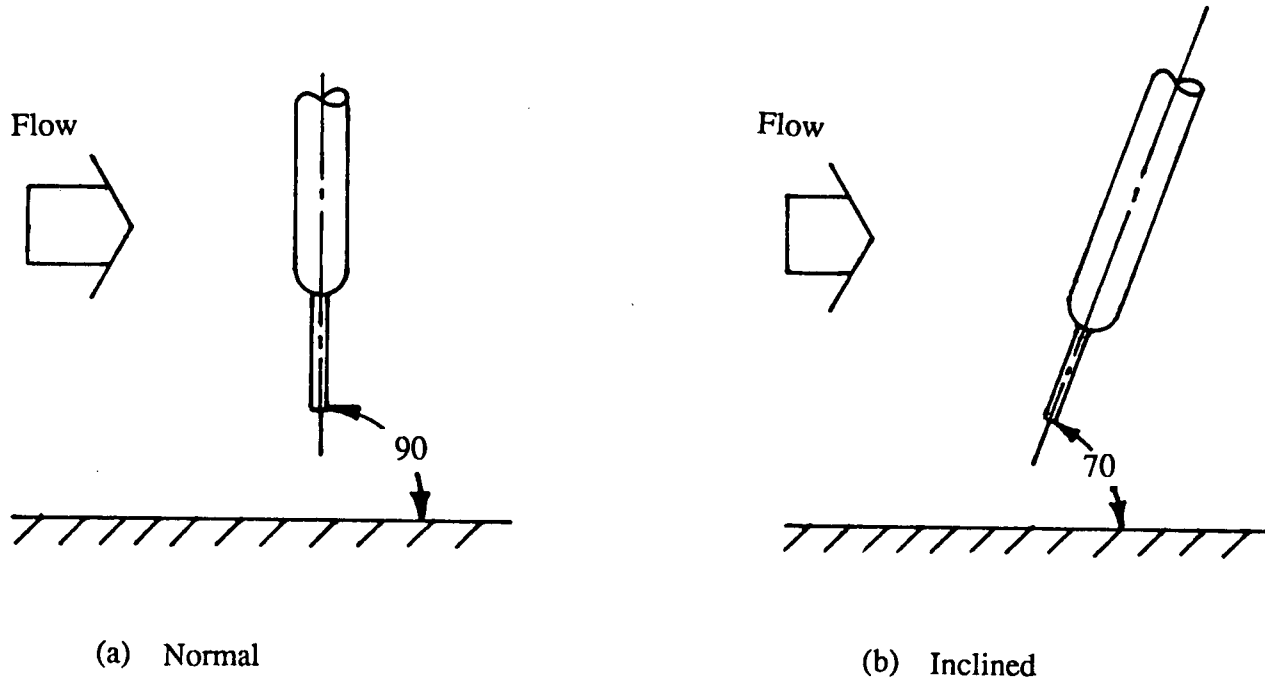


Figure 2.4 Hot wire probe orientations

Table 2.1. Hot Wire Calibration Constants for Two Probe Inclinations

Probe Orientation	Normal	Inclined	Difference
Gain (V ²)	4358740.0	4305950.2	-1.2%
Offset (V ²)	3565350.2	3628715.2	+1.7%
Exponent	0.45	0.45	n/a
Correlation, r ²	0.9962	0.9963	n/a

hot wire anemometer to accurately measure the mean and fluctuating speed at the slot opening without altering the 'normal' calibration constants. Further support for use of the single wire probe in the slot region is given by Bradshaw [36]. He shows that "a cylindrical hot wire is entirely insensitive to changes of flow direction in the plane normal to the axis of the wire". This statement ignores the proximity of the support prongs. If the flow approaches the wire as shown in Figure 2.4b the prongs should not interfere with the flow near the wire. Other situations may, however, suffer from prong or probe-holder interference.

Bradshaw [36] also discusses the effect of air temperature on hot wire calibration. He concludes "in air, 1 C temperature change may produce an error of 2 percent in measured velocity". This difference is due, in part, to the temperature dependence of the fluid properties and the wire Nusselt number. For these reasons, the bulk temperatures of the freestream air and the plenum air are carefully monitored during velocity measurements.

2.1.2.2 Temperature

The freestream and plenum air temperatures are monitored with two Copper-Constantan thermocouples and their digital displays. Each thermocouple is shielded with a tubular polyethylene baffle. The baffle is intended to reduce convective cooling of the thermocouple bead thereby improving the reading reliability.

Each thermocouple and its display unit are calibrated within the temperature range $0\text{ C} \pm 0.2\text{ C}$ to $26\text{ C} \pm 0.2\text{ C}$. This calibration has been measured against an 45.7 cm mercury bulb thermometer. The calibration is checked randomly during velocity measurements. The combined uncertainty of the thermocouple system is $\pm 0.5\text{ C}$ or typically ± 2 percent.

2.1.2.3 Plenum Mass Flowrate

To determine a mean velocity in the slot, and hence to define the mass flow ratio, M , the mass flowrate of air entering the plenum is measured with a type R-11M-25-2 Brooks rotameter.

The rotameter had been calibrated by the manufacturer in the flow range 3 to 30 scfm of air at standard conditions. Flow rates of 25 to 28 scfm are used in these experiments. Within the assumed calibration, the uncertainty of any given flow measurement is ± 0.25 scfm or typically ± 0.9 percent. It should be noted during any given test, the air supply flowrate fluctuates up to ± 0.25 scfm. This fluctuation is caused by pressure fluctuations in the air supply line upstream of the pressure regulators. Work done subsequent to this thesis suggests that the calibration assumed for the rotameter may

have been incorrect by 13 percent. This would mean that the values of M stated in this thesis are 13 percent higher than they should be. Although an error of this sort would not affect the flow measurements it would affect the agreement between the measurements and the numerical predictions. This affect is further discussed in sections 2.3.3 and 4.2.

2.1.2.4 Static Pressure

Static pressure measurements have a dual role in these experiments. Their first role permits the establishment of a zero pressure gradient boundary layer in the wind tunnel. Their second role permits the observation of the static pressure variation on the plate surface upstream and downstream of the slot. Unfortunately, limitations on the number and location of pressure taps prevent high resolution of the pressure variation near the slot. For this reason, static pressure distributions on the plate surface are measured for the 20 degree slot geometry only. The pressure tap locations are further described in section 2.1.3

The static pressures are measured with two systems. The zero pressure gradient condition is established with the use of an inclined differential alcohol manometer. This device is used on its most sensitive setting where it has an uncertainty of ± 0.02 Pa or ± 0.03 percent of full scale.

The surface pressure measurements on the plate are obtained with a type 511-J10 Datametrics Barocel Pressure Sensor and a type 1018B Datametrics electronic manometer. The Barocel pressure transducer is connected to pressure taps in the model via a 49 port switchable Scanivalve, type 48J9. Figure 2.5 shows a schematic diagram of this system.

The Barocel pressure transducer measures differential pressures in the range ± 10 mm Hg. The combined uncertainty of the Barocel and electronic manometer is

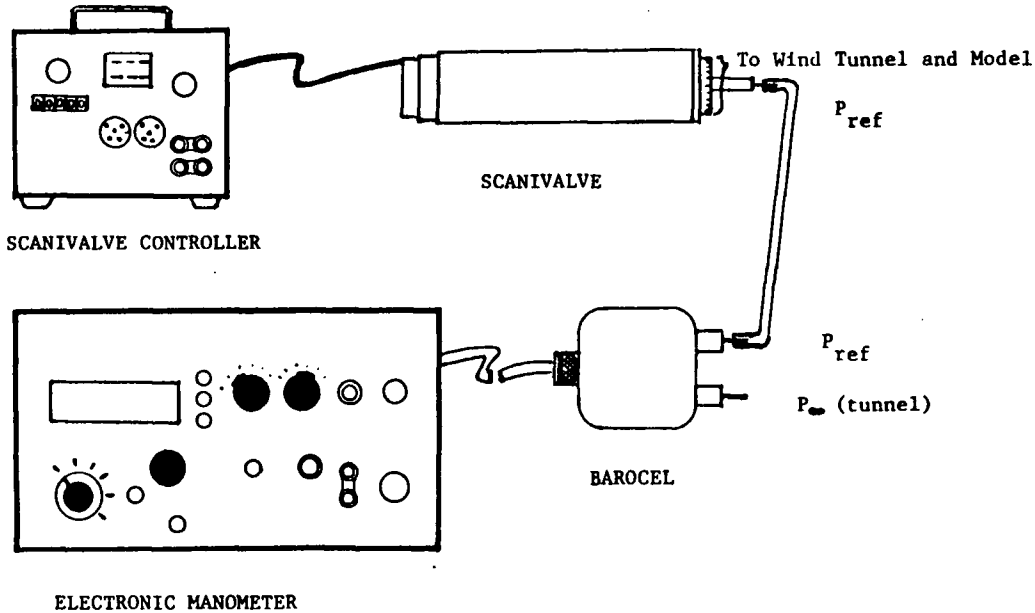


Figure 2.5 Schematic of pressure instrumentation
Reproduced Here with the Permission of A.C. Stewart [36]

± 0.001 mm Hg or ± 0.02 percent of full scale. Cross checks of both measuring systems show good agreement.

2.1.2.5 Hot Wire Probe Position

The hot wire probe is positioned with the aid of Starrett and Mitutoyo dial gauges. These gauges can be seen in Figure 2.3. Both gauges allow accurate position measurement within ± 0.0127 mm. The Starrett gauge is used to measure the position normal to the plate surface. The Mitutoyo gauge is used to measure the position upstream or downstream of the slot leading edge.

2.1.3 Experimental Models

The two models used in these experiments consist of two pairs of smooth, flat, plexiglas plates. Each pair of plates, when installed, rests on a false floor in the plenum module. This configuration allows each test plate to be flush with the test section floor while maximizing the span and adjustability of the slot. These three features help minimize three-dimensional effects.

For the tests at hand, the slot width is set at 6.35 mm ± 0.00254 mm. Choice of this gap is based on a typical length to diameter ratio for film cooling orifices in turbine blades. The ends of each pair of plates are ground to produce angles of 20 and 40 degrees. They are surface ground to minimize the radius of curvature of the slot leading and trailing edges. Figures 2.6 and 2.7 show drawings of each pair of plates. Note the 20 degree pair contains 17 pressure taps while none are in the 40 degree pair. These taps are

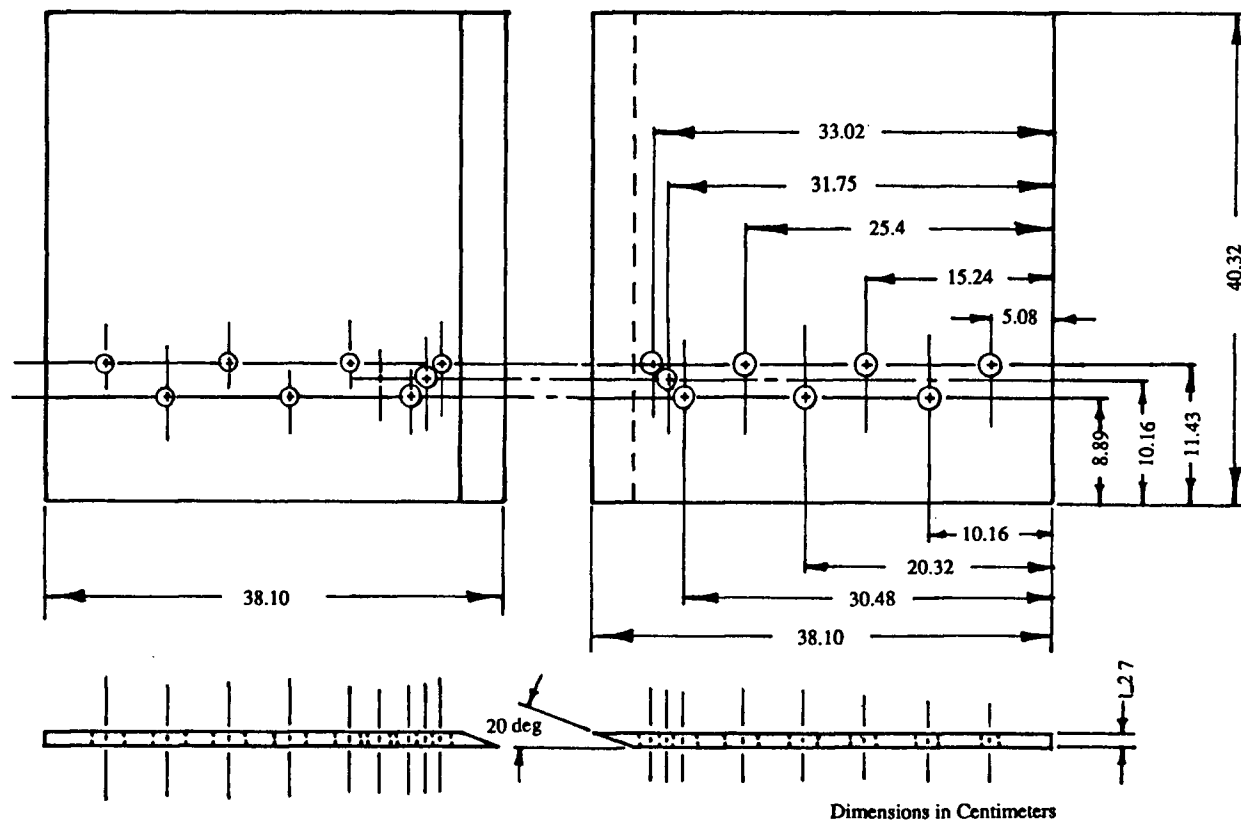


Figure 2.6 Plates for the 20 degree slot experiments

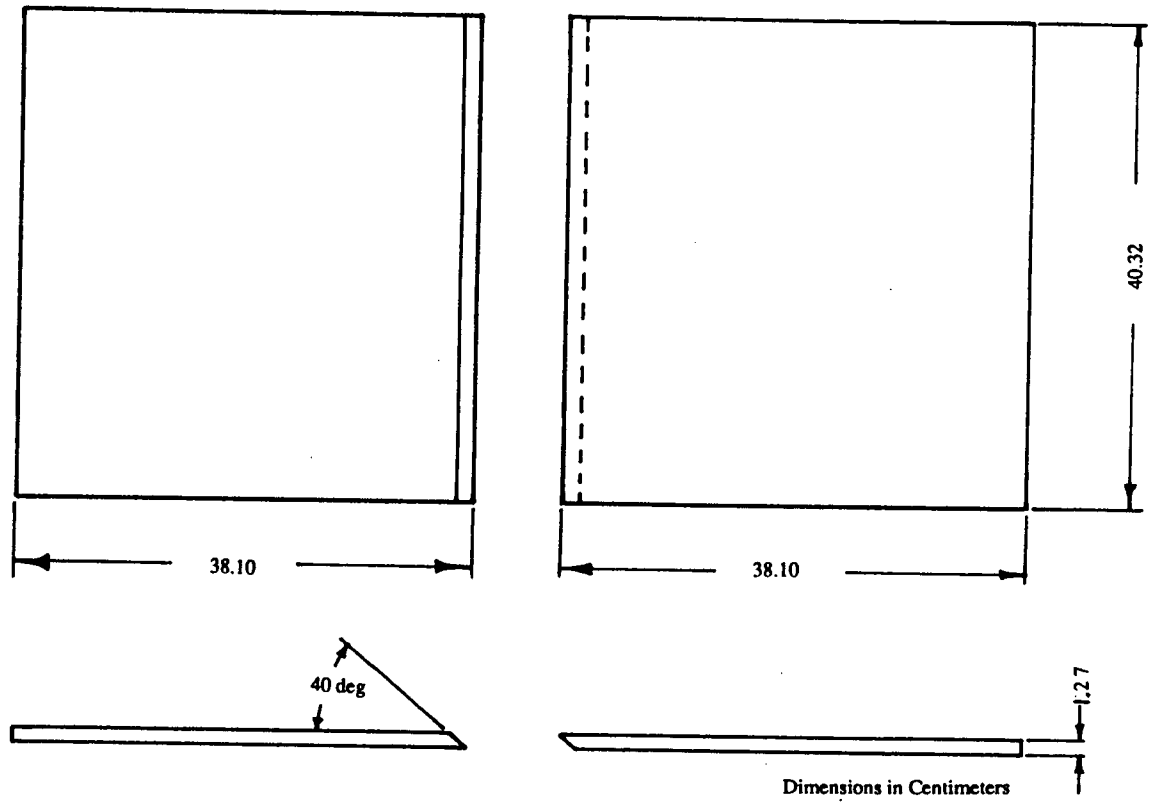


Figure 2.7 Plates for the 40 degree slot experiments

omitted from the 40 degree pair because the desired resolution could not be obtained.

The pressure taps are connected via Intramedics, 2.42mm diameter, tubing which passes along the plenum wall through a flange and eventually to ports on the Scanivalve.

When a pair of plates is installed in the plenum module they are adjusted until the top surface of each is parallel within 0.0254 mm and until the slot face of each is perpendicular to the mainstream flow direction. After adjustment, the plates are sealed and fastened in place with masking tape. A 1.59 mm diameter boundary layer trip wire placed 35.56 cm upstream of the slot is also added to the plates to ensure a fully turbulent upstream boundary layer.

2.2 Experimental Procedures

A wide variety of detailed procedures are employed to collect, verify and cross check good experimental data. The detailed aspects of these procedures are capably dealt with in reference books like those of Bradshaw [37], Pope and Harper [38], and Merzkirch [39]. The following discussions are brief outlines of the procedures used to measure a series of velocity profiles and confirm flow two-dimensionality.

2.2.1 Velocity and Turbulent Intensity Profiles

Figure 2.8 indicates the spanwise and streamwise locations where velocity and turbulent intensity profiles are measured. For a given mass flow ratio and slot angle, profiles are obtained at each of the centreline locations noted in Figure 2.8. A typical series of profile measurements entails the following steps:

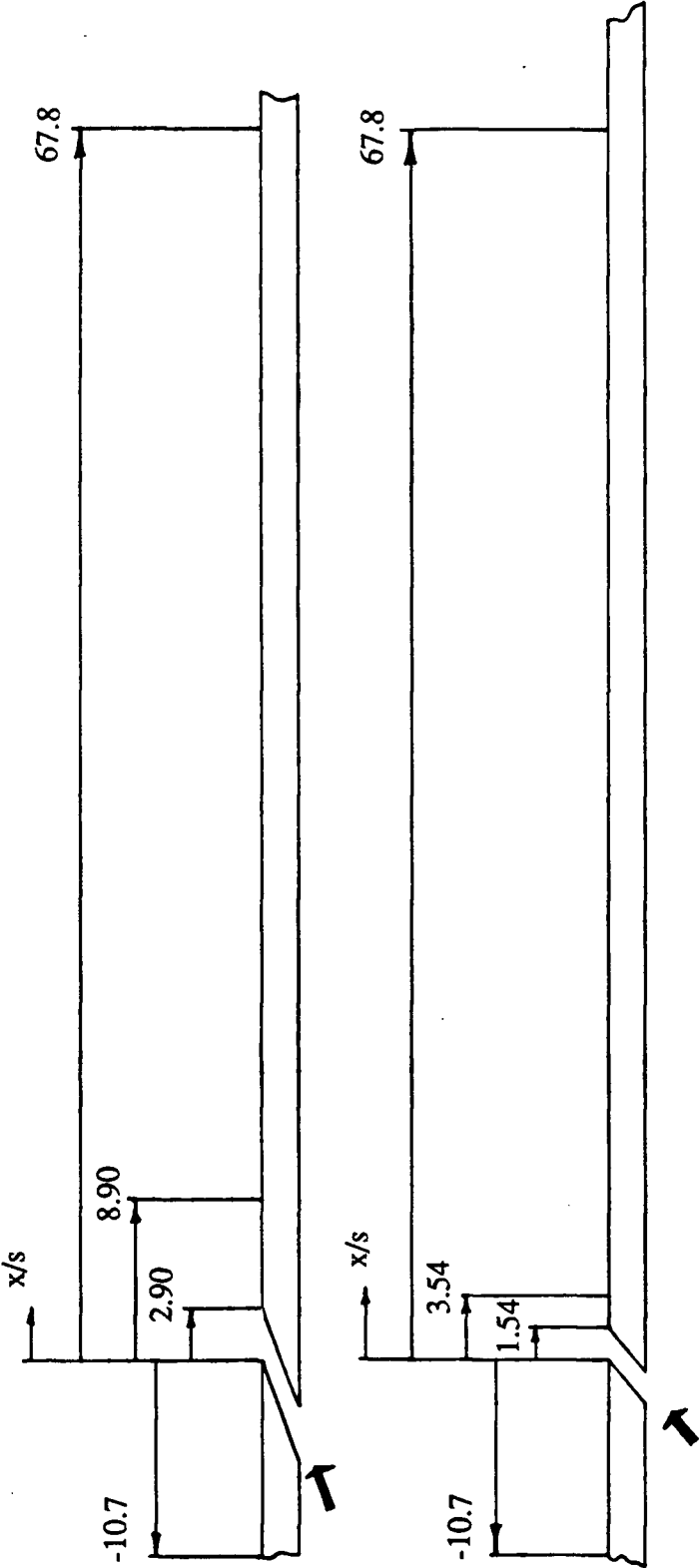


Figure 2.8 Streamwise locations of velocity profiles

- 1) Set the flowrates to the desired levels. Allow them to stabilize for 45 minutes.
- 2) Check that the overall pressure gradient in the wind tunnel is zero.
- 3) Check the calibration of the hot wire system against a standard pitot-static tube.
If the difference between measured freestream velocities is greater than 2 percent, recalibrate the system.
- 4) Position the hot wire probe at the first profile location, i.e. position 1 in Figure 2.8.
- 5) Measure the freestream velocity.
- 6) Note the plenum and freestream temperatures. If the difference is larger than 1 C, abort the measurement.
- 7) Measure the mean and fluctuating velocity across the flow with maximum spatial resolution in regions of nonzero mean velocity gradient.
- 8) Reposition the probe at the freestream location. Remeasure the freestream velocity. If the freestream velocity has changed more than 5 percent, repeat the profile measurement.
- 9) Position the probe at the next profile location.
- 10) Repeat steps 5 to 9 until all of the profiles have been measured.

2.2.2 Two-Dimensionality of the Flow

Two-dimensionality of the experimental flow is important because the experimental results are compared with two-dimensional flow computations. Figure 2.9 indicates the streamwise and spanwise locations where velocity profiles are measured for this purpose. The measurements are made for the midrange case of the 20 degree slot with a mass flow ratio of 0.90. The steps involved are:

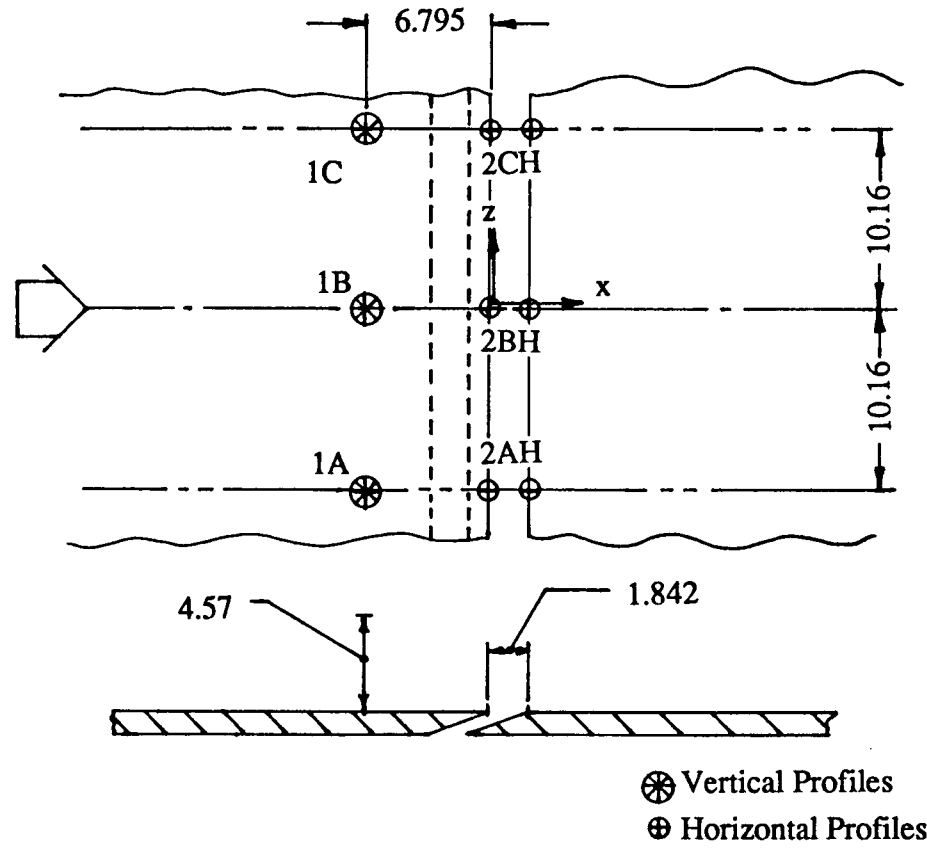


Figure 2.9 Locations of the two dimensionality measurements

- 1) Set the mainstream and plenum flowrates to the desired levels. Allow the flow to stabilize for 45 minutes.
- 2) Use the profile measurement method outlined in section 2.2.1 to measure the profiles at positions 1B and 2BH, (as indicated in Figure 2.9). At position 2BH, the probe is positioned 0.127mm above the plate surface.
- 3) Repeat step 2 for positions 1C and 2CH, (as indicated in Figure 2.9).
- 4) Repeat step 2 for positions 1A and 2AH, (as indicated in Figure 2.9).

2.3 Typical Experimental Results

The following discussion presents the flow field measurements in an effort to understand the nature of this complex flow.

2.3.1 Two-Dimensionality Tests

Tests to determine the two-dimensionality of the wind tunnel flow are done for the case $\alpha = 20$ degrees and $M=0.90$. Mean and fluctuating velocity profiles are obtained in two streamwise locations and three spanwise locations. The mean velocity profiles are presented in Figure 2.10. Figure 2.10a indicates the mean flow upstream of the slot is remarkably two-dimensional since there appears to be little spanwise variation of the mean velocities. Figure 2.10b indicates, on average, the mean velocities in the slot region and on either side of the plate centreline are 5 percent lower than the mean velocity at the plate centreline. This difference indicates a small degree of flow three-dimensionality. Since the slot velocity differences are small in the spanwise direction, we can say the flow exiting the slot is essentially two-dimensional within the range of the spanwise measurements, i.e. 10.16 cm on either side of the plate centreline. It is

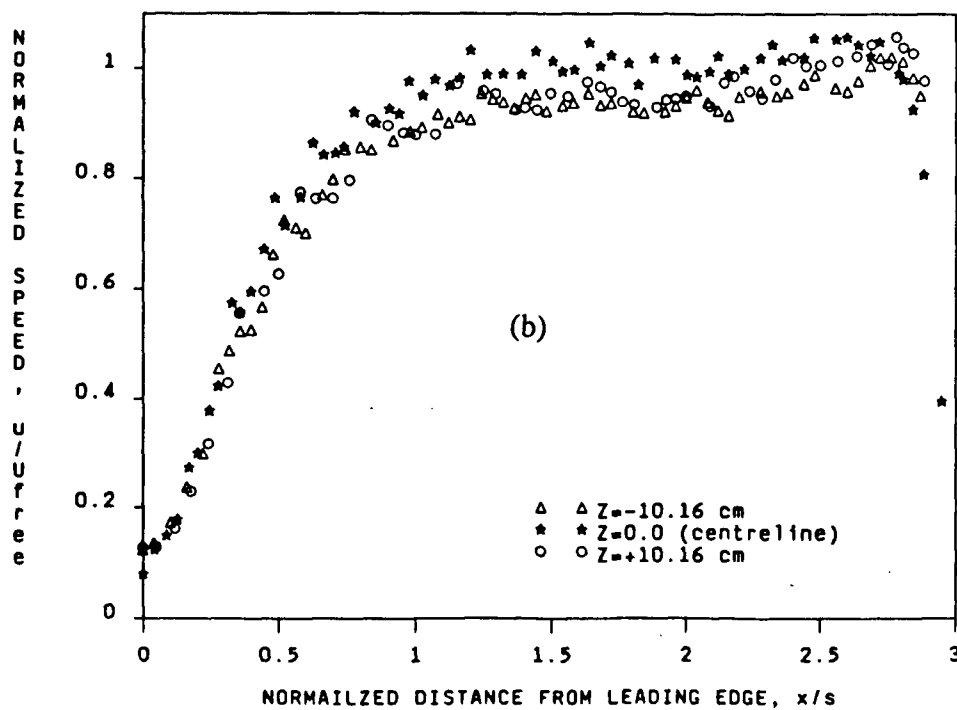
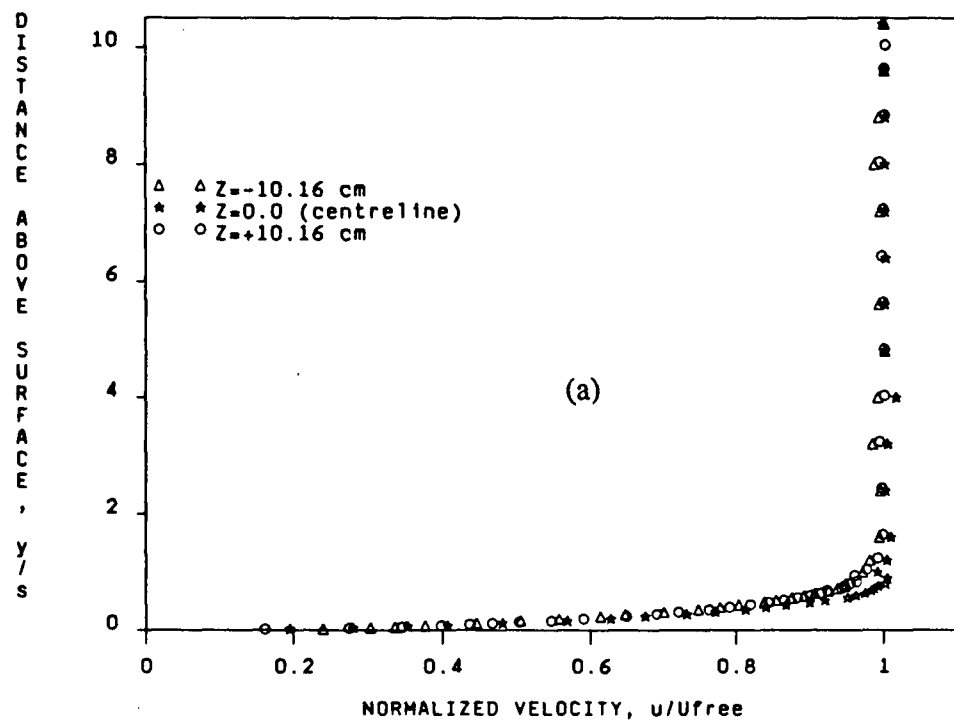


Figure 2.10 Mean velocity and speed profiles for $\alpha = 20$ degrees and $M = 0.8955$ a) upstream and b) across the slot

expected, however, that this flow is not accurately two-dimensional outside this region.

The latter expectation is due to the wall boundary layer interacting with the inclined jet to form an unstable shear layer along the wind tunnel wall.

2.3.2 Mean Velocity Profiles

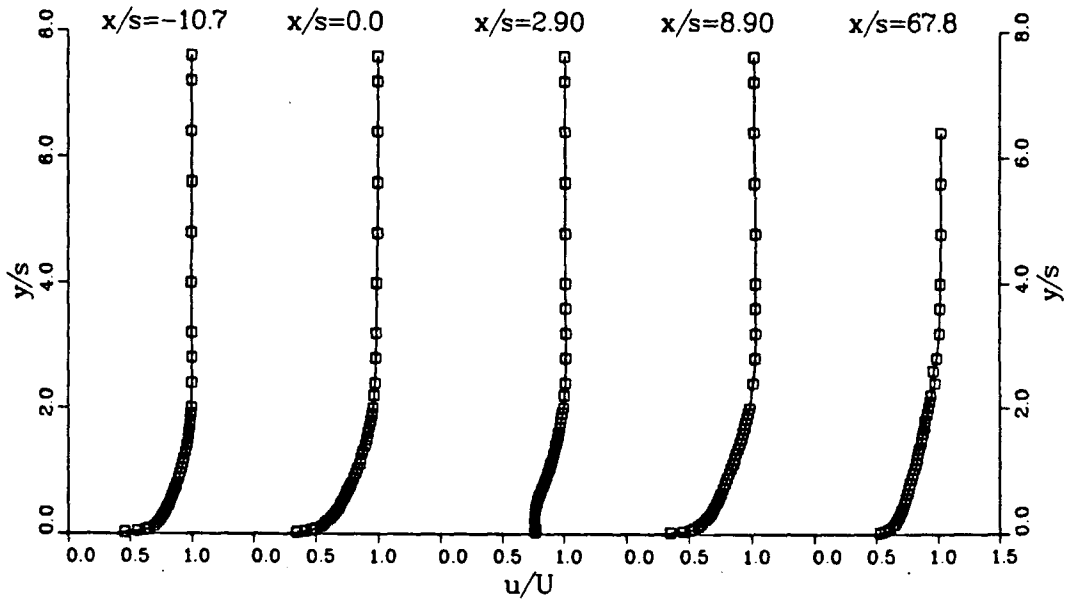
Mean velocity profiles have been obtained at each of the locations noted in Figure 2.8. Table 2.2 indicates the conditions under which these measurements have been made.

Slot Angle (degrees)	Experimental Conditions			Temperature (degrees Celcius)
	Mass Flow Ratio*			
20	0.46	0.90	1.4	25
40	0.46	0.91	1.2	25

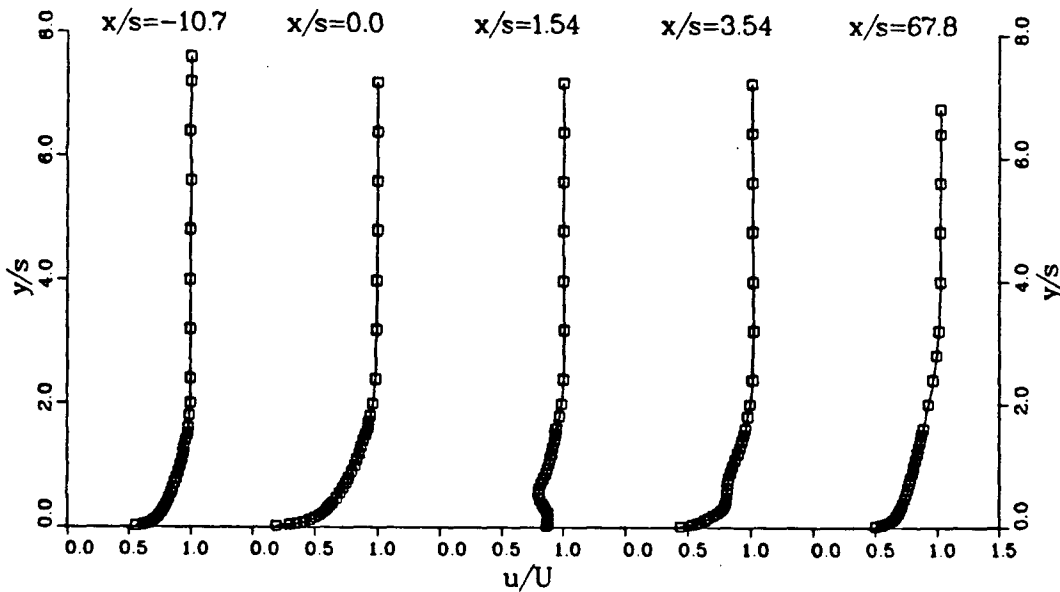
The various mass flow ratios are obtained by adjusting the freestream velocity. The data collected for mass flow ratios greater than 1.4 are limited to speed profiles across the slot.

The experimental mean, streamwise velocity profiles, for the conditions noted in Table 2.2, are presented in Figures 2.11, 2.12 and 2.13. The upstream boundary layer is tripped, for all cases, with a 1.59 mm diameter wire located 56 slot diameters upstream of the slot leading edge. Log-log plots of the velocity profiles at $x/s = -10.7$ have slopes

*See the discussion regarding mass flow ratio in section 2.1.2.3

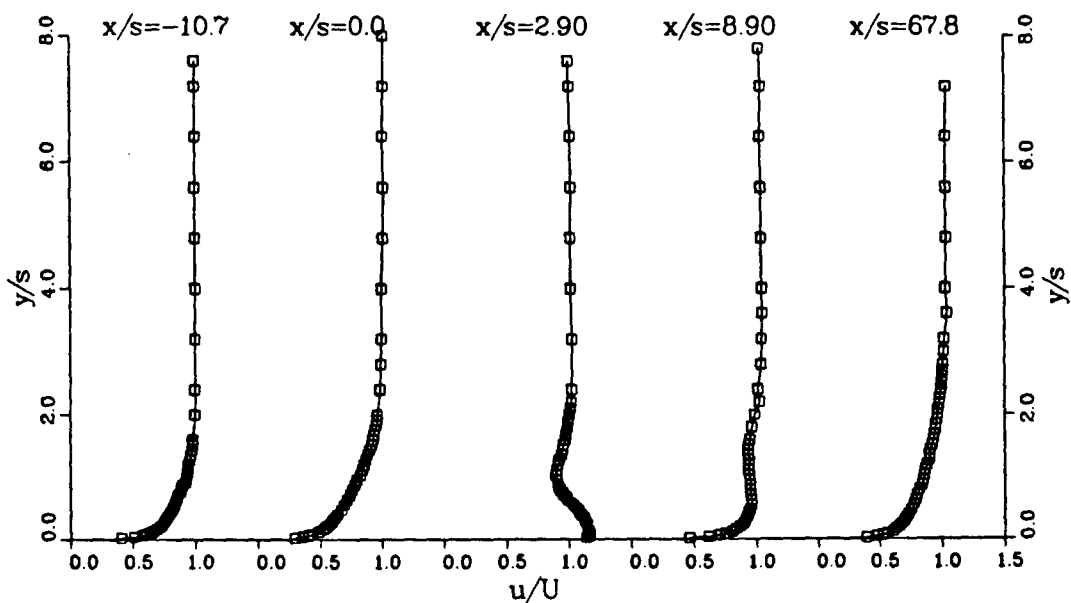


(a)

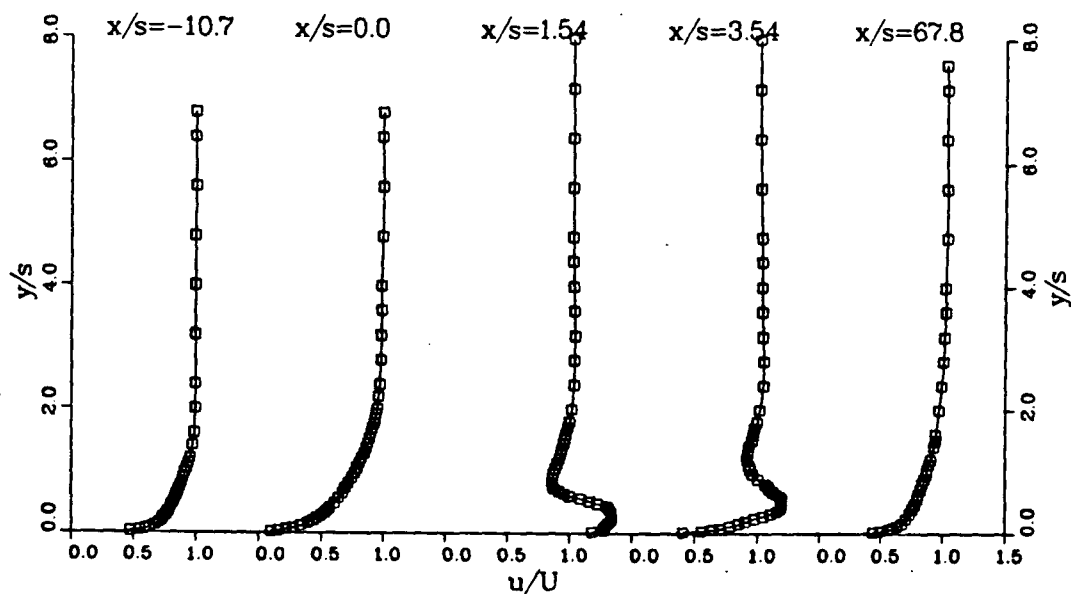


(b)

Figure 2.11 Mean Speed Profiles For 5 Streamwise Locations and $M = 0.46$ and x/s Measured from the Slot Leading Edge
 a) $\alpha = 20$ degrees and b) $\alpha = 40$ degrees

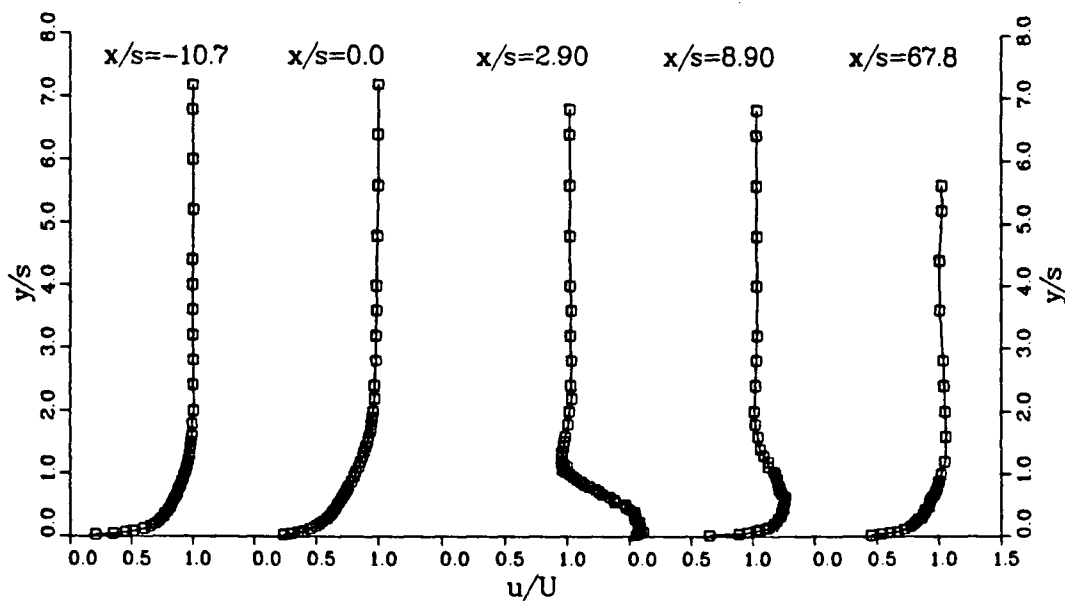


(a)

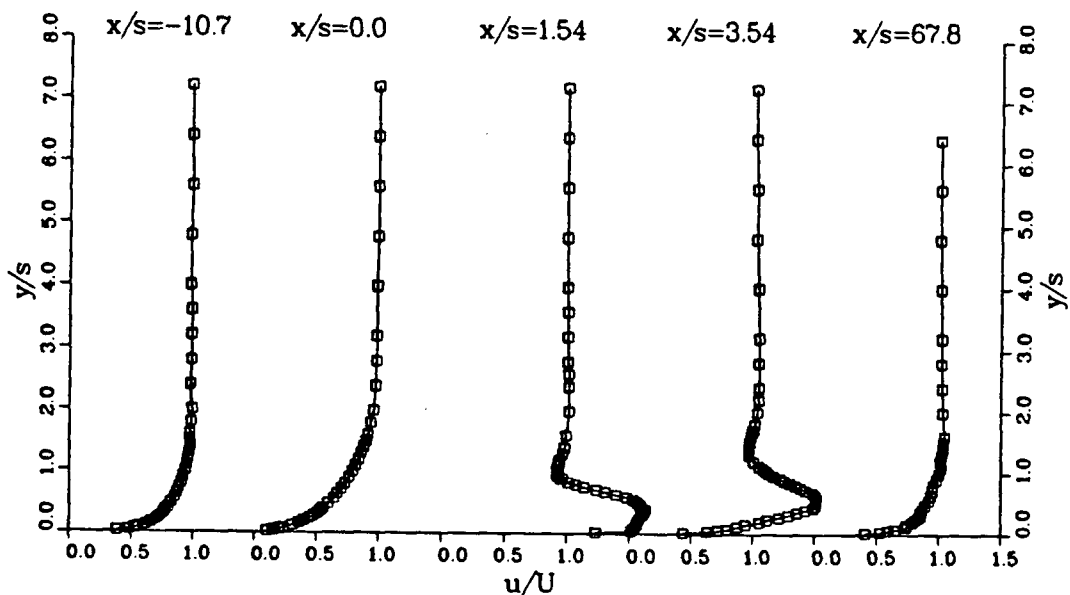


(b)

Figure 2.12 Mean Speed Profiles For 5 Streamwise Locations and $M = 0.9$ and x/s Measured from the Slot Leading Edge
 a) $\alpha = 20$ degrees and b) $\alpha = 40$ degrees



(a)



(b)

Figure 2.13 Mean Speed Profiles For 5 Streamwise Locations and $M \cong 1.3$ and x/s Measured from the Slot Leading Edge
 a) $\alpha = 20$ degrees and b) $\alpha = 40$ degrees

ranging from 5.41 to 7.41. These slopes indicate that the upstream boundary layers are acceptable as turbulent approach boundary layers.

Figures 2.11 to 2.13 clearly indicate the effects of slot angle and mass flow ratio on the flow development. In these figures, x/s is measured from the slot leading edge. The positions $x/s = 1.54$ and $x/s = 2.90$ correspond, respectively, to the slot trailing edge for the 40 degree and 20 degree geometries. Increasing the mass flow ratio results in larger and larger increases in the velocity near the wall, downstream of the slot. This behavior makes sense because increasing the mass flow ratio, by definition, increases the momentum addition from the slot. The slow moving fluid near the wall upstream of the slot mixes with the higher momentum slot flow and is accelerated. When the flow exits the slot at a steep angle, Figures 2.11 to 2.13 indicate that the point of maximum velocity moves farther away from the surface of the plate. Again, this behavior seems plausible because of the larger addition of cross-stream momentum from the slot.

It is interesting and somewhat surprising to note that separation is not detected at the slot trailing edge. Separation is expected in these experiments because of the sharp trailing edges. The 40 degree flows for $M = 0.91$ and $M = 1.2$ have a sharp, well defined peak in their velocity profiles at $x/s = 3.54$. This peak suggests that most of the flow from the slot has penetrated into the freestream in a fairly distinct jet. However, since separation is not observed for these flows, a certain amount of slot flow must be turned through a relatively large angle at the trailing edge to avoid separation. This behavior would be characterized by strong acceleration and curvature of the flow near the trailing edge. Such behavior would be accompanied by steep pressure gradients at the trailing edge. Attempts to detect separation with flow visualization are described in section 2.3.6

Flow development far downstream of the slot seems to be, roughly, analogous to that of a classical wall jet. The tangential wall jet is described and analysed by

Schlichting [40] and Glauert [41] respectively. However, quantitative comparisons with this flow are not made here.

Figure 2.14 illustrates surface pressure coefficients obtained for the 20 degree slot. The rise in pressure upstream of the slot indicates that a small adverse pressure gradient is present near the slot. As a result, the flow near the wall slows down as it approaches the slot leading edge. Within the slot region, however, the pressure gradient at the wall becomes very favourable due to the addition of momentum from the secondary flow. This favourable pressure gradient reflects a strong acceleration of the near wall flow. Figure 2.14 also indicates that the strength of this acceleration decreases with decreasing mass flow ratio.

Immediately downstream of the slot, the pressure coefficient exhibits a sharp adverse pressure gradient. This pressure gradient decreases to almost zero within 20 slot widths of the slot. The presence of a strong adverse pressure gradient reflects the recovery of the flow from its highly curved path, at the slot trailing edge, and the development of a wall flow.

These observations of pressure gradient variation provide insight to the behavior of the flow in the near wall region. The interpretation of this data is in qualitative agreement with the interpretation of the mean velocity data. Both types of data indicate the flow is decelerated near the slot leading edge and accelerated near the slot trailing edge. Furthermore, both sets of data indicate that the flow develops as a wall flow far downstream of the slot.

Another interesting feature of the velocity data is the variation of the flow speed at the slot exit. This feature is illustrated in Figures 2.15 and 2.16 for the 20 and 40 degree slots respectively. These figures indicate that a large proportion of the mass leaving the slot does so from the downstream portion of the slot. Furthermore, the degree

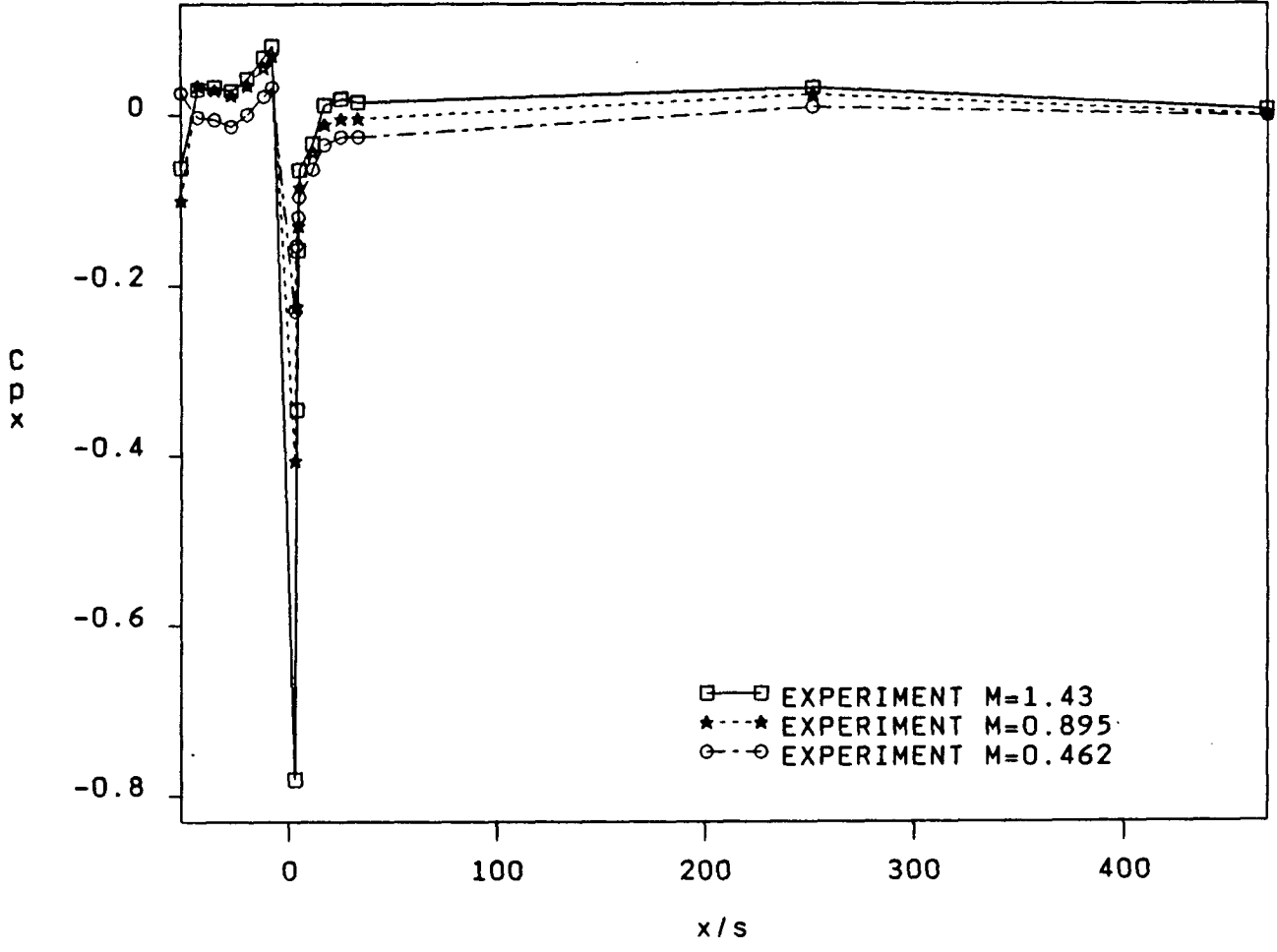


Figure 2.14 Surface Pressure Coefficients for $\alpha = 20$ degrees

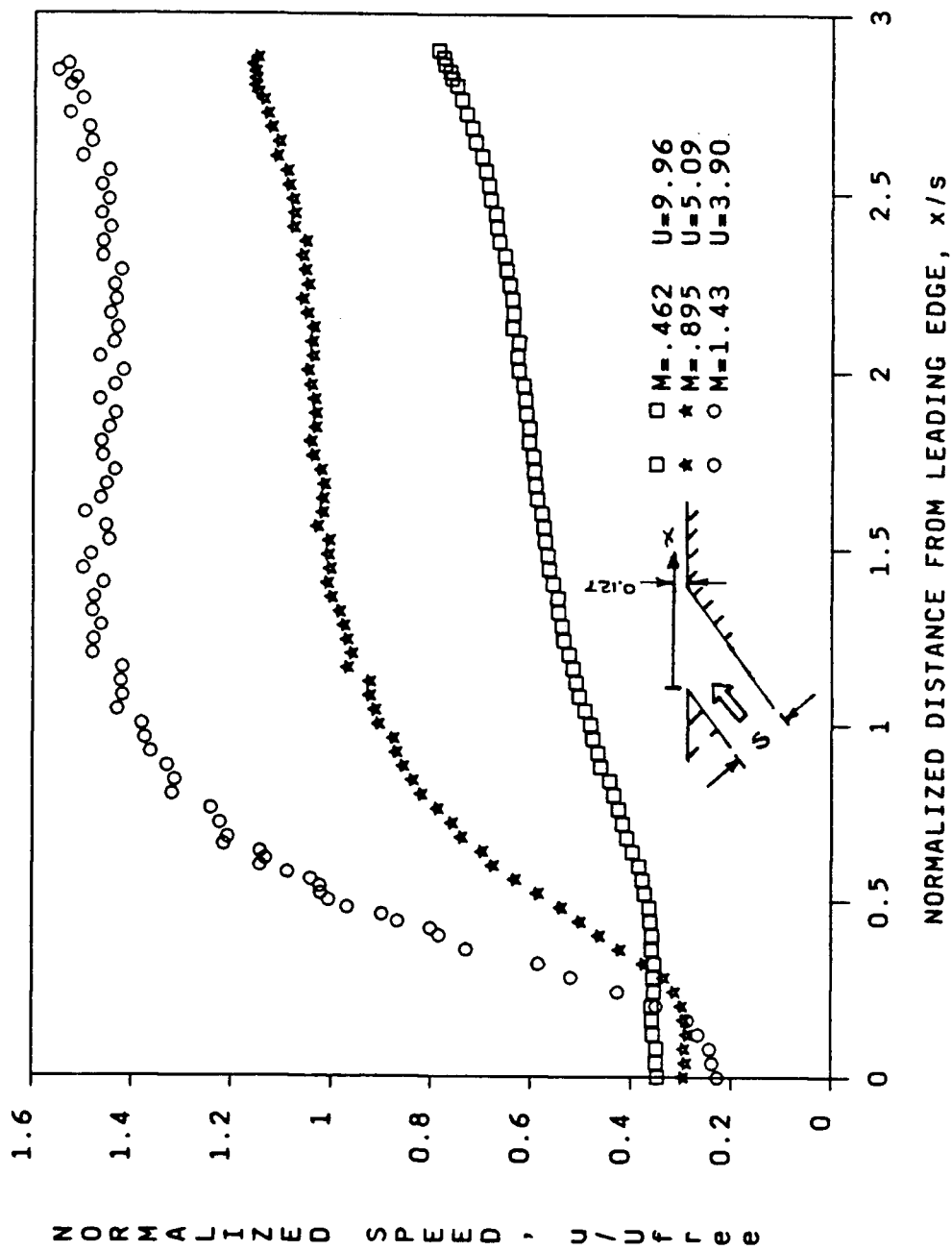


Figure 2.15 Slot Mean Speed Profiles for $\alpha = 20$ degrees

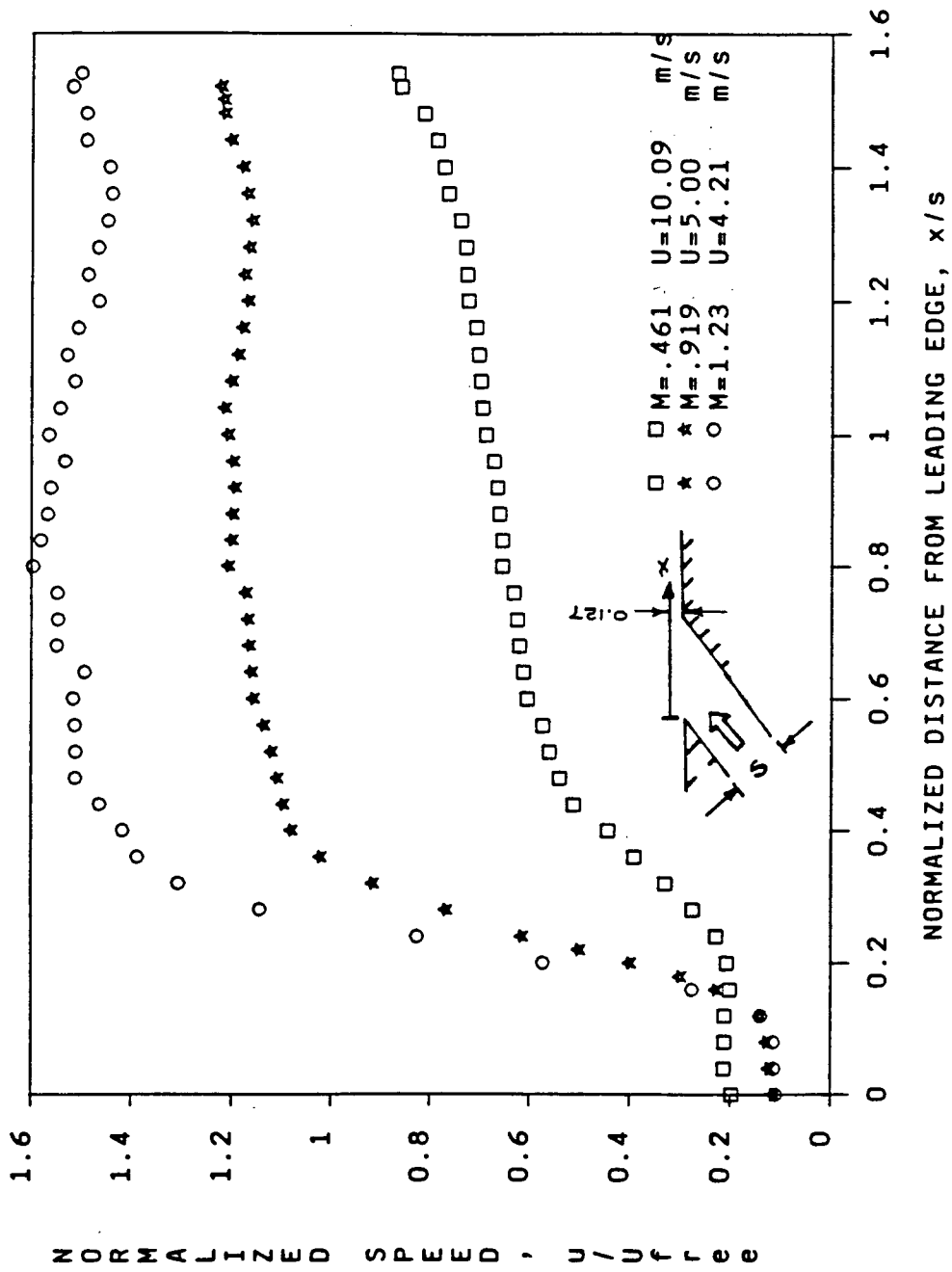


Figure 2.16 Slot Mean Speed Profiles for $\alpha = 40$ degrees

of non-uniformity in the speed profile depends on the relative strength of the main and secondary streams.

The velocity exiting the slot might be expected to have uniform magnitude and uniform direction parallel to the slot. Since the maximum measured speed, in each case, is not much larger than the value given by the mass flow ratio, the flow direction in the slot must be significantly different from the slot angle. Unfortunately, the flow angles in the slot were not measured here. The flow angle in the slot is further considered in the following section.

2.3.3 Mass Flow Verification

The mass flow rate of air entering the plenum provides an integral condition for the flow leaving the slot. Integration of each slot velocity profile should reproduce the corresponding measured mass flow rate. In this connection, reference should also be made to a calibration uncertainty described in section 2.1.2.3 of this thesis.

Velocity profile integration requires two assumptions. Firstly, the flow is assumed to be perfectly two-dimensional. Three-dimensional effects, observed in section 2.3.1, indicate this assumption is not strictly correct. However, the error introduced by a two-dimensional assumption should be small since the three-dimensional effects are small. Secondly, an assumption is required for the flow angles at the slot exit. For example, one could assume the flow leaves the slot at the slot angle. Observations in section 2.3.2 suggest this is probably not the case. The second assumption must, therefore, be made so the mass flow rate measured by the rotameter is recovered by integration of the velocity profile across the slot.

Figure 2.17 presents the results of the slot velocity profile integrations. These

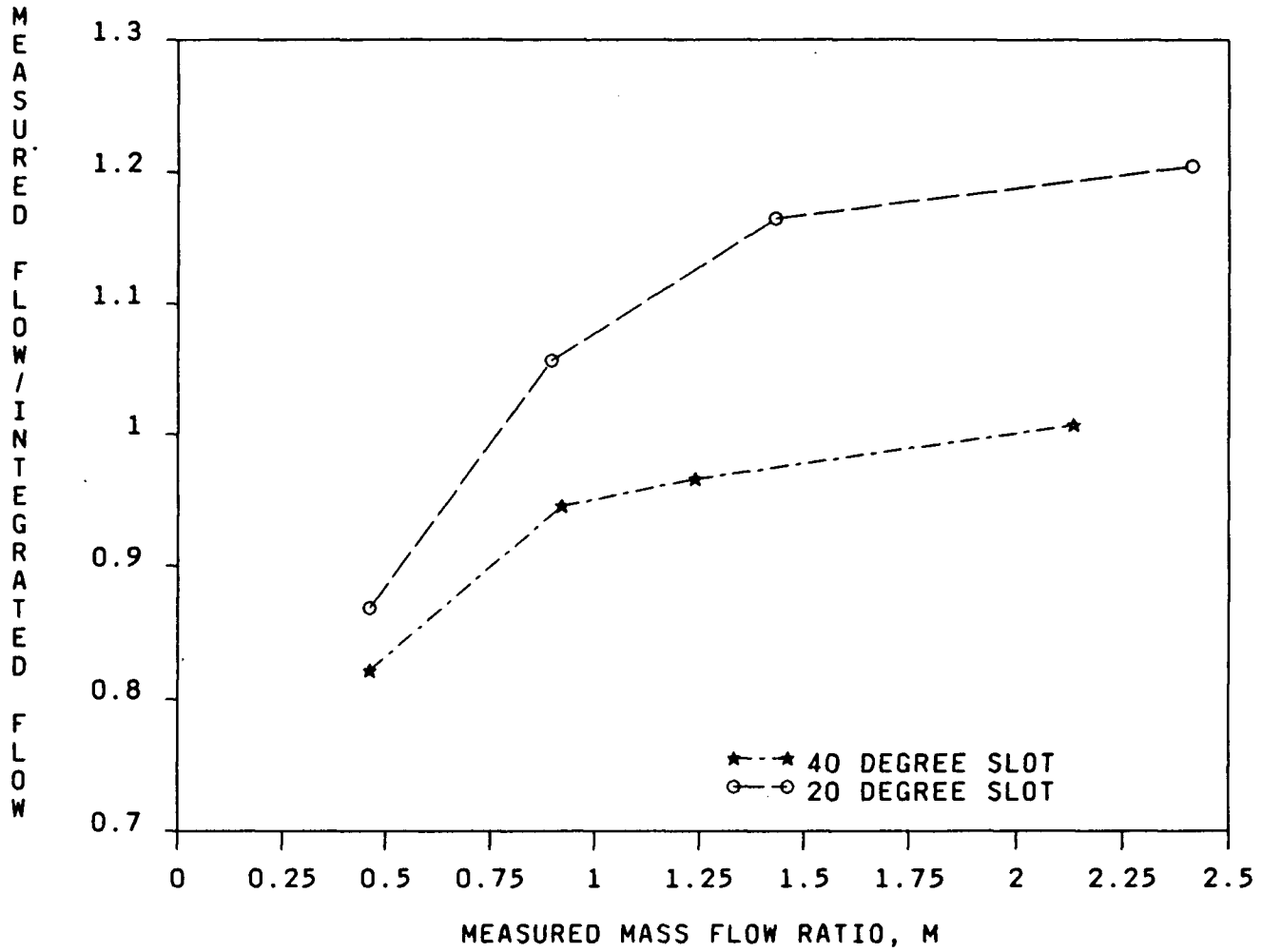


Figure 2.17 Slot velocity profile integrations for $\alpha = 20$ and 40 degrees

integration results are obtained by arbitrarily assuming the flow leaves the slot at the slot angle. It is interesting to note that both curves follow the same trend. Regarding the 40 degree slot results, the integrated value approaches the measured value as the mass flow ratio increases. This indicates that the bulk of the secondary stream is turned less and less, at the slot, as the relative strength of this stream is increased. In other words, the assumption of a uniform flow angle equal to the slot angle is more valid as the mass flow ratio increases. For very high mass flow ratios, however, the measured flow may exceed the assumed flow as discussed in the next paragraph.

Interpretation of the 20 degree slot results is not as clear. Large differences between measured and integrated mass flow rates are evident for mass flow ratios less than and greater than one. These differences are probably not all due to the slot flow being turned downstream by the external flow. Since the integrated mass flow rate is less than the measured value, for high mass flow ratios, the flow appears to leave the slot at an angle greater than the slot angle in these cases. This behavior is presumably due to a slot that is too short to direct the flow. Thus, in some cases, the slot may act more like an orifice than a slot. This flow behavior is considered in the following flow visualization section and again in chapter 4 in connection with the numerical results.

As already noted in section 2.1.2.3, there is some uncertainty about the calibration of the rotameter used in these experiments. If, as subsequent work suggests, the calibration was in error by 13 percent, the graphs shown in Figure 2.17 would be shifted down by the same 13 percent. The effect of such a shift would not alter the flow description presented above.

2.3.4 Flow Visualization

Two methods of visualization are used to study the flow exiting the slots. Smoke is used to follow the flow of fluid ejected through the 20 degree slot. The "oil of wintergreen" method is used to look for separation downstream of the 40 degree slot.

The results of the smoke visualization indicate a dramatic and surprising variation in the flow behavior near the slot. Smoke is ejected from the slot as indicated in Figure 2.18. By varying the mass flow ratio, the average angle β_{ave} , made between the smoke and the horizontal, is observed to vary noticeably. For low mass flow rates, i.e. weak secondary streams, the smoke is blown sharply downstream and β_{ave} appears much smaller than the slot angle. For the higher mass flow ratios, β_{ave} appears to be slightly larger than the slot angle. This latter observation reflects flow behavior akin to flow through an orifice as noted in section 2.3.3. This behavior is likely to be a consequence of the slot length to width ratio. The length to width ratio for the 20 degree slot is 3.10 and that for the 40 degree slot is 1.92. Future work on flow from slots or orifices should consider an in depth examination of the combined effects of length to width ratio and mass flow ratio on film cooling flows.

The absence of flow separation evidence from the 40 degree slot measurements is somewhat surprising. The hot wire measurements of Figure 2.12 do not indicate separation although the momentum from the slot seems to penetrate significantly into the freestream. The "Oil of Wintergreen" technique is applied for the case of $M = 0.91$.

A copy of the ink smear pattern obtained at the plate centreline is presented in Figure 2.19. The ink smears of this test appear to be in the downstream direction near the slot. This indicates that separation is not present for this case. In fact, separation was not observed for any of the flow cases considered in this study.

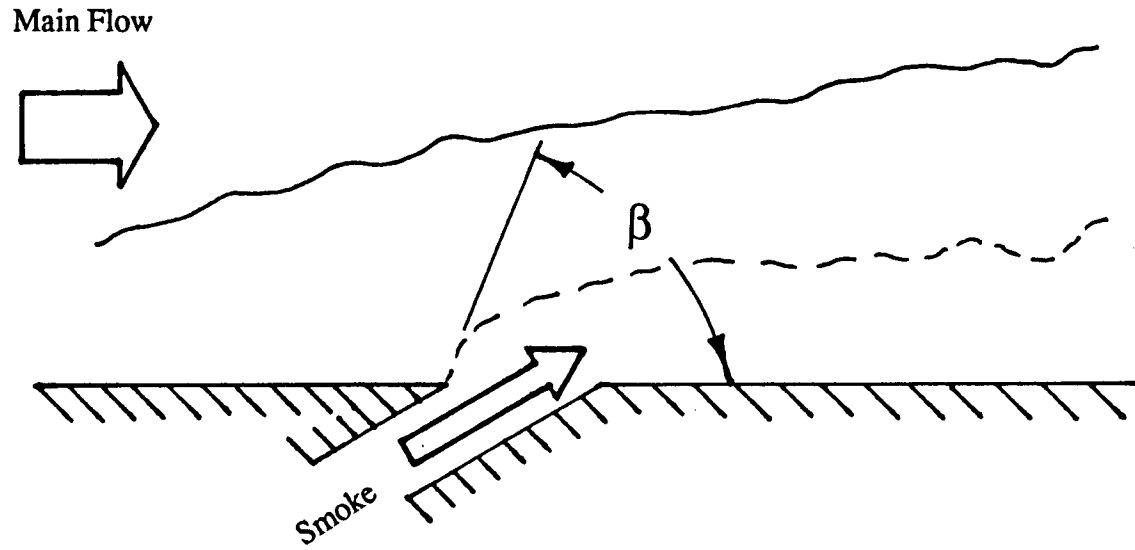


Figure 2.18 Illustration of Flow Visualization with Smoke

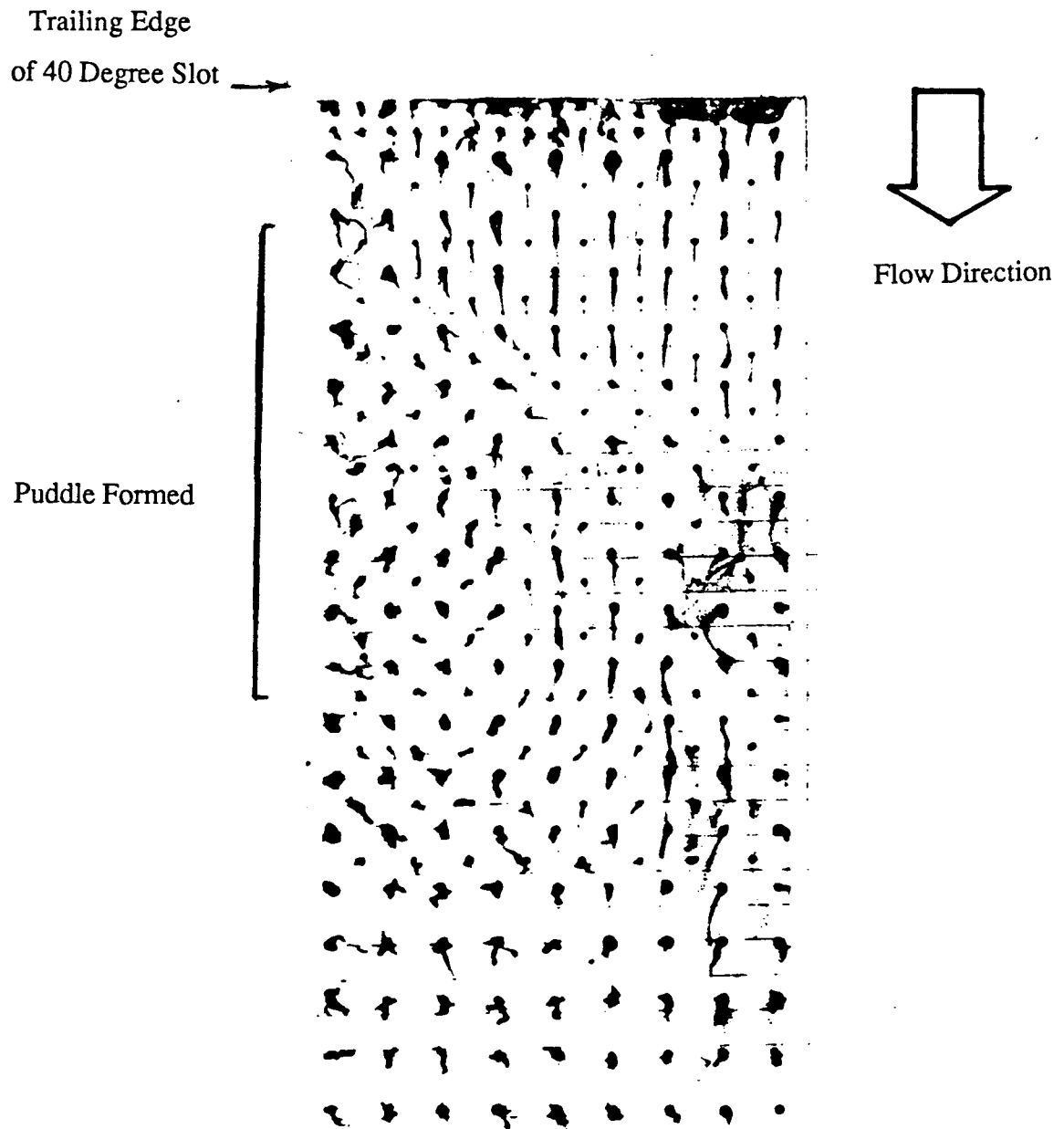


Figure 2.19 Ink Smear Pattern From the Oil of Wintergreen Visualization

3. NUMERICAL INVESTIGATION

*"... I have promises to keep
and miles to go before I sleep,
and miles to go before I sleep"*

Robert Frost

3.1 Background

The fundamental equations of fluid dynamics represent the laws of conservation of mass, momentum and energy. The derivations and limitations of these equations are discussed in detail by Schlichting [40] and Bird, Stewart and Lightfoot [42]. The variables encountered in the following equations are defined in the nomenclature.

When combined with an equation of state and assumptions for the fluid stress tensor the conservation equations form a closed set which can, ideally, be solved for any given conditions. Many factors contrive to make the conservation equations difficult and, most often, impossible to solve in closed form. Solutions are easier to obtain when simplifying assumptions are made. For an incompressible, isothermal Newtonian fluid, such as gas at speeds less than Mach 0.3, the conservation equations (in tensorial form) are:

$$\text{mass} \quad \frac{\partial u_i}{\partial x_j} = 0 \quad (3.1)$$

$$\text{momentum} \quad \rho U_j \frac{\partial U_i}{\partial x_j} = -\frac{\partial p}{\partial x_i} + \mu \frac{\partial^2 U_i}{\partial x_j^2} + \rho f_{b_i} \quad (3.2)$$

$$\text{energy} \quad \frac{\partial}{\partial x_j} (\rho c_p u_j T) = u_j \frac{\partial p}{\partial x_j} + \frac{\partial}{\partial x_j} \left(k \frac{\partial T}{\partial x_j} \right) \quad (3.3)$$

Equation 3.2 forms three scalar equations which are collectively known as the Navier-Stokes equations. To date, only a few closed form solutions exist for the Navier-Stokes equations; several of these are described by Schlichting [40].

A wide spectrum of numerical and analytical techniques are available for solution of the Navier-Stokes equations. Analytical techniques usually make simplifying assumptions in an effort to get a closed form solution. Analytical solutions are usually restricted to simple geometries. In principle, numerical techniques can deal with complicated geometries and physics such as transient, swirling, chemically reacting, turbulent flow. Unfortunately, numerical methods are subject to numerical instability, truncation errors, and high cost. Anderson, Tannehill and Pletcher [43] describe the development and application of many numerical methods. Schlichting [40] and Bird, Stewart and Lightfoot [42] outline the development and application of approximate analytical methods.

Although the exact computation of turbulent flow via Equations 3.1 to 3.3 is possible through direct numerical simulation, it is not practical for many flows of practical interest. Examples of such calculations for low Reynolds number, turbulent channel flows are given by Kim, Moin and Moser [44] and Moin and Kim [45]. The calculations of reference 44 required 250 CPU hours on a CRAY-XMP computer which was fitted with extra memory specifically for this calculation. The grid for this

calculation contained four million grid points.

The problem with turbulent flow computation lies within the complex nature of the flow itself. The numerical grid for such a calculation must have resolution fine enough to distinguish motion in the smallest length and time scales of turbulence. Rodi [46] and Anderson, Tannehill and Pletcher [43] suggest such a calculation may require 10^5 to 10^9 grid points per cubic centimeter of fluid. Modern computers do not have the memory or speed required to deal with the large number of calculations generated by such a grid. For these reasons, the statistically regular nature of turbulent flow is used to study the time averaged effects of turbulence.

The time averaged effects are studied through time averaged Navier-Stokes equations commonly known as the Reynolds equations. Schlichting [40], Reynolds [47] and Anderson, Tannehill and Pletcher [43] provide detailed discussions of the time averaging process.

Hinze [48] conveniently defines turbulent fluid motion as an "irregular condition of flow in which the various quantities show a random variation with time and space coordinates so that statistically distinct average values can be discerned."

In the time averaging process, the instantaneous value of a given variable is replaced by a mean value plus an instantaneous fluctuation about the mean, as in Equations 3.4.

$$\begin{array}{ll}
 \mathbf{U} = \bar{\mathbf{U}} + \mathbf{u} & H = \bar{H} + h' \\
 \mathbf{V} = \bar{\mathbf{V}} + \mathbf{v} & T = \bar{T} + T' \\
 P = \bar{P} + p & \rho = \bar{\rho} + \rho'
 \end{array} \tag{3.4}$$

The mean values are defined by time averages of the instantaneous variables as in Equation 3.5.

$$\bar{U} = \frac{1}{\Delta T} \int_{t_1}^{t_1 + \Delta T} U dt \quad (3.5)$$

Here, ΔT must be much larger than the period of the turbulent fluctuations. Note that ΔT must also be much smaller than the period of the mean flow found in unsteady flow.

After replacing the instantaneous variables with Equation 3.4 in Equations 3.1 to 3.3, the Reynolds equations are derived by time averaging each of Equations 3.1, 3.2 and 3.3. The Reynolds equations, as used in this study, are:

$$\text{mass} \quad \frac{\partial \bar{U}_i}{\partial x_j} = 0 \quad (3.6)$$

$$\text{momentum} \quad \frac{\partial}{\partial x_j} (\rho \bar{U}_i \bar{U}_j) = -\frac{\partial \bar{P}}{\partial x_i} + \frac{\partial}{\partial x_j} \left(\frac{\partial \bar{U}_i}{\partial x_j} + \frac{\partial \bar{U}_j}{\partial x_i} \right) - \frac{\partial}{\partial x_j} (\rho \overline{u_i u_j}) \quad (3.7)$$

$$\text{energy} \quad \frac{\partial}{\partial x_j} (\rho c_p \bar{U}_j \bar{T}) = \bar{U}_j \frac{\partial \bar{P}}{\partial x_j} + \frac{\partial}{\partial x_j} \left(k \frac{\partial \bar{T}}{\partial x_j} \right) - \frac{\partial}{\partial x_j} (\rho c_p \overline{u_j T'}) \quad (3.8)$$

Equations 3.6 to 3.8 are essentially the same as 3.1 to 3.3 with the exception of two extra terms in 3.7 and 3.8. The extra term in 3.7 represents an additional shear stress produced by time averaged interactions of the turbulent momentum fluctuations. This additional correlation is called the Reynolds or turbulent stress. Similarly, the extra term in

equation 3.8 represents an additional heat flux produced by the time averaged interaction of enthalpy and momentum. This heat flux is called the turbulent heat flux.

Unfortunately, Equations 3.6 to 3.8 do not form a closed set because the turbulent shear stress and heat flux are unknown quantities. A further manipulation and time averaging process could produce differential equations for the unknown correlations but the nonlinear nature of the equations simply produces unknown higher order correlations. The determination of turbulent shear stresses and heat fluxes is commonly known as the closure problem.

Solutions for Equations 3.6 to 3.8 are obtained by artificial closure of the set of equations. Artificial closure is obtained by approximating the behavior of the unknown correlations. The wide variety of available approximations are known as turbulence models. Some detailed, critical reviews of turbulence modelling are provided by Rodi [46], Nallasamy [49], Patel, Rodi and Scheuerer [50] and Hirata, Tanaka, Kawamura and Kasagi [51].

The well known, semi-empirical k- ϵ model is used in this study. This model, proposed by Jones and Launder [52], begins by using the Boussinesq approximation to model the turbulent shear stress and, via Reynolds analogy, the turbulent heat flux. The Boussinesq approximation suggests that turbulent shear stress behaves like laminar shear stress except with a different viscosity. This viscosity is referred to as the eddy or turbulent viscosity, μ_T . Equations 3.9 to 3.11 reflect this idea.

$$-\overline{\rho u_i u_j} = \mu \left(\frac{\partial u_i}{\partial x_j} + \frac{\partial u_j}{\partial x_i} \right) - \frac{2}{3} \rho k \delta_{ij} \quad (3.9)$$

$$-c_p \rho \overline{u_i T'} = \frac{\mu_T}{\sigma_k} \left(\frac{\partial T}{\partial x_i} \right) \quad (3.10)$$

$$k = \frac{1}{2} (\overline{u_i u_i}) \quad (3.11)$$

An exact differential equation for the turbulent kinetic energy, k , may be obtained using time averaging procedures. This is given by Equation 3.12.

$$\frac{\partial k}{\partial t} + U_i \frac{\partial k}{\partial x_i} = -\frac{\partial}{\partial x_i} \left[u_i \left(\frac{u_i^2}{2} + \frac{p}{\rho} \right) \right] - \overline{u_i u_j} \frac{\partial U_i}{\partial x_j} - \nu \overline{\left(\frac{\partial u_i}{\partial x_j} \right)^2} \quad (3.12)$$

Each of the terms in Equation 3.12 have physical interpretations. These are, from left to right, rate of change (following the mean motion), diffusive transport, production by shear and viscous dissipation, ϵ , of turbulent kinetic energy. Note the high order correlations referred to earlier. A similar exact equation can be derived for the viscous dissipation, ϵ , of turbulent kinetic energy. The presence of higher order correlations propagates the closure problem. But the physical nature of each term in Equation 3.12 and in the dissipation equation permits reasonable approximation of these terms. The k and ϵ equations, as used in this study, are modelled semi-empirically as Equations 3.13 and 3.14 respectively.

$$U_i \frac{\partial k}{\partial x_i} = \frac{\partial}{\partial x_i} \left(\frac{\nu_{eff}}{\sigma_k} \frac{\partial k}{\partial x_i} \right) + \nu_{eff} \left(\frac{\partial U_i}{\partial x_j} + \frac{\partial U_j}{\partial x_i} \right) \frac{\partial U_i}{\partial x_j} - \epsilon \quad (3.13)$$

$$U_i \frac{\partial \epsilon}{\partial x_i} = \frac{\partial}{\partial x_i} \left(\frac{\nu_{eff}}{\sigma_\epsilon} \frac{\partial \epsilon}{\partial x_i} \right) + C_1 \nu_{eff} \left(\frac{\partial U_i}{\partial x_j} + \frac{\partial U_j}{\partial x_i} \right) \frac{\partial U_i}{\partial x_j} - C_2 \frac{\rho^2}{k} \quad (3.14)$$

where

$$\nu_{eff} = \frac{(\mu + \mu_T)}{\rho} \quad (3.15)$$

By dimensional analysis [46], ϵ is related to k and a dissipation length scale, l by

$$\epsilon \propto \frac{k^{3/2}}{l} \quad (3.16)$$

Combining this with the empirical Kolmogorov-Prandtl relation $\mu_T \cong C_\mu(k^{1/2}l)\rho$ yields

$$\mu_T = \frac{c_\mu \rho k^2}{\epsilon} \quad (3.17)$$

The empirical constants appearing in Equations 3.13, 3.14 and 3.17 are summarized in Table 3.1.

Table 3.1 Empirical Constants for the $k - \epsilon$ Model

C_μ	C_1	C_2	σ_k	σ_ϵ	κ
0.09	1.44	1.92	1.00	$\frac{\kappa^2}{(C_2 - C_1)C_\mu^{1/2}}$	0.4187

These constants have been found by ensuring the equations describe a number of simple flows, eg. boundary layers. The particular values used here are suggested by Anderson, Tannehill and Pletcher [43]. These values are typically used for boundary layer flows and are not varied in any way in this study. It should be noted, however, that these constants are strongly flow dependent. If the flow deviates far from a boundary

layer flow use of these values may adversely affect the solution. Equations 3.6 to 3.17 form a closed set which can be solved, using numerical techniques, for a given set of boundary conditions.

3.2 Problem Definition

The three numerical models discussed in the following sections represent three cases of increasing complexity. The physical boundary conditions are outlined here for each model.

3.2.1 The Heated Flat Plate

The heated flat plate in zero pressure gradient flow is a classical problem. The laminar flow problem is one of the few cases for which Equations 3.1 to 3.3 have simple solutions [40]. The turbulent case has also been studied thoroughly [40,53]. The physical layout of the flow domain is shown in Figure 3.1.

The boundary conditions are specified as follows:

- i) At the inlet, (AB), values of all principal variables, except pressure, are specified. For the laminar flow case, uniform profiles of streamwise velocity, U , and enthalpy, H , are used while the normal velocity, V , is set to zero.

The turbulent flow case uses profiles of U , H and k interpolated from the experimental results of M.F. Blair [53]. The normal velocity, V , is set to zero as a convenient approximation in the turbulent calculation. The dissipation, ϵ , is

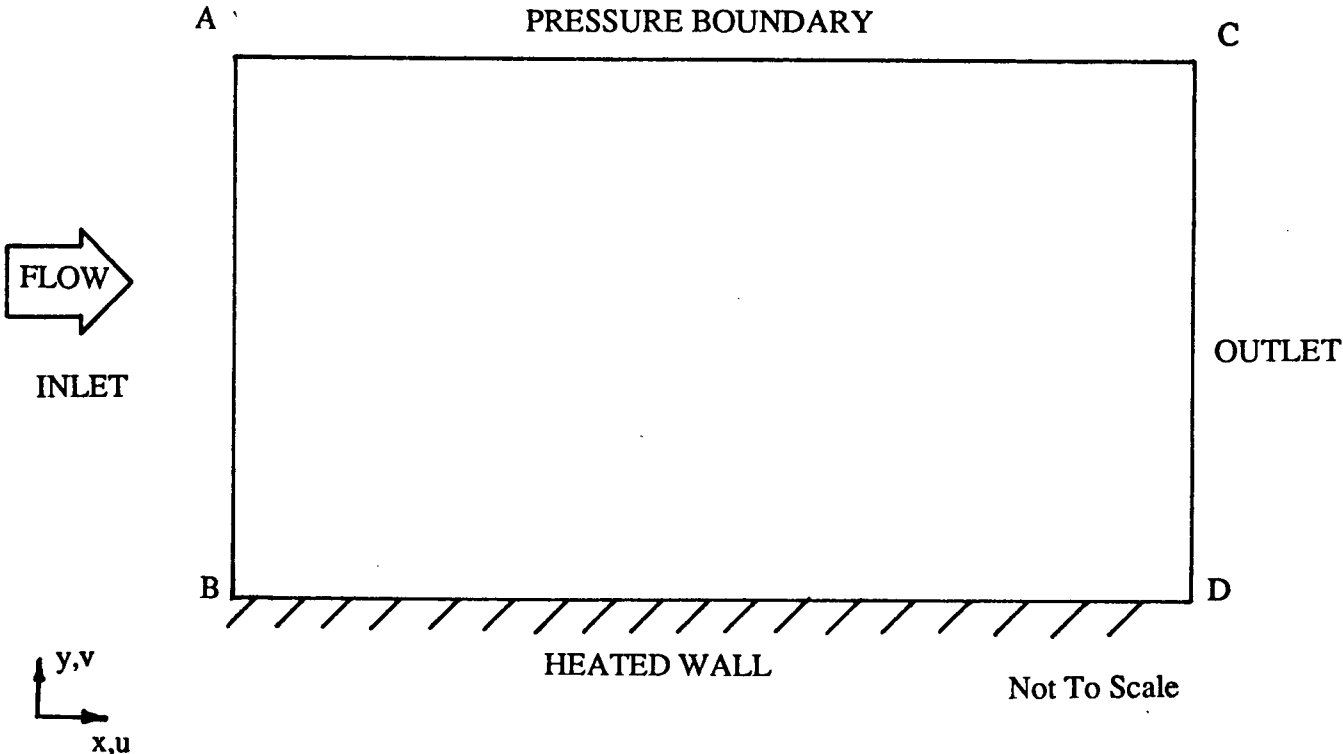


Figure 3.1 Flow domain for the heated flat plate problem

estimated from k and a characteristic length scale, namely the boundary layer thickness, $\delta_{.995}$, at the inlet.

- ii) At the outlet, (CD), zero streamwise gradients are used as outlet conditions for all variables, e.g. $\frac{\partial \phi}{\partial x} = 0$. This boundary condition, although strictly incorrect, can be used as an approximation for flows which are still developing as long as the outlet is positioned 'far enough' away from the region of interest. A position 'far enough away' is one which does not affect the solution in the region of interest. Such positions are found by trial and error.
- iii) At the 'pressure axis', (AC), a zero streamwise pressure gradient boundary condition is imposed, i.e. $\frac{\partial p}{\partial x} = 0$. This is achieved by specifying a uniform streamwise pressure distribution. The normal velocity, V , can not be imposed when the pressure is imposed. Thus, a cross stream normal velocity gradient exists which allows mass and momentum to penetrate the pressure axis. All other variables are assumed to satisfy a zero cross-stream gradient condition, e.g. $\frac{\partial \phi}{\partial y} = 0$. This latter assumption is appropriate as long as the 'pressure axis' is located outside the boundary layer.
- iv) At the heated wall, (BD), the no-slip boundary condition is imposed for the streamwise velocity, U , while the normal velocity, V , is set to zero. Temperature boundary conditions are imposed in the source terms of the cells adjacent to the wall. A uniform wall temperature is used for the laminar flow calculation.

For turbulent flow, the no-slip boundary condition involves a special treatment of the near wall region. The k - ϵ model is derived for fully turbulent

flows without viscous effects. Clearly, this is not the case near a wall where viscous effects dominate the flow. Launder and Spalding [54] have developed a near wall treatment that uses the universal law of the wall to calculate the wall shear stress. This shear stress is then used to impose the effect of the wall in the source term of the adjacent cell. A specified, uniform heat flux is imposed at the wall for the turbulent heat transfer calculation. The heat flux used here corresponds to that of M.F. Blair's experiments. This heat flux is imposed in the source terms of the cells adjacent to the wall. For non-dimensionalization of the results, the wall temperature is calculated using Reynolds analogy to extend the near wall treatment to the energy equation.

The use of wall functions has the benefit of reducing the number of computational cells required to resolve the near wall region. Large gradients typically found in this region would otherwise require many cells for resolution and a low Reynolds number model for computation of the near wall turbulence.

3.2.2 The Flush, Inclined Slot

The flow domain of the inclined flush slot is shown in Figure 3.2. This flow domain is very similar to that of the heated flat plate. The only difference is the presence of a slot opening in the solid wall. The pressure axis, solid wall and outlet boundary conditions are the same as those in the turbulent heated flat plate problem. The inlet and slot boundaries are the only ones that need further elaboration:

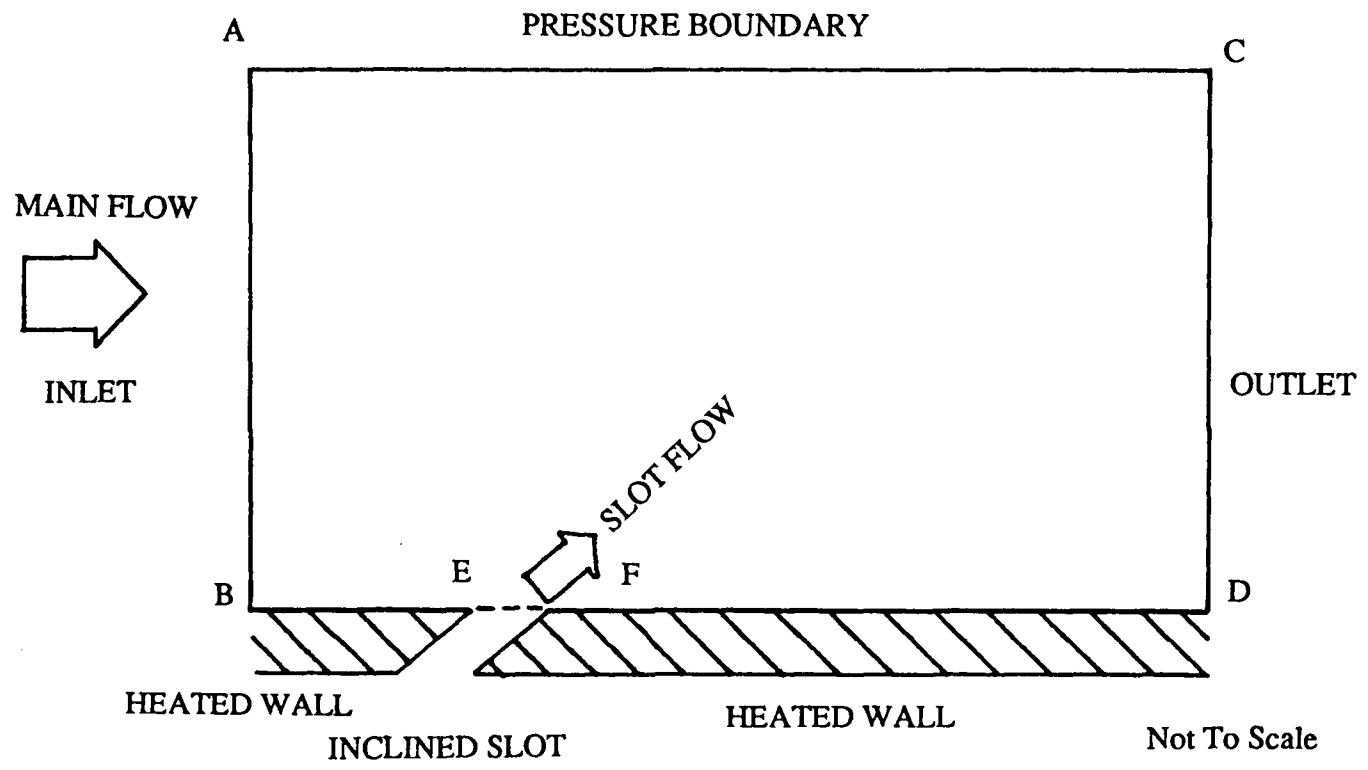


Figure 3.2 Flow domain for the flush, inclined slot problem

- i) At the inlet boundary, (AB), values of U , V , H and k are specified. The turbulent profiles of streamwise velocity, U , and turbulent kinetic energy, k , are interpolated from the experimental results of section 2.3. The normal velocity, V , is set to zero as a convenient approximation. The enthalpy, H , is assumed to follow a 1/7th power law. The energy dissipation, ϵ , is estimated by k and a characteristic length scale, namely the boundary layer thickness, $\delta_{99.5}$, at the inlet.
- ii) At the slot boundary, (EF), values of U , V , H and k are specified. Values of U , V and k are interpolated from the experimental results of section 2.3. The enthalpy, H , of the slot flow is assumed to be uniform across the slot such that the coolant and wall have the same temperature. The energy dissipation, ϵ , is estimated from the turbulent kinetic energy, k , and a characteristic length scale, namely the slot width, s .

As discussed in section 2.3, the direction of the measured slot velocity vectors is unknown. For these numerical experiments, three distributions of flow direction are assumed across the slot to obtain interpolated U and V velocities. These arbitrary distributions are shown in Figure 3.3.

The uniform distribution of Figure 3.3a assumes the flow angle is the same as the slot angle. This assumption reflects the practice of other researchers, namely Bergeles et al [31, 32, 33], Demuren et al [34] and Yavuzkurt et al [35].

The nonuniform distributions are obtained by using an integral condition of the mass flow with the plenum as a control volume. The points marked 'A' and 'B' in Figures 3.3b and 3.3c are obtained from the slot velocity profiles of Figures 2.15 and 2.16. Figure 3.4 illustrates the location of these points for $\alpha = 40$ degrees and $M = 0.91$. The features of these distributions and their effects on the flow calculations are further considered in section 4.2.

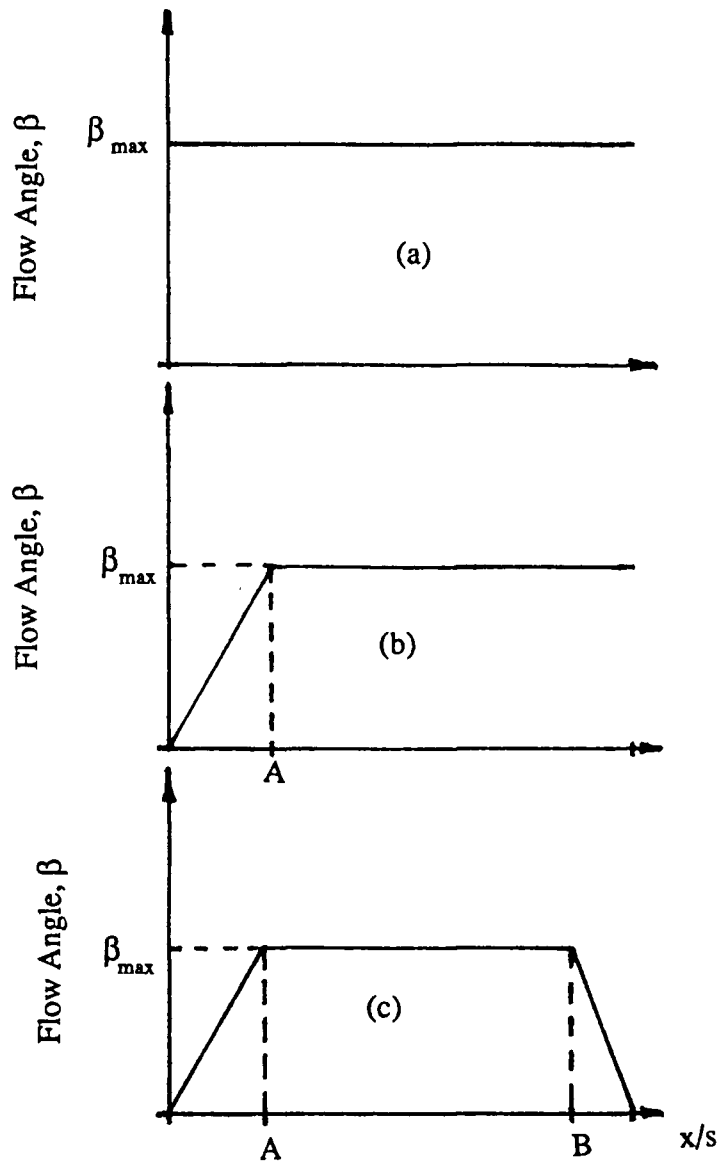


Figure 3.3 Various Schemes Used for the Angular Variation in the Slot
 (a) Uniform, (b) Linear-Uniform, (c) Linear-Uniform-Linear
 Note that $\beta_{\max} = \alpha$ for all case (a) calculations

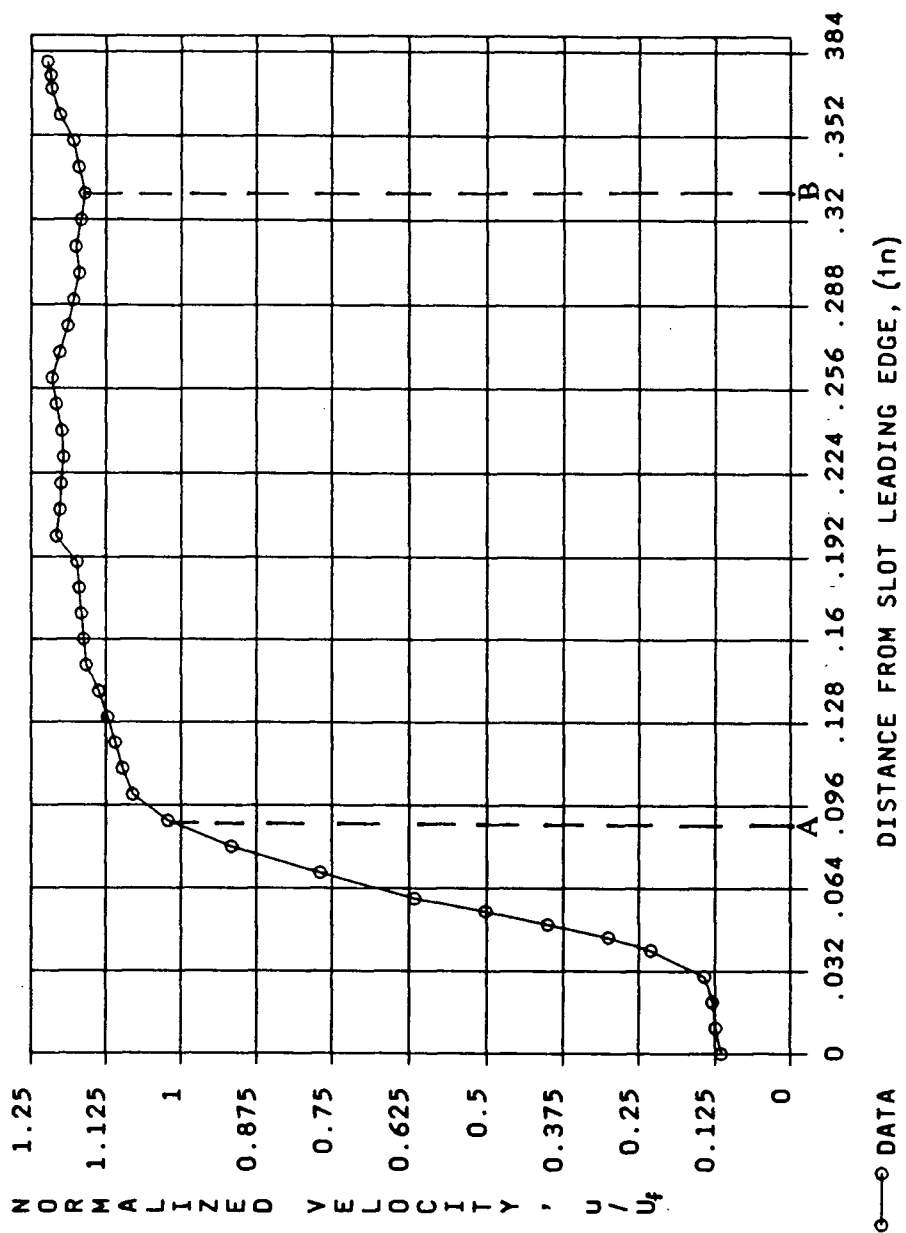


Figure 3.4 Location of points 'A' and 'B' for $\alpha = 40$ degrees and $M = 0.919$

The calculations with various flow angle distributions are made to test the sensitivity of the solution to the flow direction in the slot region. Since the flow directions near the slot were not measured directly, there is some ambiguity in the experimental velocity profiles. Hence it is desirable to calculate the complete flow from the plenum and through the slot. This calculation is described below, in section 3.2.3, for the simple case of injection normal to the freestream direction.

3.2.3 The Plenum-Mainstream Interaction

The flow domain for this calculation is shown in Figure 3.5. Unfortunately, time constraints limit this calculation to isothermal, laminar flow and normal injection. The boundary conditions employed at the pressure axis, solid wall, inlet and outlet are the same as those in the laminar heated flat plate problem. At the plenum inlet, (HJ), a uniform distribution is used for the V velocity and U is set to zero.

3.3 Method of Solution

The incompressible, two dimensional Navier-Stokes equations are solved with an implicit finite difference technique. The method of solution first involves discretizing the partial differential equations. Discretization is accomplished, in this case, with the bounded skew hybrid differencing (BSHD) technique developed by Lai and Gosman [55]. The resulting implicit finite difference equations are then solved iteratively using a multi-sweep tridiagonal matrix solver. In each iteration the coupling between the mass conservation equation and the transport equations is dealt with by a pressure implicit split operator technique developed by Issa [56]. The entire solution technique is incorporated in a computer code, TEACH-II, developed by Benodekar,

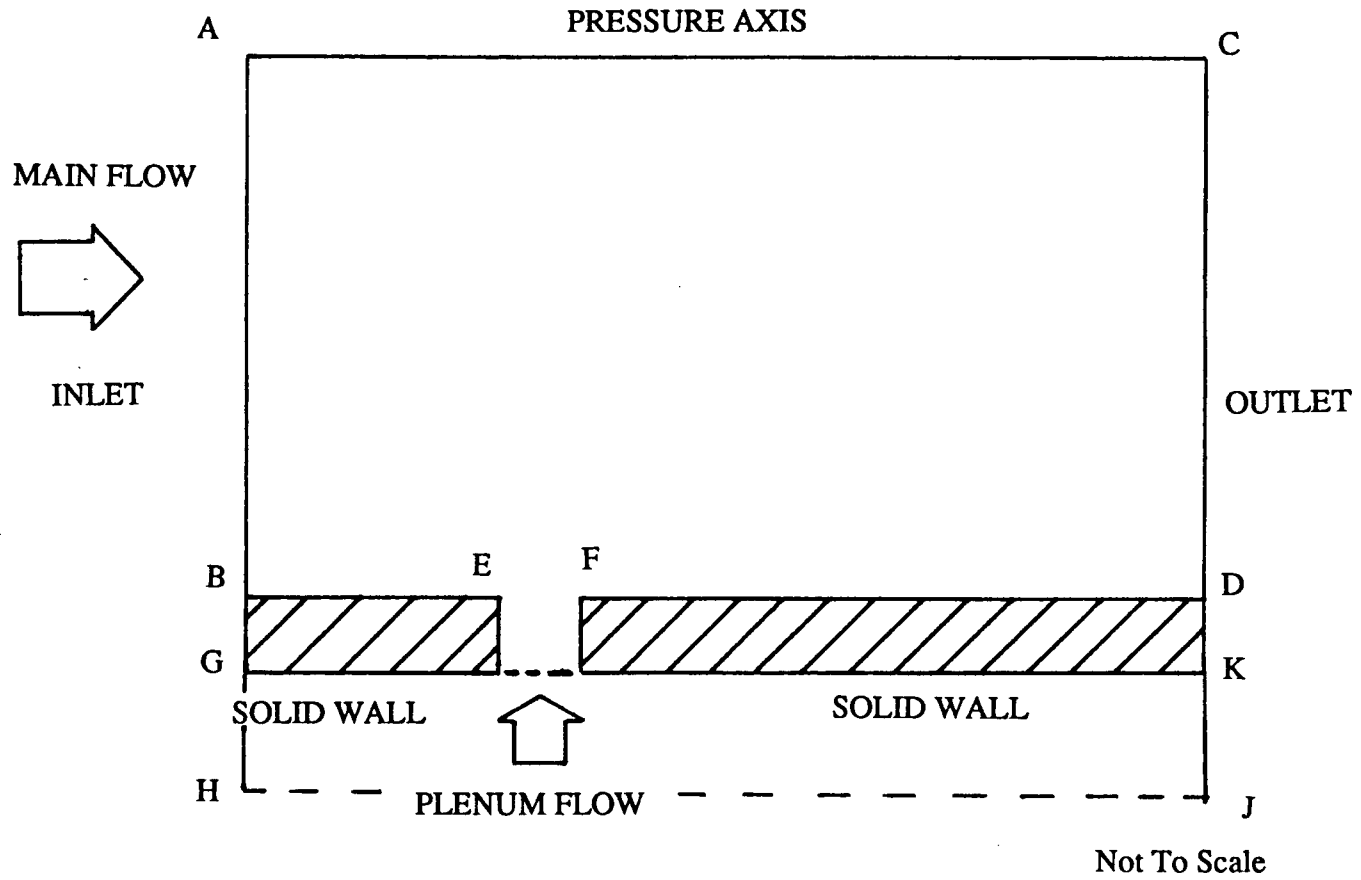


Figure 3.5 Flow domain for the plenum-mainstream interaction problem

Gosman and Issa [57]. This program is well known so only the main features are outlined here.

3.3.1 Main Features of the Computer Code

In the Teach-II code, the physical flow domain is divided into a finite number of control volumes. When the conservation equations are solved in the domain, they are applied to each control volume. The Teach-II code employs a staggered grid system where the control volumes for streamwise velocity, normal velocity and pressure, (or scalar quantities), are staggered. The relative orientation of these grids is shown in Figure 3.6.

The staggered grid is used because it allows the conservation of mass at each scalar cell to be represented with second order accuracy [43]. Furthermore, this technique is shown to eliminate unnatural oscillations of pressure between adjacent cells [58].

The staggered grid is placed so the edges of scalar control volumes coincide with physical boundaries. Fictitious cells, located outside the computational domain, are used to facilitate boundary condition implementation at solid walls.

The BSHD scheme is used because it improves accuracy by reducing the effect of false diffusion. This problem arises from the truncation error of first order differencing schemes. Since the truncation error for such a scheme is of second order, the error term behaves analogously to a second order diffusive flux and acts to diffuse steep gradients in the solution.

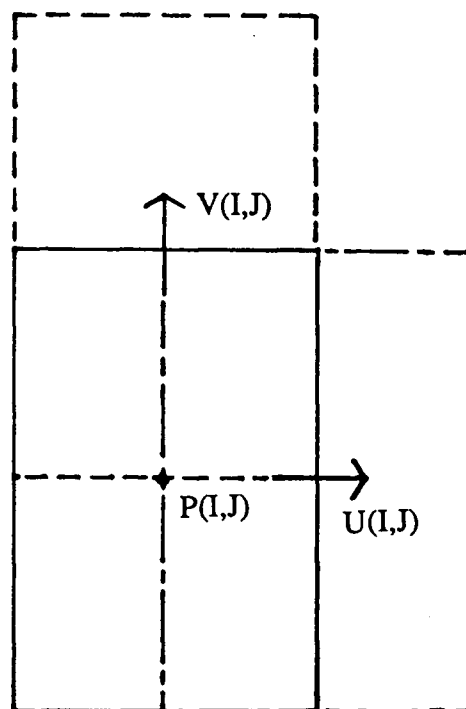


Figure 3.6 Relative locations of the staggered grids and calculated variables

Raithby [59], has shown that false diffusion is significant only when flow is skewed to the grid or when steep gradients exist in the flow. The BSHD scheme produces less false diffusion because it is a second order accurate scheme with a third order truncation error. A summarized derivation of the BSHD scheme is given by Benodekar, Goddard, Gosman and Issa [60].

The PISO algorithm developed by Issa [56] is a two-stage predictor-corrector procedure. This method provides a non-iterative means of separating operations on pressure and velocity variables. The coupling of these variables in the transport equations is difficult and expensive to deal with when semi and fully implicit solution schemes are used. By separating operations on the pressure and velocities at each stage of the procedure, a set of equations in terms of a single variable, namely U, V or P, is obtained. Each set of equations is easily solved using standard techniques. The splitting operation is repeated twice to ensure mass conservation. The same operator splitting procedure is used to deal with the coupling of the source terms in the calculation of the k and ϵ fields.

The PISO algorithm has been modified in the present study to allow imposition of pressure boundary conditions at the pressure axis of the flow domain. In the cells where the pressure is imposed the velocities and scalar quantities are not corrected with each recalculation of the pressure field. A second modification is the addition of the streamline curvature correction to the k- ϵ model. This correction, recommended by Leschziner and Rodi [61], involves an empirical recalculation of the constant C_μ . The correction is given by Equation 3.1.

$$C_\mu = \max \left\{ 0.025, \frac{0.09}{1 + 5.7(k/\epsilon)^2 (du_s/dn + u_s/R_c) u_s/R_c} \right\} \quad (3.1)$$

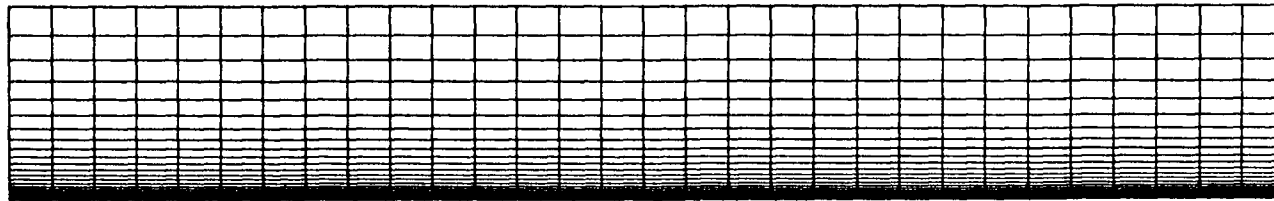
where u_s is the velocity tangential to the streamline, n is the normal coordinate and R_c is the radius of curvature.

The boundary conditions for the computations at the wall are imposed with a standard technique which imposes additional source terms in the cells adjacent to the boundary while cancelling convective and diffusive fluxes from the boundary. This method is described in detail by Anderson, Tannehill and Pletcher [43].

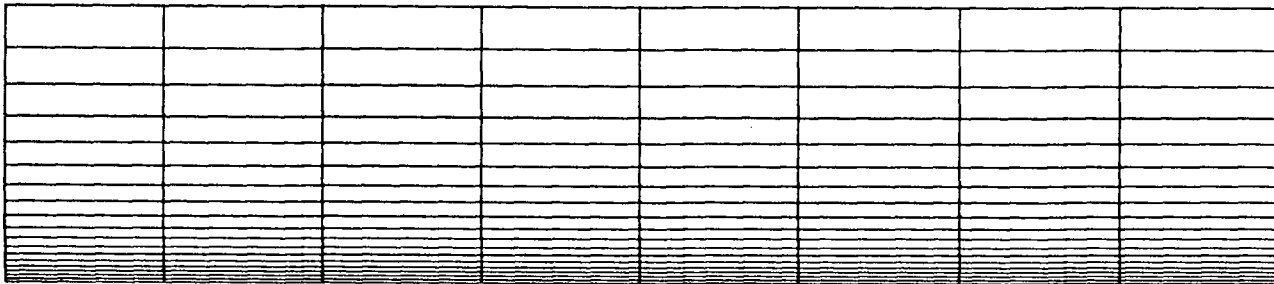
3.3.2 Grid Selection

The selection of a poorly refined numerical grid may adversely affect convergence of the numerical solution. Figures 3.7, 3.8 and 3.9 show typical scalar grid distributions used for the flat plate, inclined slot and plenum-mainstream flow domains.

The grid distributions in these figures are obtained through a trial and error series of tests. In each series of tests, the grid in question is progressively refined until the numerical solution is essentially unaffected by further refinements. The graph of Figure 3.10 illustrates the results of these tests for the flush, inclined slot. Each curve in the graph represents the variation of the converged solution with varying refinement of the flow domain. Clearly the effect of refining the grid, in this case, beyond the 60 by 20 mesh is marginal.

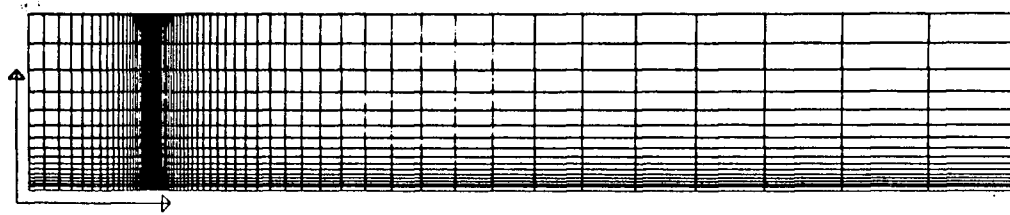


(a)

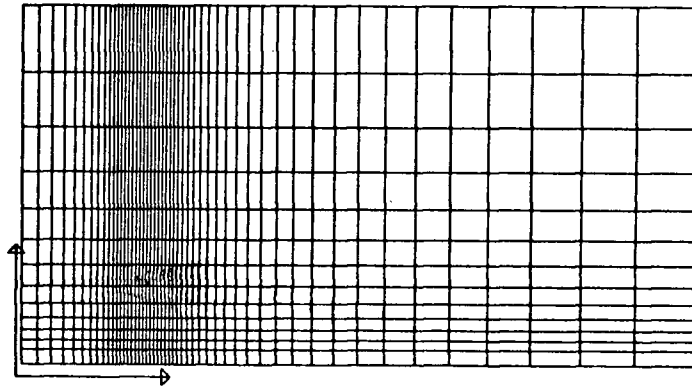


(b)

Figure 3.7 Typical numerical grid for the heated flat plate problem
(a) Entire Grid (b) Closeup of Refined Region



(a)



(b)

Figure 3.8 Typical numerical grid for the flush, inclined slot problem
(a) Entire Grid (b) Closeup of Refined Region

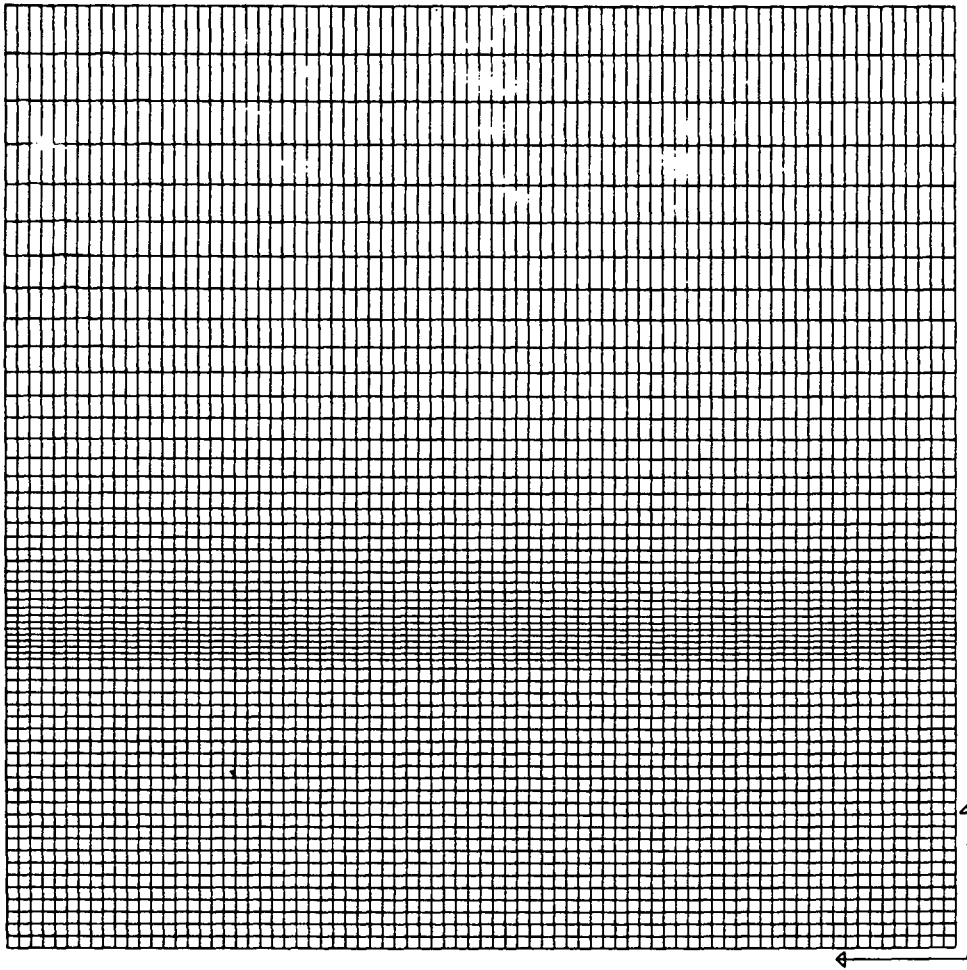


Figure 3.9 Typical numerical grid for the plenum-mainstream interaction

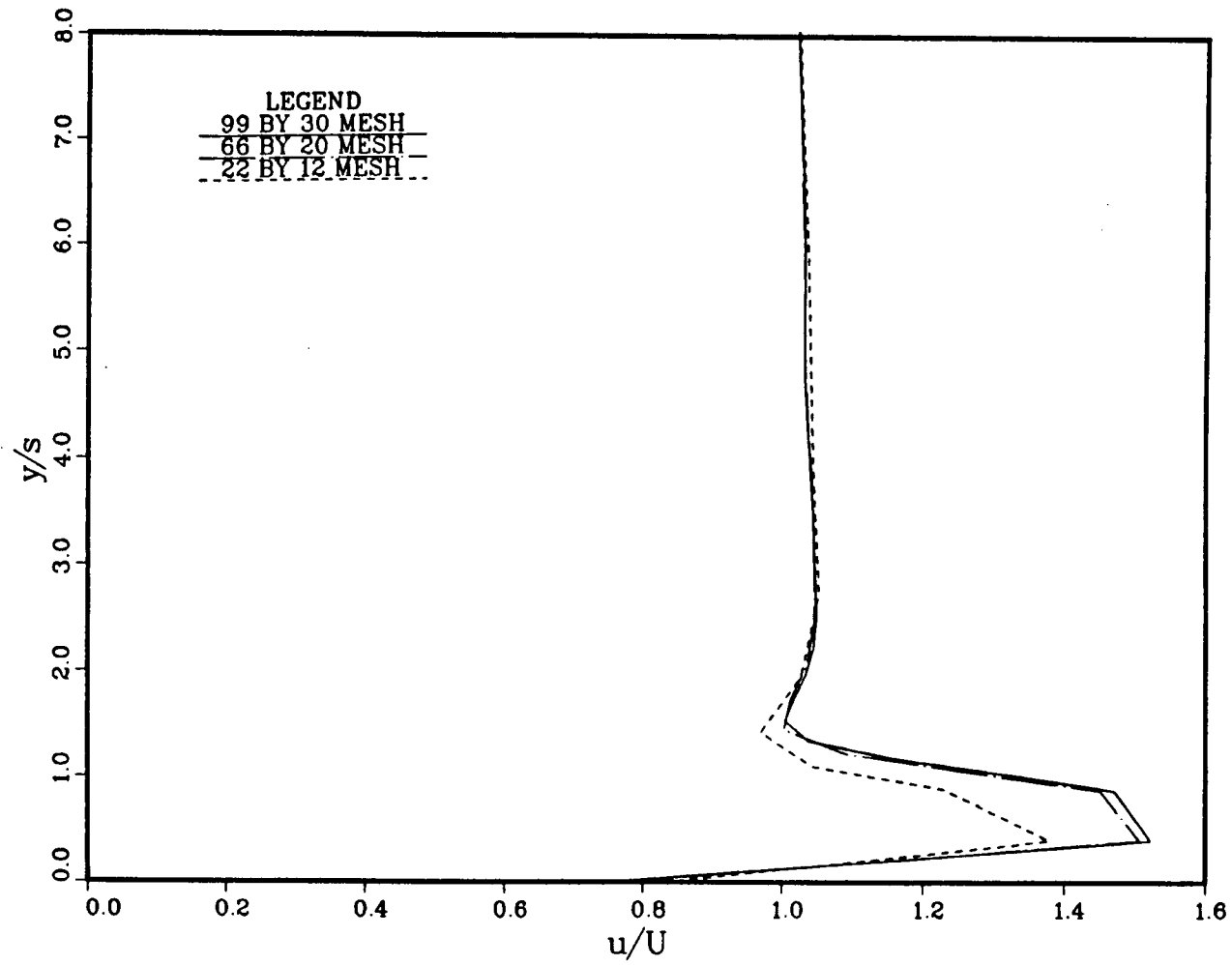


Figure 3.10 Demonstration of grid independence for the flush, inclined slot problem

4.0 Results and Discussion

*"As we acquire more knowledge, things do not become more
comprehensible but more mysterious."*

Albert Schweitzer

In this chapter, the qualitative and quantitative features of the numerical calculations are examined. Whenever possible, these predictions are compared with experimental measurements and well known correlations. Before presenting results pertinent to film cooling, the predictions for simple flat plate boundary layers are discussed.

4.1 The Flat Plate

This classical flow is examined as a test case, of the computer code, for two reasons. Firstly, flat plate boundary layers have been extensively studied and accurate results exist for both laminar and turbulent cases. Secondly, the flush inclined slot geometry of section 3.2.2 is a direct extension of the flat plate. The ability to predict flat plate boundary layer behavior may have a direct bearing on the ability to predict the flow and heat transfer behavior of fluid issuing from a flush, inclined slot.

4.1.1 Laminar Flow and Heat Transfer

The ability to predict laminar flow and heat transfer reflects the accuracy of the equations, boundary conditions and solution technique. The equations employed here are the fully elliptic conservation equations, namely 3.1 to 3.3. The parabolic boundary layer equations are not used in this study because the same computer code is used to study boundary layers and recirculating flows.

The flow results presented here are for a laminar, zero pressure gradient boundary layer on a heated flat plate. The thermal boundary layer is calculated for the case of a uniform wall temperature and Prandtl number equal to one. Since the ratio $Gr_x/(Re_x)^2$ for the case at hand is 0.1, buoyancy effects are not included in the numerical model.

Typical velocity and temperature profiles midway along the plate are shown in Figures 4.1a and 4.1b respectively. In each case, the numerical result is compared with the classic Blasius similarity solution of the boundary layer equations [40]. Clearly, the agreement with the Blasius result is remarkable for both temperature and velocity. These results indicate that the boundary conditions, including the pressure boundary condition, are correctly imposed and the numerical technique is reliable.

4.1.2 Turbulent Flow and Heat Transfer

For turbulent flow, turbulence models must be used to approximate the second order correlations of equations 3.10 and 3.11. The model used here is the standard k- ϵ model described in section 3.1. Calculation of a boundary layer is a good test of the k- ϵ model because the empirical constants used here are derived from boundary layer flows.

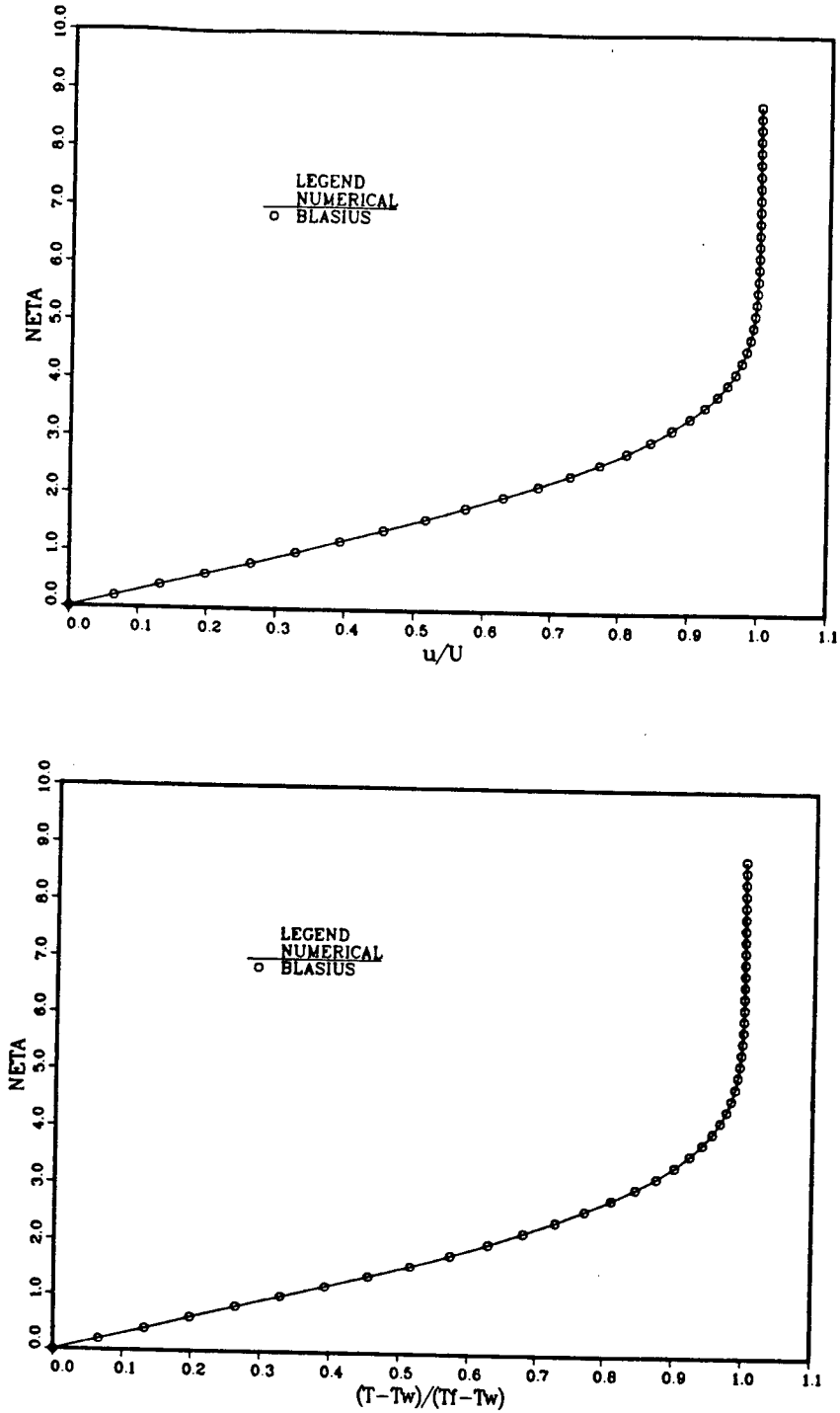


Figure 4.1 Laminar Boundary Layer Velocity and Temperature Profiles for $x/L = 0.5$

As such, the momentum boundary layer features should be accurately predicted by the numerical model.

The thermal boundary layer features, however, may not be as accurately predicted. The Reynolds analogy, with a constant turbulent Prandtl number, is used to predict the turbulent heat transfer. Since the turbulent Prandtl number has been reported to vary by a number of researchers [53, 62], the turbulent heat transfer predictions should be somewhat less reliable than the momentum boundary layer features.

The flow calculations presented here represent a turbulent, zero pressure gradient boundary layer on a heated flat plate. The thermal boundary layer development is presented for a specified, uniform wall heat flux boundary condition and a turbulent Prandtl number of 0.9. Since the ratio $Gr_x/(Re_x)^2$ is 0.0000057, buoyancy effects are not included in the numerical model.

In the following discussion, comparisons are made for two different numerical calculations. The first case, that of M.F. Blair [53], allows assessment of the mean velocity and temperature field predictions. The numerical model for this case uses experimental measurements of U, T, k and q_w for the inlet and wall boundary conditions. The second comparison case is that of a flat plate with turbulent flow from the leading edge in zero pressure gradient with uniform wall heat flux. This second case allows assessment of predictions in the wall region, namely predictions of C_{fx} and St_x . The numerical results for this case are compared with correlations from Schlichting [40].

The mean velocity predictions corresponding to Blair's data are shown in Figure 4.2. The velocity results shown, for the two streamwise positions, indicate excellent agreement between the experimental measurements and numerical predictions. The largest difference in the two results occurs for the streamwise position $x/L = 0.84$. At this location, the numerically predicted velocities in the boundary layer are shown to be 3 percent higher than the measured velocities. This difference is not large and is

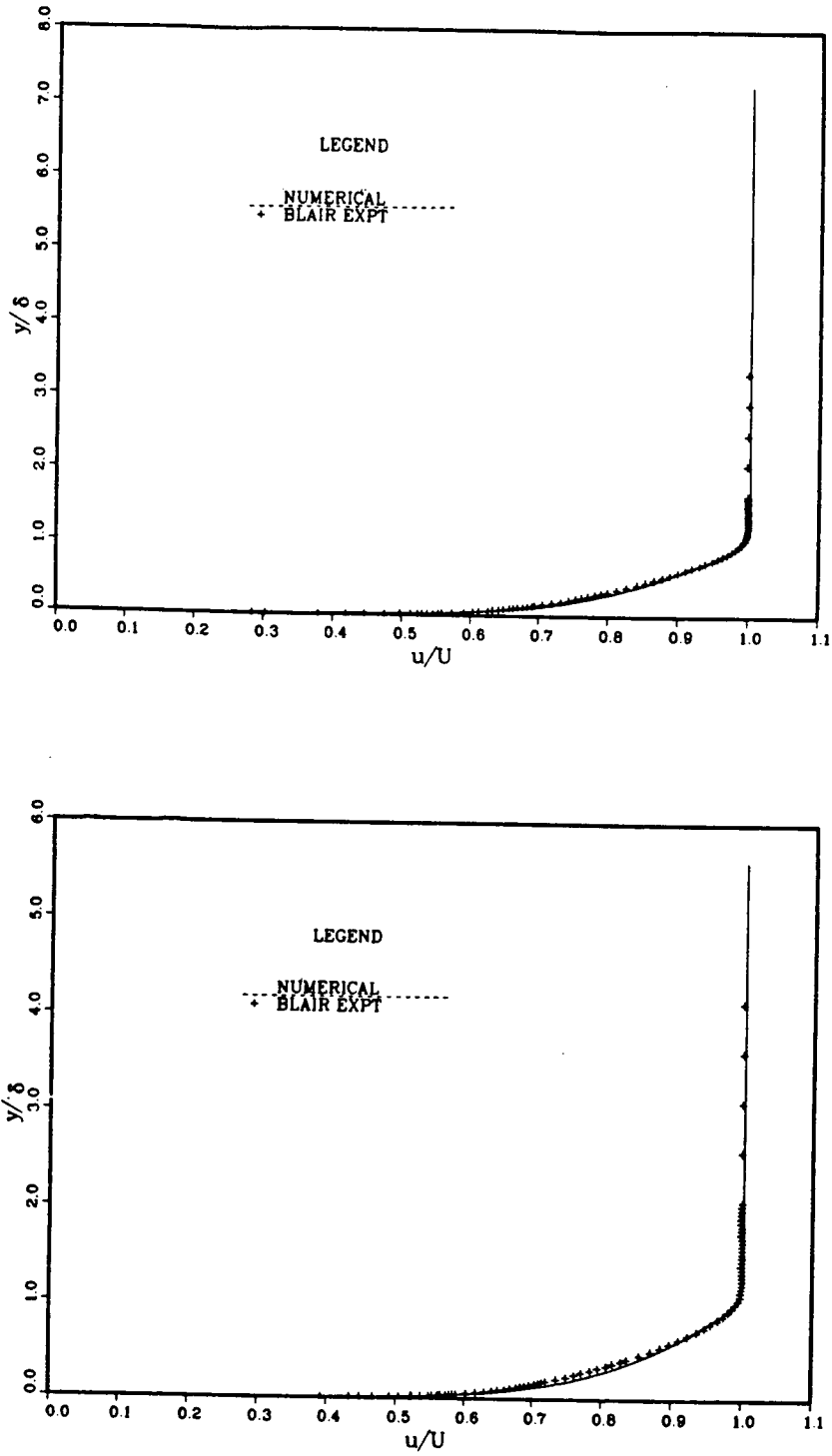


Figure 4.2 Turbulent Boundary Layer Mean Velocity Profiles for a) $x/L = 0.68$ and b) $x/L = 0.84$

within the experimental uncertainty of ± 5 percent quoted by Blair [53]. It is interesting to note that both numerical velocity profiles contain slightly more momentum than the experimental data. This may be due to the interpolation of Blair's data at the inlet and might account for the 3 percent maximum difference in predicted and measured values. It may also reflect a slight departure from two-dimensionality in the measurements. The slope of each numerical velocity profile near the wall seems to be in excellent agreement with the experimental data.

This agreement would indicate a good numerical prediction of the wall shear stress. Such a comparison is not made, however, because Blair offers only three streamwise values of the shear stress coefficient. These three values are extrapolated from his velocity profiles and are very dependant on the method of extrapolation. Instead, Figure 4.3 presents a comparison of the numerical and correlated shear stress coefficients for the second comparison case. Again, the agreement between the numerical prediction and the experimental correlation is very good. The largest difference in these two results is only about 3 percent. This difference may be due to the positioning of the numerical grid point adjacent to the wall. The position of this grid point is governed by the near wall model of Launder and Spalding [54]. This model requires that the first grid point be outside the laminar sublayer and the buffer region of the boundary layer i.e. at $30 < y^+ < 100$. This requirement may lead to poor resolution of the flow field very close to the wall. The numerical results of Figures 4.2 and 4.3 indicate, however, that the numerical technique used here is very suitable for the calculation of flow field features in a boundary layer.

The mean temperature predictions corresponding to Blair's data are shown for two streamwise positions in Figure 4.4. Although the experimental data show some scatter, overall agreement with the numerical result is good. The largest difference between the numerical and experimental results is seen in the profile corresponding to

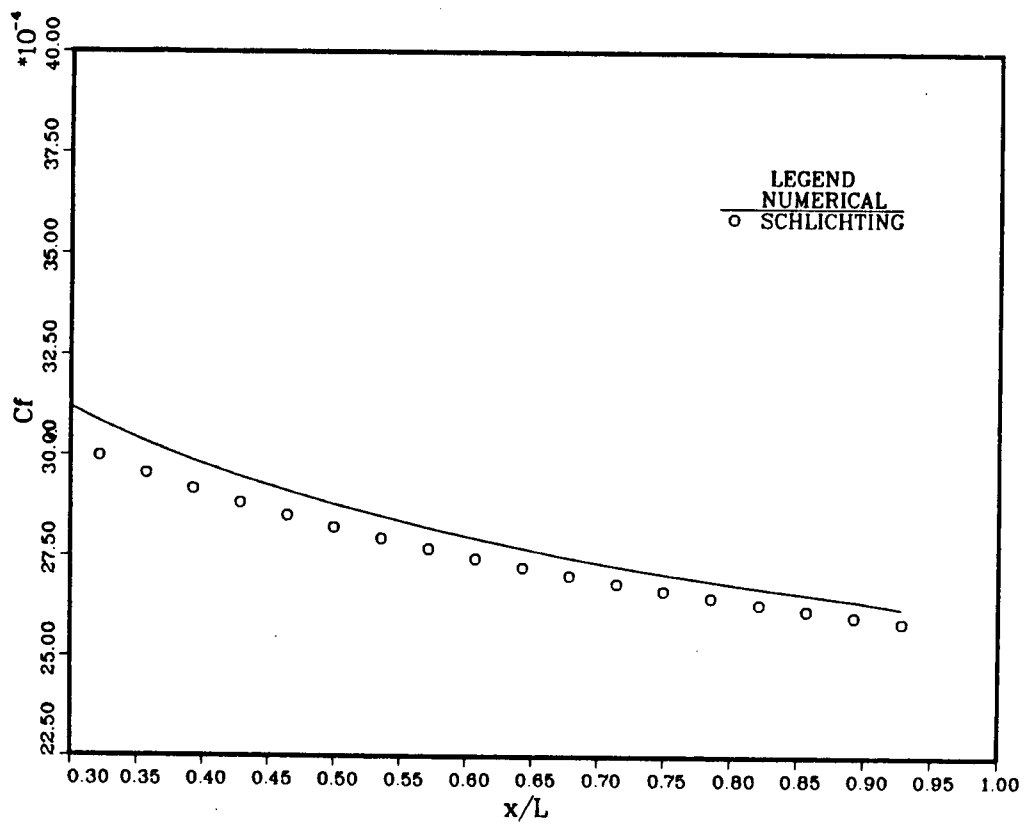


Figure 4.3 Turbulent Boundary Layer Variation of Shear Stress Coefficient

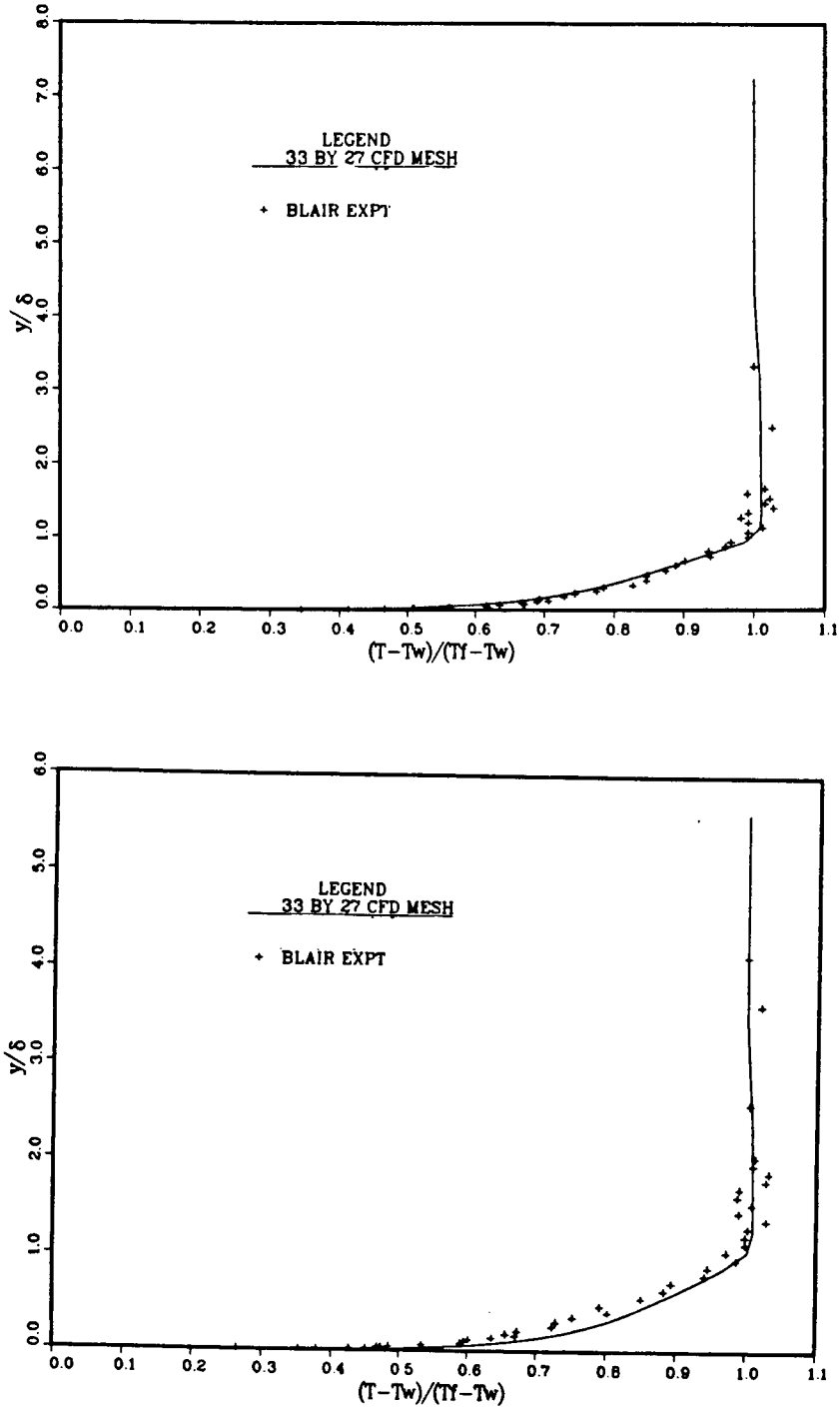


Figure 4.4 Turbulent Boundary Layer Mean Temperature Profiles at a) $x/L = 0.68$ and b) $x/L = 0.84$

$x/L = 0.84$. At this position, the numerical result consistently overpredicts the temperature near the wall by 3 to 5 percent. This observed difference may be a reflection of the experimental uncertainty.

In his error analysis, Blair states that "discrepancies in the mean temperature profile measurements were slightly larger than those for the velocity measurements with only 70 percent of the measurements falling within ± 5 percent" [53]. He goes on to show that his temperature measurement uncertainty with a hot wire probe varies linearly from ± 20 percent at $y/\delta_{995} = 0.005$ to ± 2 percent at $y/\delta_{995} = 1.04$. Blair attributes these errors to the size of the 3 wire probe used in his study [53].

Considering this error analysis, the mean temperature predictions of Figure 4.4 are well within experimental error. This result is very encouraging since it supports the thermal simplifications referred to earlier.

Figure 4.5 presents the Stanton number predictions for the second comparison case. Here, the numerical results compare favourably with correlated values from Eckert and Drake[63]. The largest difference between the two results is 17 percent. This comparison provides further evidence of the reliability of the turbulent heat transfer calculations. It should, however, be emphasized that the law of the wall is used to calculate the wall temperature (or heat flux for a constant temperature wall). As a result, the reliability of the heat transfer calculations may deteriorate if the flow deviates far from a boundary layer flow, e.g. if recirculation is present. The gradual deterioration of the Stanton number agreement, with increasing x / L , is evidence that Reynolds analogy is not strictly valid and the turbulent Prandtl number is not constant throughout the boundary layer.

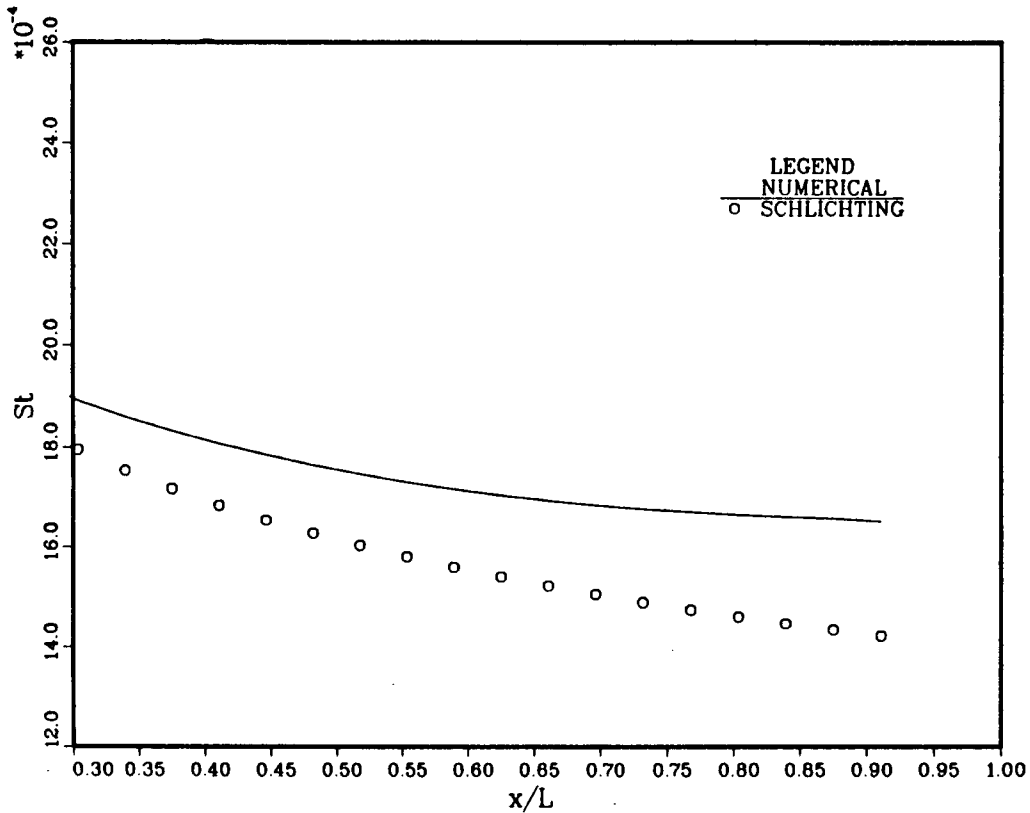


Figure 4.5 Turbulent Boundary Layer Variation of Stanton Number

4.2 The Flush, Inclined Slot

Having established the reliability of the numerical method for boundary layer flows, the primary objectives of this study may now be considered. Calculation of the flow and heat transfer in the vicinity of the flush inclined slot is one of the principal objectives of this study. The presentation of these results is separated into two sections. In section 4.2.1, the flow calculations are compared with the experimental results of Chapter 2. Section 4.2.2 examines some preliminary heat transfer results. The heat transfer results are considered preliminary because experimental data are not available for comparison. The detailed comparison of heat transfer results is left for future work.

The calculations presented in sections 4.2.1 and 4.2.2 correspond to a variety of flow conditions. For clarity, these conditions are summarized in Table 4.1. This table is reproduced in Appendix A, which should be detached for easy cross-reference. In viewing the following results, the reader should keep in mind the note in section 2.1.2.3 regarding M_{expt} .

The uniform and nonuniform distributions of flow angle in the slot are described in section 3.2.2. These various distributions are used in the calculations for several reasons. Firstly, the flow direction at the slot exit is not measured in this study. Secondly, experimental results, presented in section 2.3, indicate that this direction is not equal to the slot angle as assumed by previous researchers [31, 32, 33, 34 and 35]. Furthermore, as discussed in section 2.3, the assumption of a uniform flow angle equal to the slot angle does not always accurately represent the mass flow from the slot. Subsequently, calculations are presented to illustrate the effect of flow direction in the

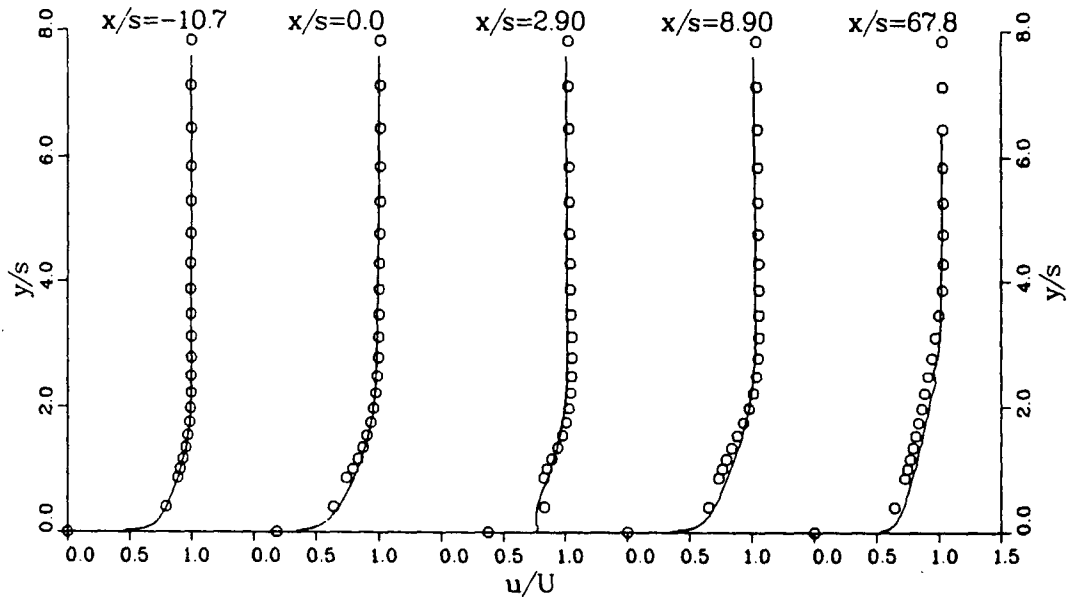
slot on the flow and heat transfer downstream of the slot. The discussions of flow and heat transfer calculations begin by presenting results for the uniform flow angle distribution and then consider the effect of more plausible flow angles.

Table 4.1 Tabulation of Various Flow Cases Used to Study the Flow and Sensitivity of the Flow to the Flow Angle Distribution in the Slot

Case Number	Slot Angle	M_{num}	M_{expt}	Flow Angle Distribution
201-U	20	0.53	0.46	Uniform
201-LU	20	0.46	0.46	Linear-Uniform
201-LUL	20	0.46	0.46	Linear-Uniform-Linear
202-U	20	0.85	0.90	Uniform
203-U	20	1.23	1.4	Uniform
203-LU	20	1.43	1.4	Linear-Uniform
203-LUL	20	1.43	1.4	Linear-Uniform-Linear
401-U	40	0.56	0.46	Uniform
401-LU	40	0.46	0.46	Linear-Uniform
401-LUL	40	0.46	0.46	Linear-Uniform-Linear
402-U	40	0.97	0.91	Uniform
403-U	40	1.28	1.2	Uniform
403-LU	40	1.24	1.2	Linear-Uniform
403-LUL	40	1.24	1.2	Linear-Uniform-Linear

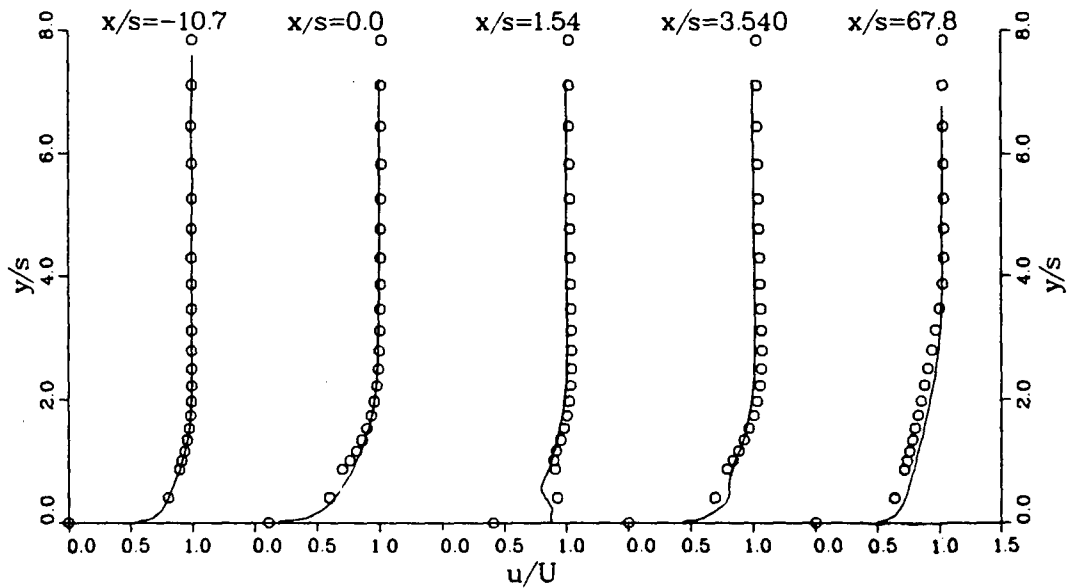
4.2.1 The Flow Field

Comparisons of numerical and experimental mean speed profiles, for 5 streamwise positions, are shown in Figures 4.6, 4.7, and 4.8. The numerical results presented therein use the measured mean and fluctuating speeds as inlet and slot



(a)

— EXPERIMENT
 ○ NUMERICAL



(b)

Figure 4.6 Comparison of Experimental and Numerical Mean Speed Profiles at 5 Streamwise Positions, for Mass Flow Ratio of 0.46 and x/s Measured from the Slot Leading Edge for a) the 20 degree slot and b) the 40 degree slot

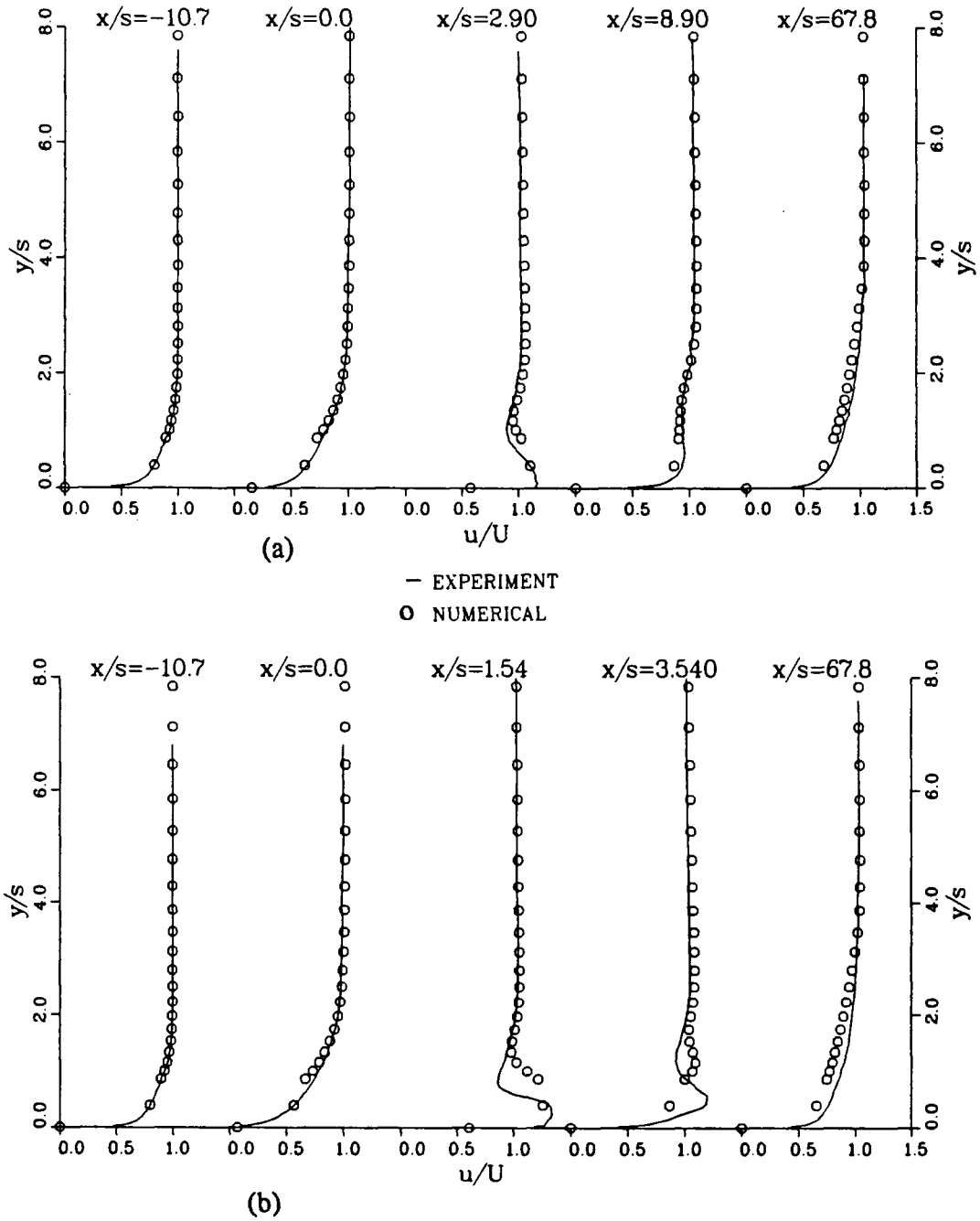


Figure 4.7 Comparison of Experimental and Numerical Mean Speed Profiles at 5 Streamwise Positions, for Mass Flow Ratio of 0.9 and x/s Measured from the Slot Leading Edge
 a) $\alpha = 20$ degrees and b) $\alpha = 40$ degrees

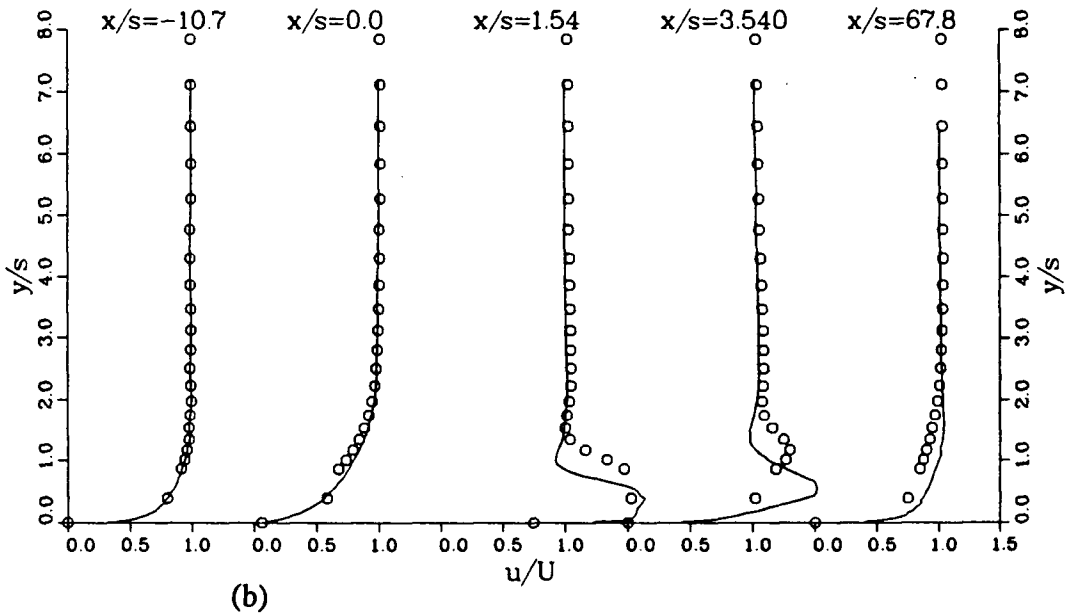
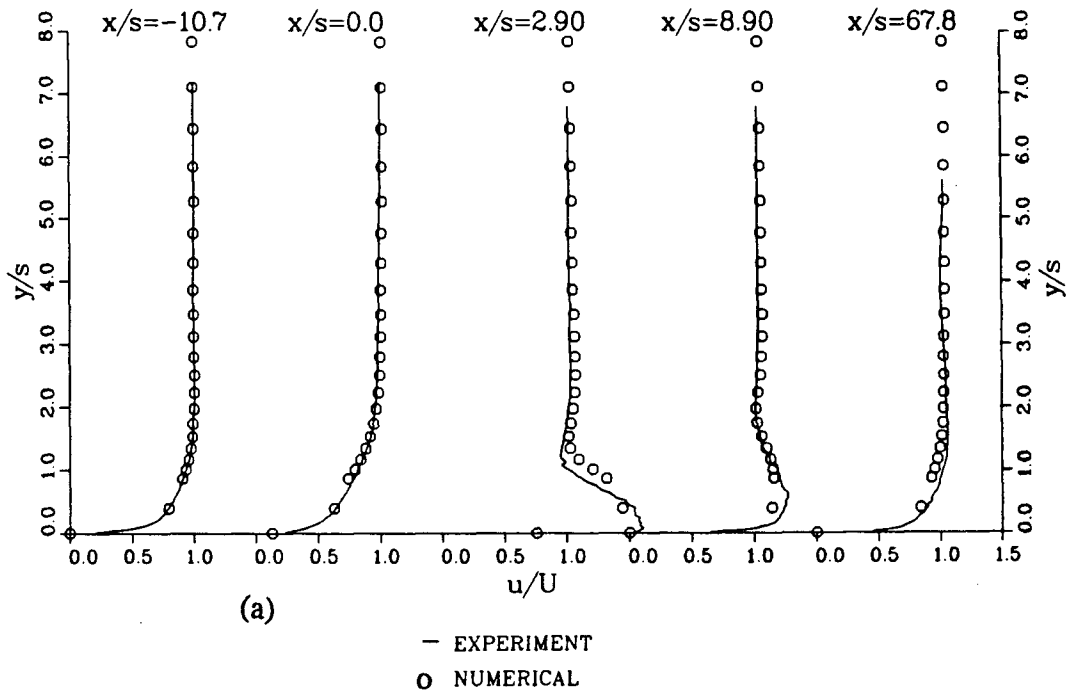


Figure 4.8 Comparison of Experimental and Numerical Mean Speed Profiles at 5 Streamwise Positions, for Mass Flow Ratio Near 1.3 and x/s Measured from the Slot Leading Edge
a) $\alpha = 20$ degrees and b) $\alpha = 40$ degrees

boundary conditions. The use of the slot mean speed profile raises the question of flow angle, discussed in section 2.3.3.

The numerical results of Figures 4.6 to 4.8 assume, in the absence of detailed measurements, that flow issues from the slot at the same angle as the slot itself. As mentioned in section 2.3.3, this assumption can have the effect of imposing an erroneous slot massflow in the numerical calculations. In particular, the calculations of cases 201-U, 203-U and 401-U are subject to this error.

Previous researchers, notably Bergeles et al [31, 32, 33] and Demuren et al [34], have assumed that both the speed and direction of the flow do not vary across the orifice. Although the numerical results in Figures 4.6 to 4.8 assume a uniform flow angle across the slot, the measured speed variation across the slot is included in the numerical model.

Regarding Figures 4.6 to 4.8, the quality of agreement between numerical and experimental results depends on the slot angle considered. The agreement for the 20 degree slot seems to be good for each of the flow cases. The numerical predictions for the 40 degree slot, however, can only be said to predict the qualitative features of the flow. The largest difference between numerical and experimental results ranges from 5 to 10 percent for the 20 degree slot and from 5 to 50 percent for the 40 degree slot. In each case, this difference appears at or near the slot trailing edge where the gradients are steepest, i.e. $x/s = 2.90$ and $x/s = 1.54$. As already noted, in section 2.1.2.3, work done subsequent to this thesis suggests the rotameter calibration was in error by 13 percent during the experiments. Since this error would have indicated a lower experimental slot mass flow, the calculated velocities can be expected to be approximately 13 percent higher than the experimental values. This possible source of error does not account for the large discrepancies noted here.

It is rather disappointing to note the combination of steep velocity gradients and poor numerical resolution near the wall, especially at the slot trailing edge.

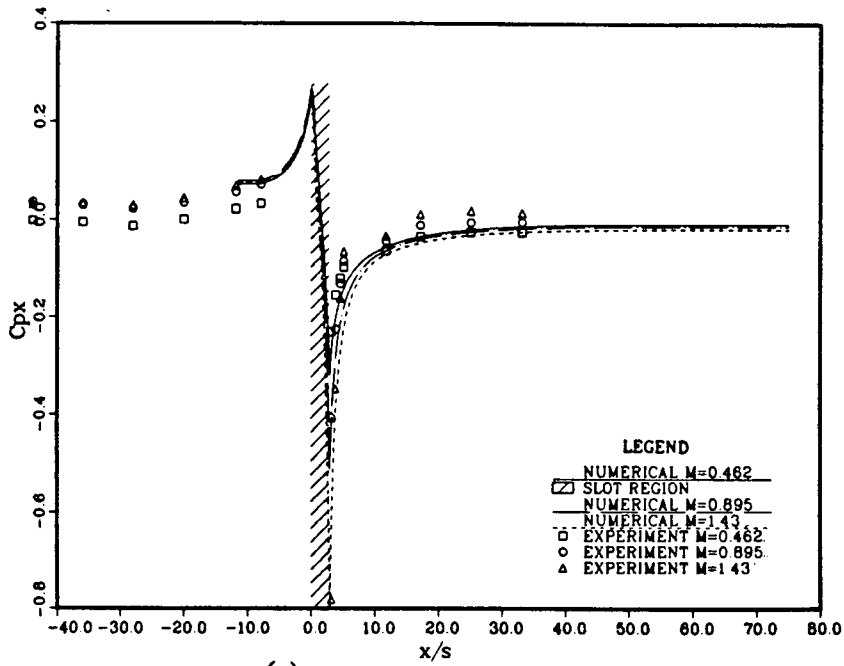
Unfortunately, the resolution of these gradients cannot be improved with the present near wall model. The location of the grid point closest to the wall is restricted to $30 < y^+ < 100$ for reasons given in section 4.1.2.

The observed discrepancies between the numerical and experimental results may be due, in part, to inaccurate modelling of the mass flow from the slot. According to section 2.3.3, however, cases 402-U and 403-U should not be subject to significant errors of this sort. That is, the cases showing the largest disagreement in results incorporate reasonable mass flow conditions at the slot. The effects of slot mass flowrate and flow angle are considered in the following discussion.

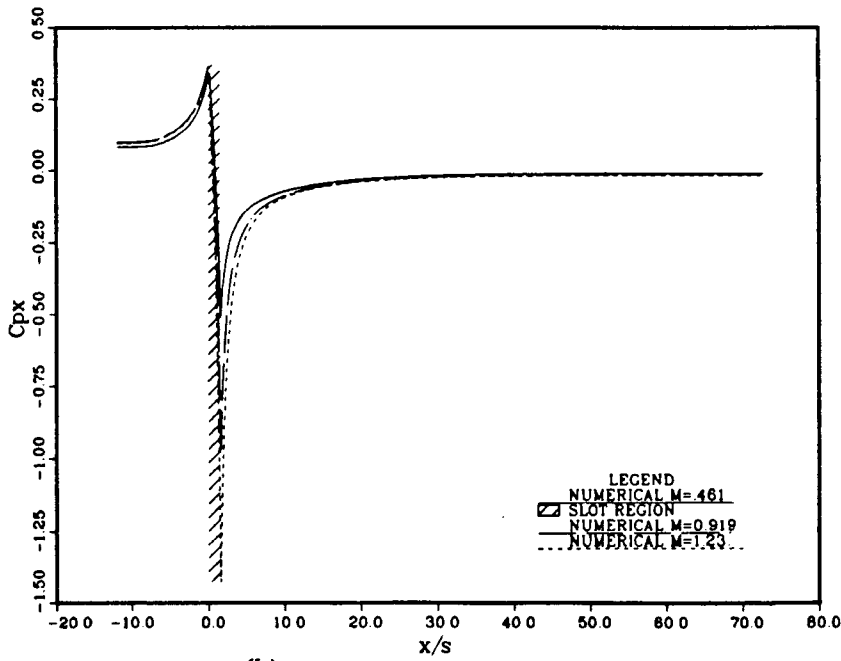
Regarding the 40 degree numerical results, for cases 402-U and 403-U in Figures 4.7 and 4.8, it is apparent that the predicted slot flow has penetrated to the same position for both mass flow cases. The point of predicted maximum velocity, namely $y/s = 1.1$ at $x/s = 3.54$, appears independent of the mass flow ratio. This behavior indicates that the slot flow, for high mass flow ratios, penetrates the mainstream as if it were a strong jet. This behavior (of the numerical flow) may be a consequence of the flow angle assumption at the slot.

The use of a uniform flow angle assumption for these flow calculations was expected to predict a recirculation region downstream of the slot trailing edge. The absence of separation from the numerical result may be due to the coarseness of the numerical grid near the wall since the first grid point is placed nominally 1 cm above the plate surface. Separation is not evident in the experimental results either and is very limited in extent, if it exists at all.

For completeness, the surface pressure coefficients and shear stress coefficients, for cases 201-U, 202-U, 203-U, 401-U, 402-U and 403-U are presented in Figures 4.9 and 4.10 respectively. Regarding Figure 4.9, the predicted surface pressure coefficients for the 20 degree slot are in reasonable agreement with the experimental measurements.



(a)



(b)

Figure 4.9 Surface Pressure Coefficients for a) the 20 degree slot and b) the 40 degree slot

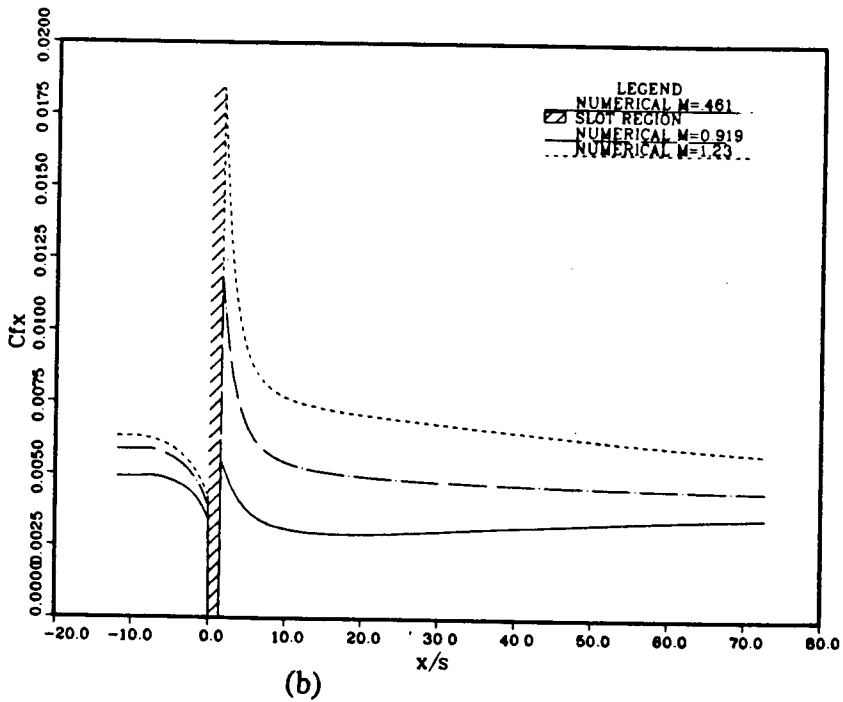
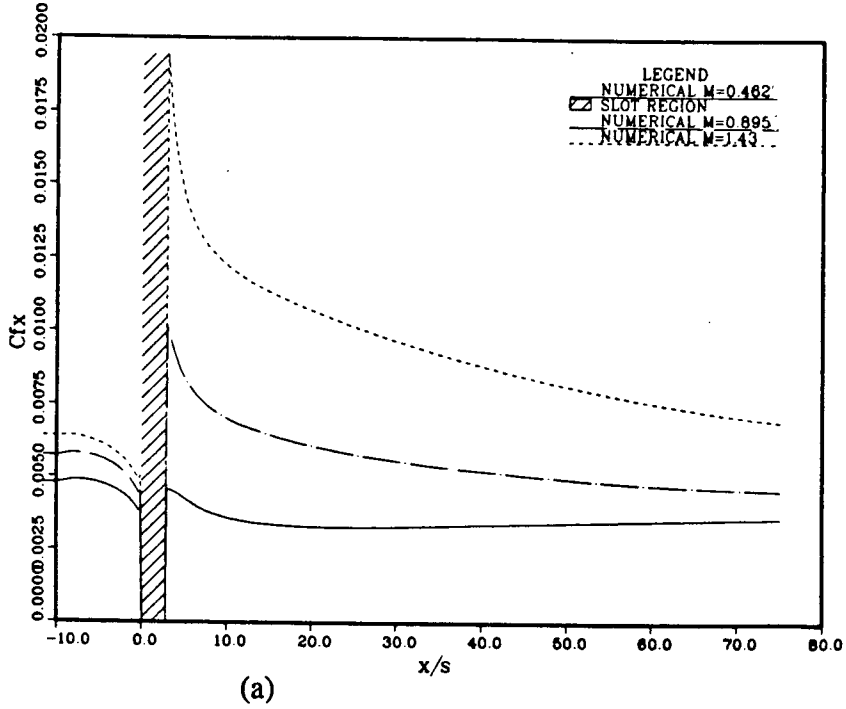


Figure 4.10 Shear Stress Coefficients for a) the 20 degree slot and b) the 40 degree slot

It is interesting to note from this figure that the zero pressure gradient condition for each flow case is re-established within 40 slot widths of the slot leading edge. The numerical shear stress coefficients in Figure 4.10 do not exhibit the sign change characteristic of separation. Furthermore the variation of shear stress downstream of the slot is similar, in form, to the development of shear stress along a flat plate in a zero pressure gradient boundary layer. The differences between the shear stresses upstream of the slot are a result of the various upstream velocity profiles used to produce the various mass flow ratios. It is interesting to note, from Figure 4.10, that the shear stress coefficient increases downstream of the slot for the low mass flow ratio cases. The reason for this behavior is not clear.

The sensitivity of the numerical results to the distribution of flow direction in the slot is examined with two types of non-uniform distributions. The distributions used here are outlined in section 3.2.2. In the following discussion, the results of calculations with the non-uniform distributions are compared with those using the uniform distribution. The linear-uniform distribution is expected to cause changes in the numerical result due to its more accurate representation of the slot mass flow. Other than adjusting the mass flow, this distribution does little to alter the nature of the flow direction in the slot. This point is clarified by Table 4.2 where β_{\max} refers to the maximum, uniform flow angle assigned in the linear-uniform distribution.

TABLE 4.2 Table of Values of β_{\max} for the Linear-Uniform Distribution of Flow Angle

Case Number	Slot Angle (deg)	β_{\max} (deg)	Extent of slot Covered by Uniform Region (percent)
201-LU	20	17.92	84.3
203-LU	20	23.48	95.9
401-LU	40	32.99	79.2
403-LU	40	39.07	79.2

The values of β_{\max} given in Table 4.2 reflect the qualitative flow behavior observed in the flow visualization of section 2.3.4.

The linear-uniform-linear distribution of the flow direction is expected to have two effects on the flow field predictions. Accurate representation of the mass flow from the slot should have an effect similar to that of the linear-uniform case. Forcing the flow angle to zero at the trailing edge, in effect, removes the possibility of separation from the numerical calculations. This latter effect is only expected to be significant for cases of high mass flow ratio, i.e. strong slot flow. Table 4.3 clarifies the differences between the linear-uniform and linear-uniform-linear distributions.

Table 4.3 Table of Values of β_{\max} for the Linear-Uniform-Linear Distribution of Flow Angle

Case Number	Slot Angle (deg)	β_{\max} (deg)	Extent of Slot Covered by Uniform Region (percent)
201-LUL	20	22.06	77.2
203-LUL	20	24.84	92.4
401-LUL	40	55.69	64.9
403-LUL	40	47.54	72.7

The velocity profile predicted at the slot trailing edge is shown in Figures 4.11 and 4.12 for comparison of cases 201-U, 201-LU, 201-LUL, 203-U, 203-LU, 203-LUL, 401-U, 401-LU, 401-LUL, 403-U, 403-LU, 403-LUL, (hereto referred to as the variants of cases 201, 203, 401 and 403). Each of the '-U' cases, except for case 403-U, corresponds to a case where the slot mass flow is inaccurately represented with the uniform flow angle assumption.

Regarding Figure 4.11, the various distributions of flow direction do not affect the predictions for case 201. The various distributions of flow direction do have an effect on the velocity predictions for the higher mass flow ratio of 1.4, i.e. case 203. For this case, each of the calculations with non-uniform flow angles in the slot predict velocities 10 percent higher than the same calculations with a uniform flow angle in the slot. Since both non-uniform distributions result in essentially the same prediction, the 10 percent increase can be attributed to more accurate representation of the slot mass flow.

Figure 4.12 illustrates similar behavior for the 40 degree slot. The results for case 401 indicate that, overall, the various distributions of flow angle have little effect on the calculated result.

Very close to the wall, however, differences up to 5 percent can be seen. These differences are not significant, but indicate some sensitivity to the direction of flow in the slot. The results for case 403 are also shown in Figure 4.12. These velocity predictions indicate that assumption of a linear-uniform distribution of flow angle has negligible effect for this case. This observation is reasonable considering the value of β_{\max} in Table 4.2 is only 0.93 degrees different from the slot angle itself. For this situation, essentially no difference exists between the uniform and linear-uniform distributions of flow angle. As a result, the boundary conditions and solutions are the same for these two cases. The velocity predictions near the wall for the linear-uniform-linear distribution, (case

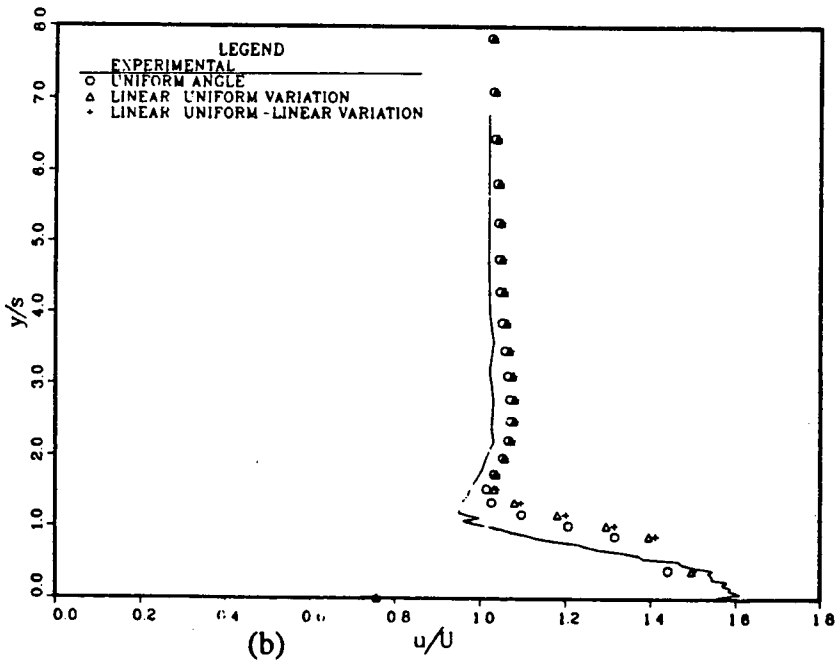
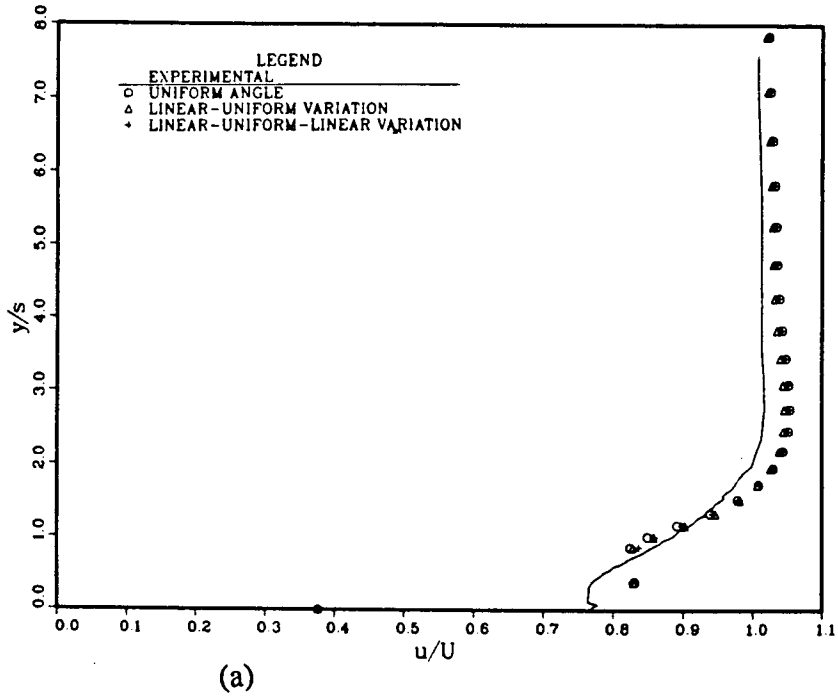


Figure 4.11 Comparison of the Mean Speed Profiles at the Slot Trailing Edge for Three Flow Angle Distributions, $\alpha = 20$ degrees and a) $M=0.4622$, (case 201) and b) $M=1.430$, (case 203)

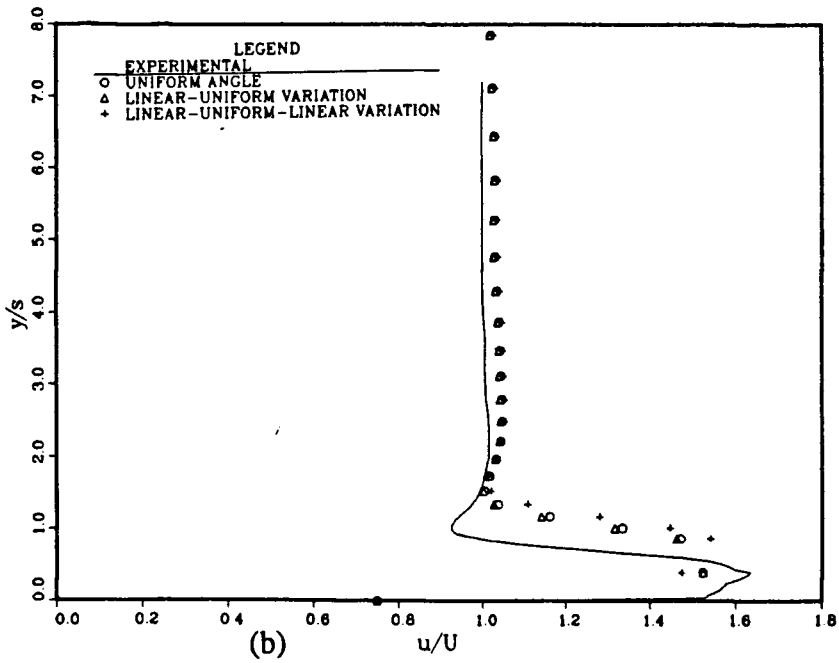
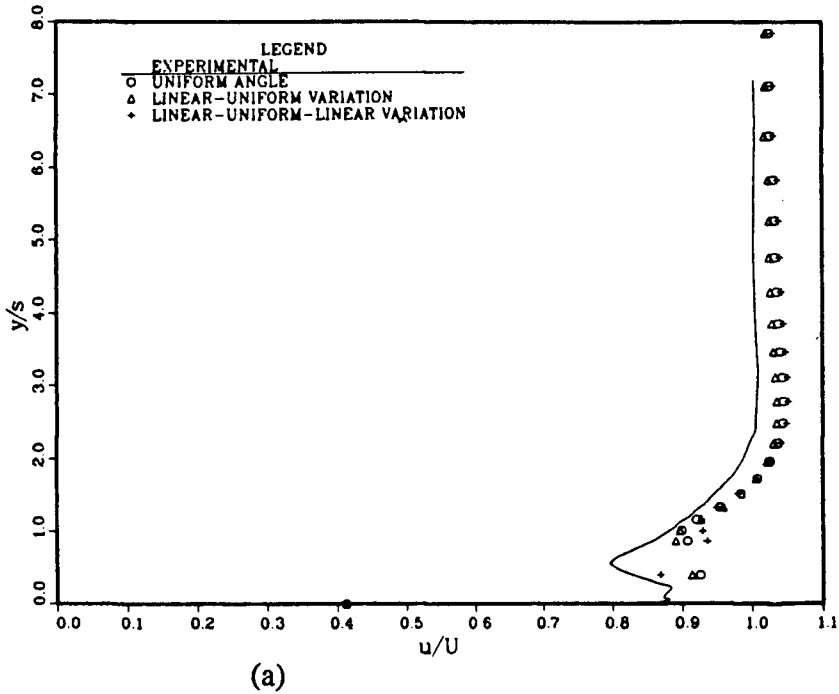


Figure 4.12 Comparison of the Mean Speed Profiles at the Slot Trailing Edge for Three Flow Angle Distributions, $\alpha = 40$ degrees and
 a) $M = 0.4616$, (case 401) b) $M = 1.239$, (case 403)

403-LUL), however, are from 3 to 8 percent different from the predictions which use the uniform flow angle distribution (case 403-U).

The differences in each of the numerical results follow the trend expected for the various flow angle distributions. The velocity predictions do not, however, seem to be as sensitive to these distributions as first thought. Differences of 10 percent between various numerical solutions do not seem large when the corresponding experimental measurements differ from the numerical solutions by, as much as, 40 to 50 percent in some places.

Figures 4.13 and 4.14 illustrate the surface pressure coefficients for the variants of cases 201, 203, 401 and 403. The largest difference between two pressure coefficients is less than 5 percent. This small difference again suggests an insensitivity of the predictions to the assumed small changes in flow direction within the slot.

Although the predictions of velocity are quite insensitive to the flow direction assumed in the slot, the shear stress coefficients are, in some cases, very sensitive to this flow direction. This fact is illustrated by Figures 4.15 and 4.16 for the variants of cases 201, 203, 401 and 403. The differences in shear stress upstream of the slot in these figures are due to differences in the upstream flow conditions used to set the mass flow ratios. The results of Figure 4.15a show little more than a 10 percent effect on shear stress for case 201. No effect is apparent for case 203. The results of Figure 4.16, on the other hand, indicate changes in wall shear stress of 60 to 80 percent downstream of the slot trailing edge. Presumably, the precise flow velocity close to the plate has a strong effect on the wall stress so that this quantity is most affected by the assumed flow direction in the slot. This observation may have important implications for the heat transfer predictions downstream of the slot. The experimental points shown in Figure 4.16, obtained from the velocity profiles using Clauser plots, provide an initial estimate

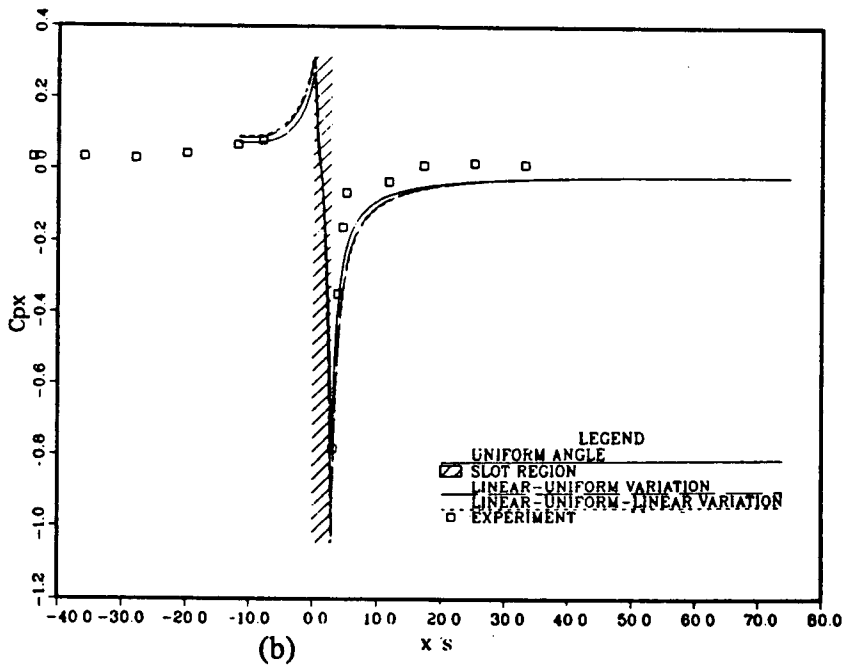
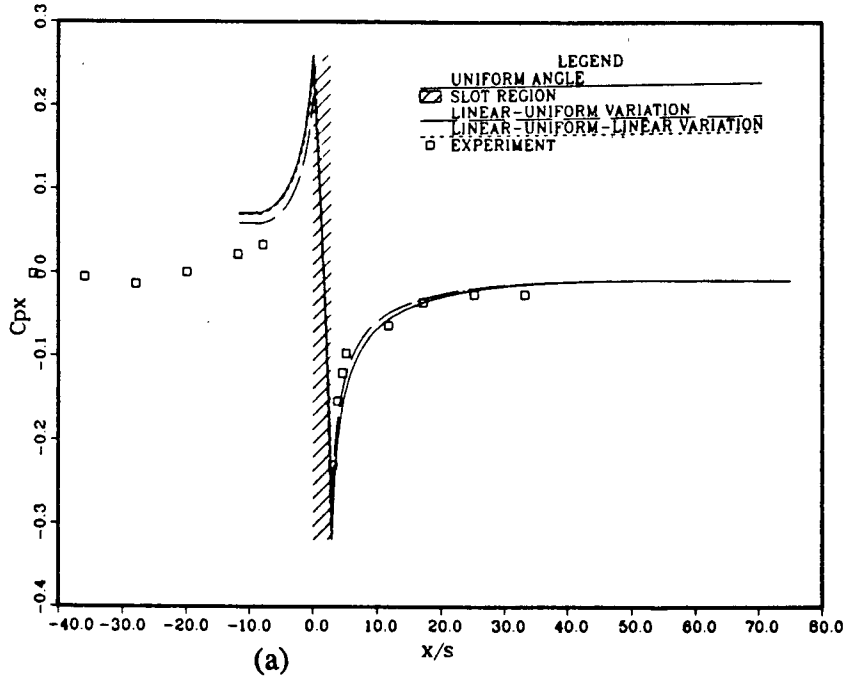


Figure 4.13 Comparison of Surface Pressure Coefficients for Three Flow Angle Distributions, $\alpha = 20$ degrees and a) $M = 0.4622$, (case 201) b) $M = 1.430$, (case 203)

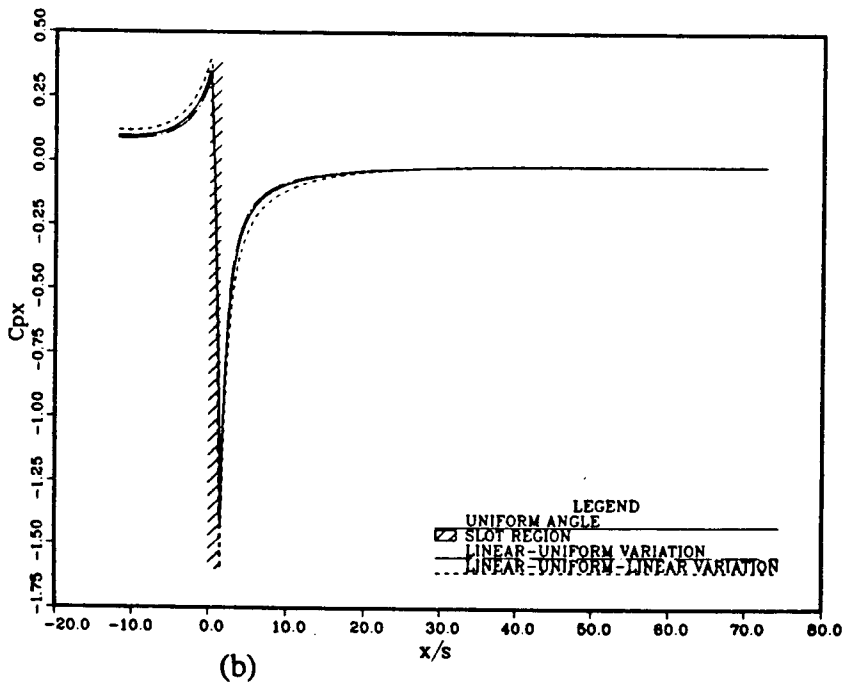
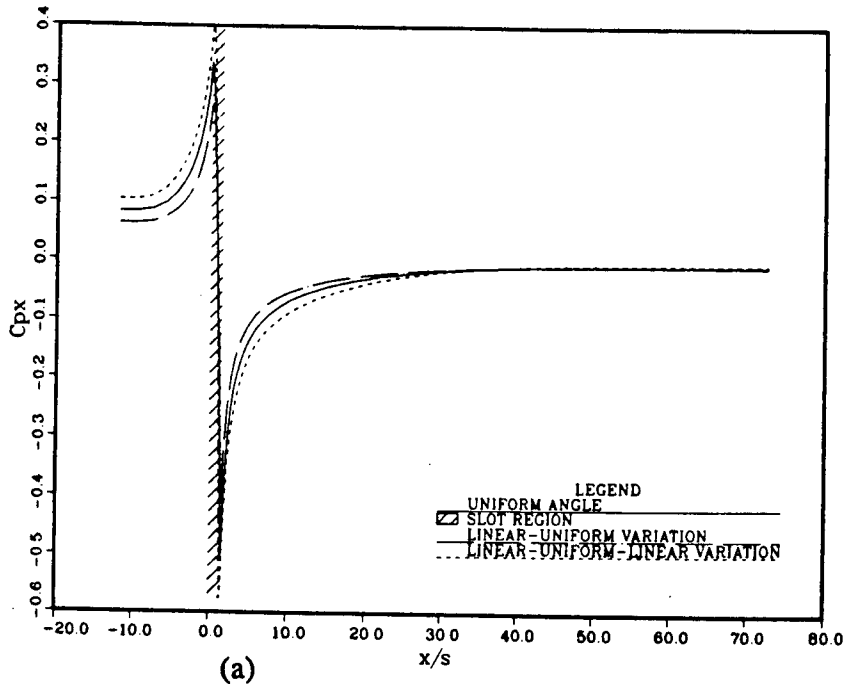


Figure 4.14 Comparison of Surface Pressure Coefficients for Three Flow Angle Distributions, $\alpha = 40$ degrees and a) $M = 0.4616$, (case 401) b) $M = 1.239$, (case 403)

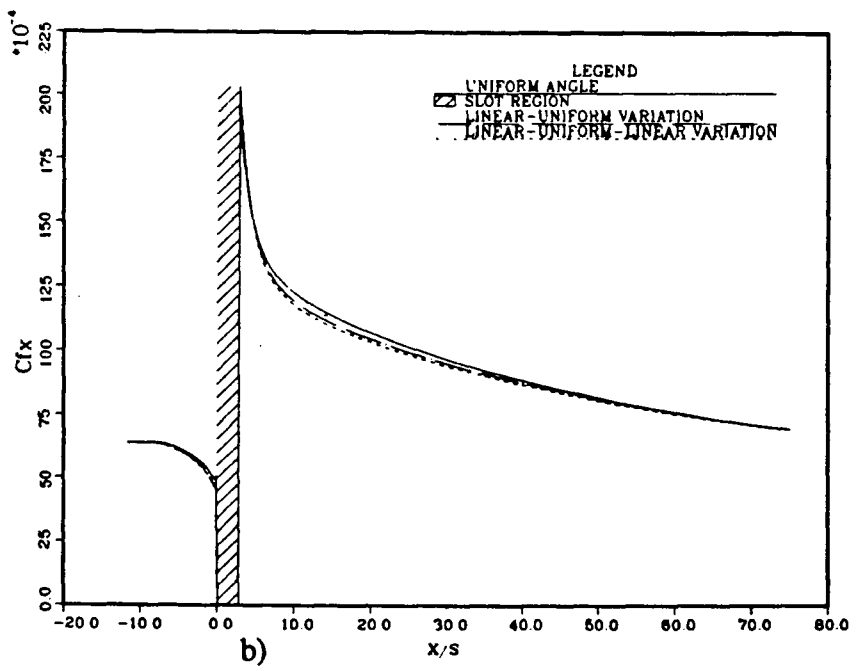
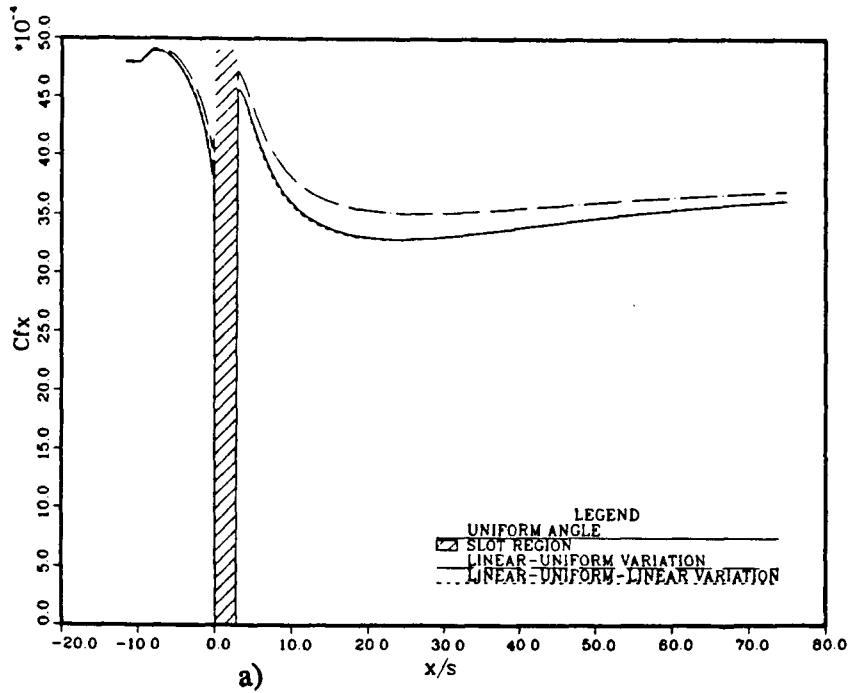


Figure 4.15 Comparison of Shear Stress Coefficients for Three Flow Angle Distributions, $\alpha = 20$ degrees and a) $M = 0.4622$, (case 201) b) $M = 1.430$, (case 203)

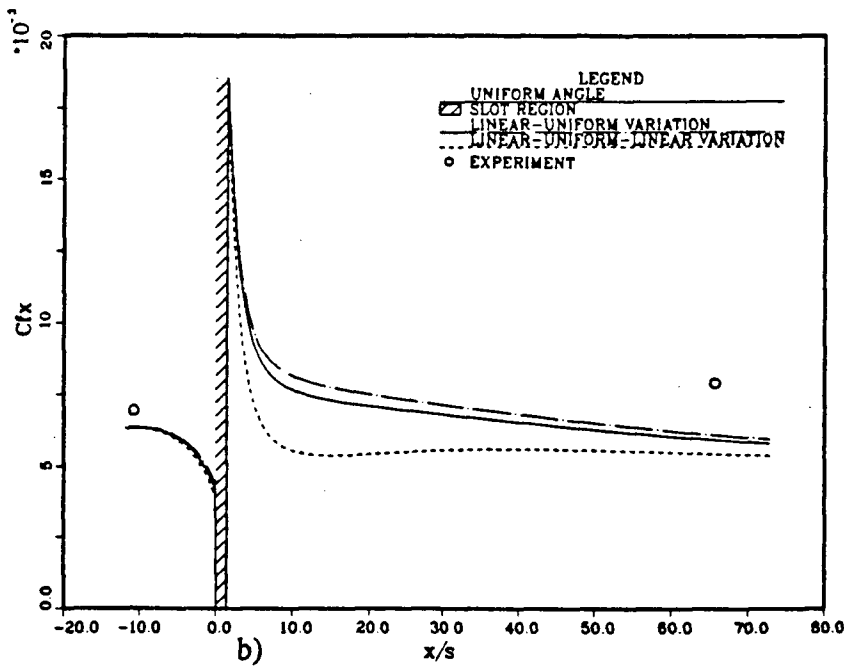
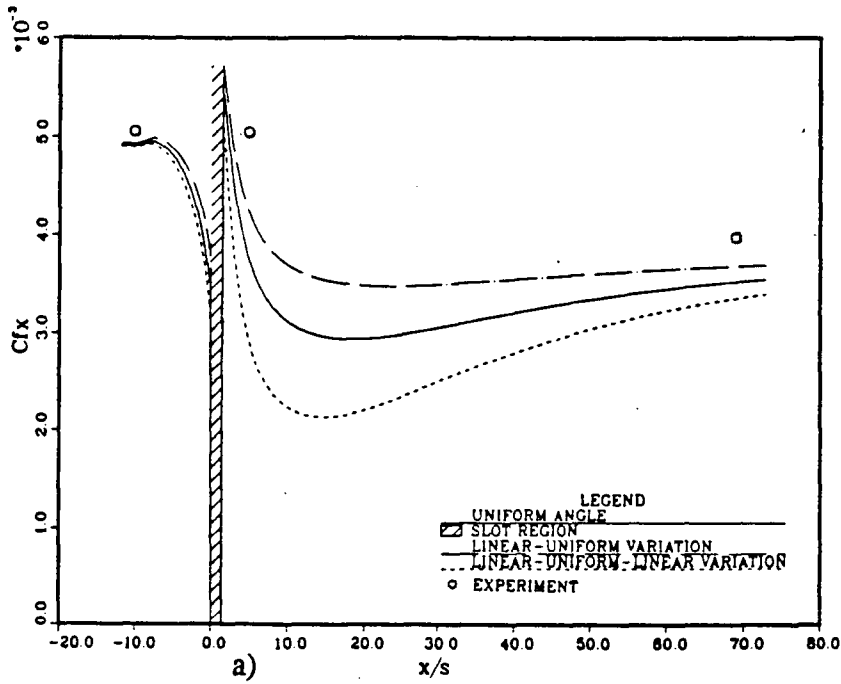


Figure 4.16 Comparison of Shear Stress Coefficients for Three Flow Angle Distributions, $\alpha = 40$ degrees and a) $M = 0.4616$, (case 401) b) $M = 1.239$, (case 403)

of the quality of prediction of the wall shear stress. These points indicate that the wall shear stress is reasonably predicted upstream and well downstream of the slot. Detailed measurements of wall shear stress should be made to allow a better comparison of the numerical and experimental results.

4.2.2 The Thermal Field

In this section, some preliminary temperature and heat transfer results are presented and discussed. Although experimental results are not available for comparison, a qualitative discussion of the numerical results sheds some light on heat transfer behavior in a film cooling situation.

The numerical results presented here represent the case of a secondary coolant stream injected into a hot primary stream. The solid wall is assumed to have a uniform temperature. The coolant and wall temperatures are 298.0 K. The freestream temperature is 304.0 K. The flow fields correspond to those discussed in the preceding section. Since the ratio of $Gr_x/(Re_x)^2$ is 0.00101 downstream of the slot, buoyancy effects are neglected in the numerical model.

Figure 4.17 presents the streamwise development of typical temperature profiles for the cases 202-U and 402-U. The temperature profiles are shown to develop slowly downstream of the slot trailing edge. The temperature profiles shown in Figure 4.18, for cases 201-U, 202-U, 203-U, 401-U, 402-U and 403-U, illustrate the effect of several mass flow ratios on the temperature profile at the slot trailing edge. An interesting feature of these profiles is their slope near the wall. One would expect the slope, dT/dy , in this region to be zero because the coolant injected over the wall has the same temperature as the wall. However, it appears that turbulent mixing of the two streams

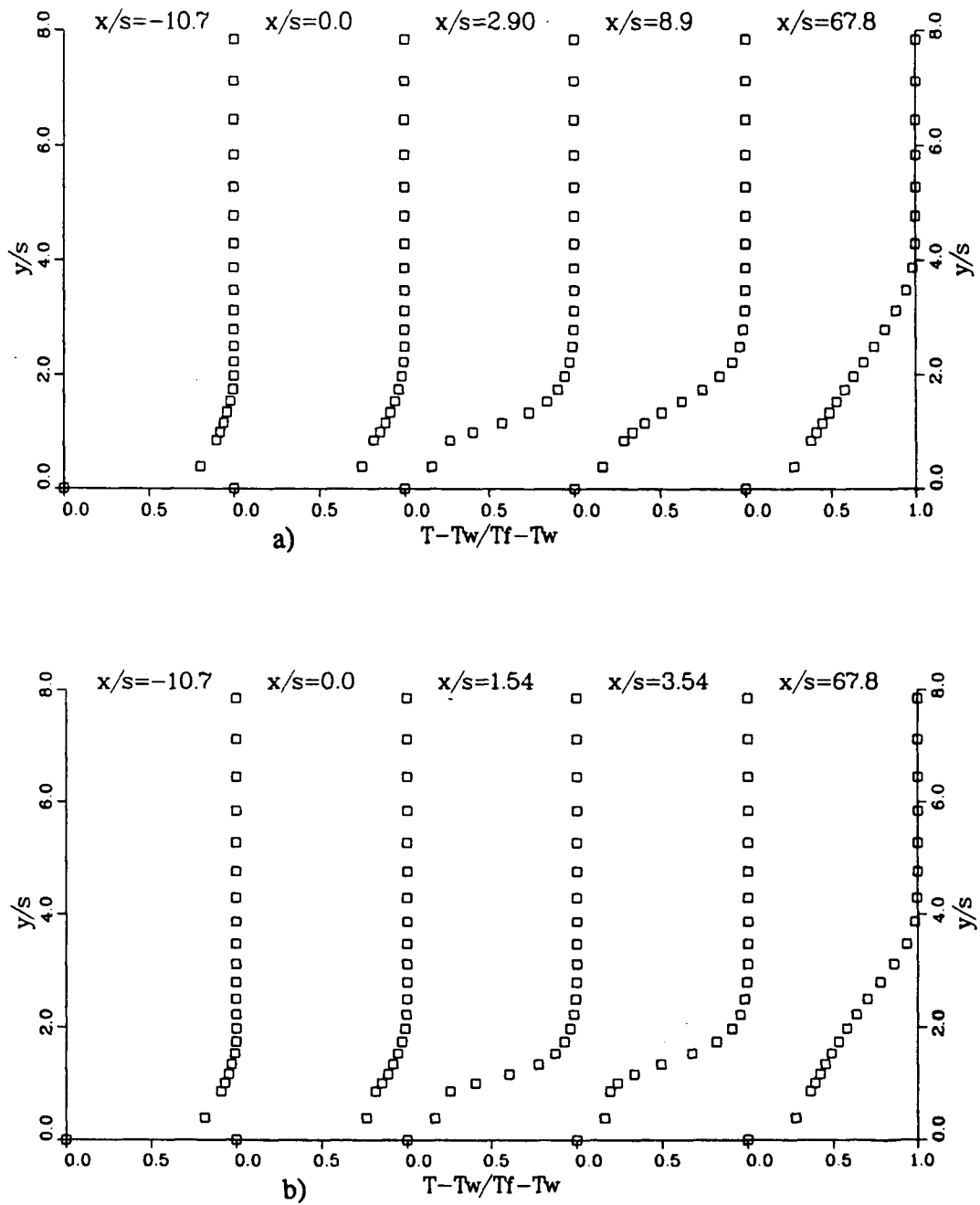


Figure 4.17 Typical Streamwise Development of the Temperature Profiles for
 a) $\alpha = 20$ degrees and $M = 0.8955$, (case 202-U)
 b) $\alpha = 40$ degrees and $M = 0.9194$, (case 402-U)

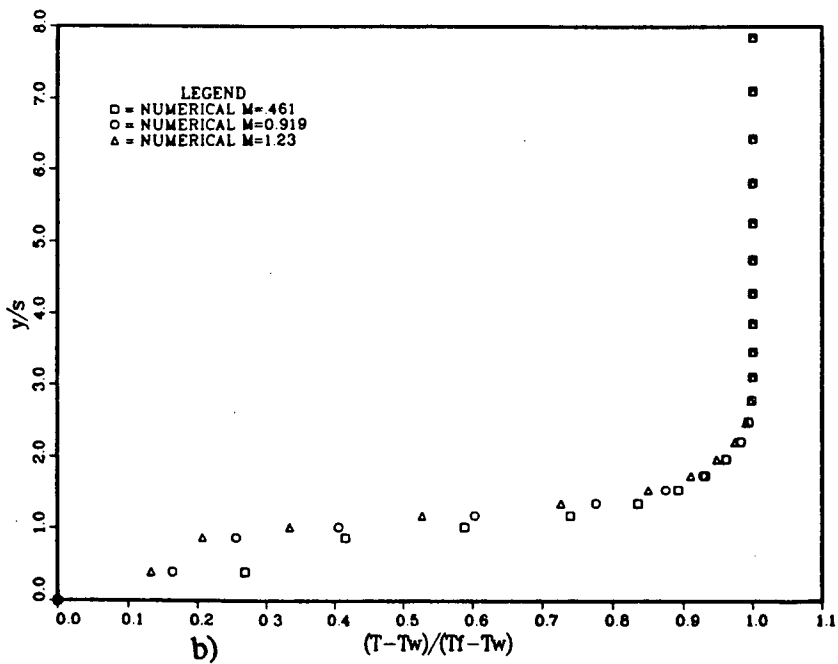
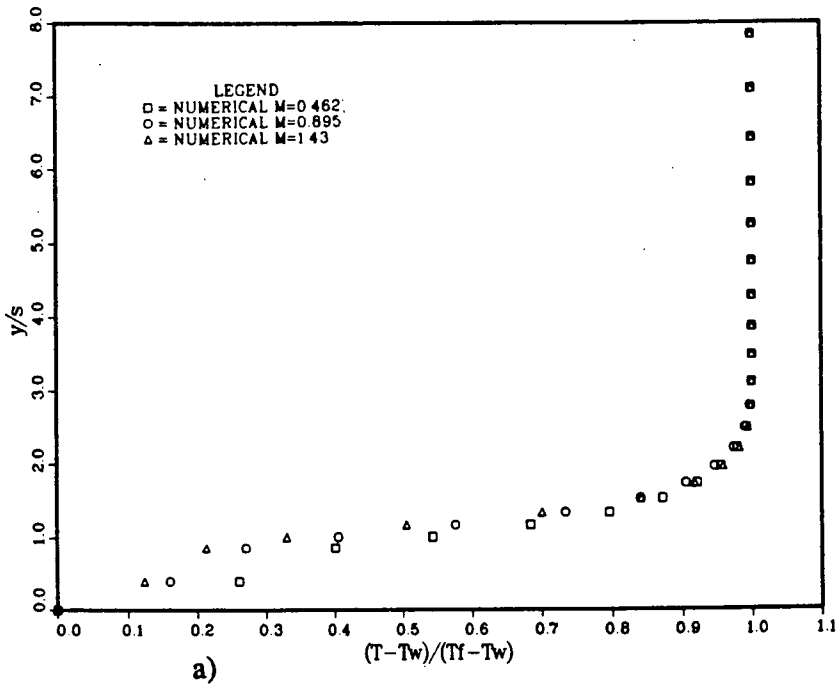


Figure 4.18 Comparison of Temperature Profiles at the Slot Trailing Edge for a) $\alpha = 20$ degrees and b) $\alpha = 40$ degrees

causes the fluid near the wall to adopt an intermediate temperature even at this point.

Figure 4.18 indicates that more of this mixing occurs for the smaller mass flow ratios. As a result, the lower mass flow ratio flows provide less thermal protection for the surface downstream of the injection slot.

The Stanton numbers shown in Figure 4.19 are defined as $q_w/(\rho C_p(T_w-T_f))$. The wall heat flux, q_w , is calculated from the temperature field results and equation 4.1 which use Reynold's analogy to extend the near wall model for momentum to the energy equation between the wall and the first computational cell.

$$q_w = \frac{\rho C_p^{1/4} k^{1/2} (h_w - h)}{\text{Pr}_i (9.24 ((\text{Pr}/\text{Pr}_i)^{3/4} - 1) (1 + 0.28 e^{-0.007 \text{Pr}/\text{Pr}_i}) + \text{Ln}(E y^+) / \kappa)} \quad (4.1)$$

The differences in the Stanton numbers upstream of the slot are due to differences in the inlet conditions of the various flow cases, namely 201-U, 202-U, 203-U, 401-U, 402-U and 403-U. It is interesting to note from this figure, for both slots, that the flow with the lowest mass flow ratio offers the least protection for the surface downstream of the slot. That is, the lowest mass flow rate through the slot corresponds to the highest wall heat flux. The Stanton number variation also shows the rate at which surface protection deteriorates. This rate is given by the slope of the Stanton number curve. For example, referring to Figure 4.19, the slope of the curve for the low mass flow ratio, through either slot, is much higher than the other slopes. This indicates that heat transfer to the surface downstream of the slot is increasing faster for the lower mass flow ratio.

Larger mass flow ratios do not necessarily provide more protection for the surface. This is evidenced in the near slot region, $x/s < 40$, of Figure 4.19. In this region, the heat flux for the largest mass flow ratio is predicted to be greater than or equal to that of the next lowest mass flow ratio. It is also interesting to note, in Figure 4.19, that the

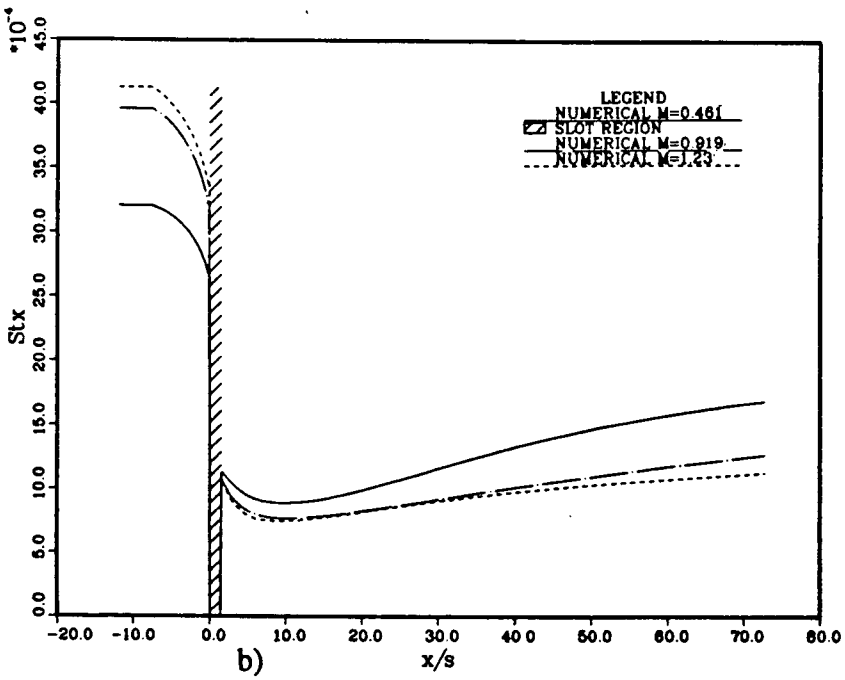
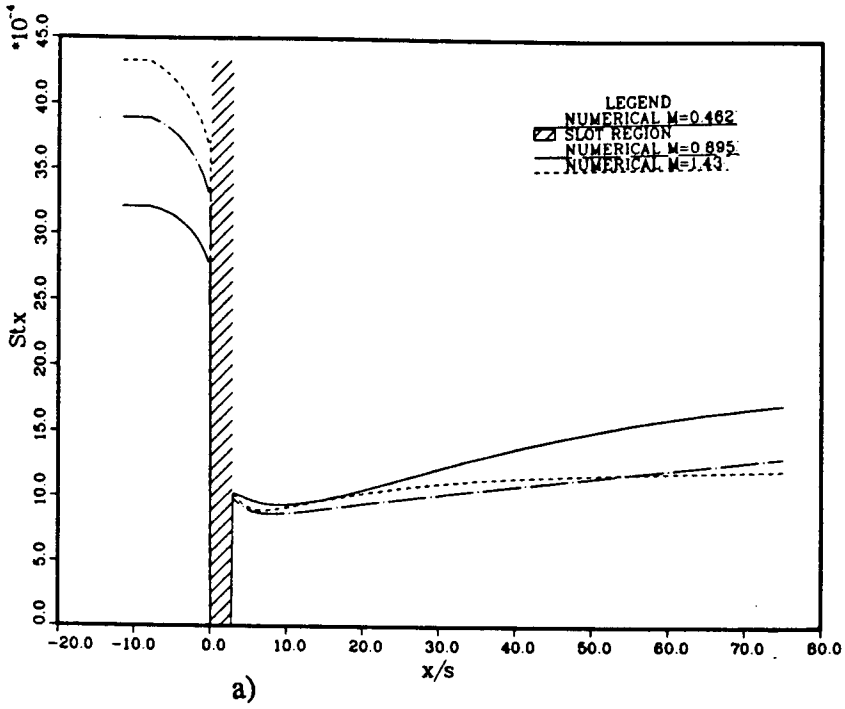


Figure 4.19 Comparison of Stanton Number Variation for a) $\alpha = 20$ degrees and b) $\alpha = 40$ degrees

Stanton number is essentially constant, downstream of the slot, for larger mass flow ratios. Similar qualitative behavior is noted, for full coverage film cooling flows, by Yavuzkurt and Moffat [35].

The preceding heat transfer results are calculated based on the assumption that flow exits the slot in a uniform direction equal to the slot angle. Figure 4.20 presents some heat transfer predictions corresponding to the flow fields of cases 401 and 403. The comparison here illuminates the effect of three different assumed distributions of flow direction in the slot. For the cases shown here, the effect on wall heat flux can be very significant. Small changes in the slot flow direction can cause changes of 80 to 100 percent in the wall heat flux downstream of injection. The magnitude of these effects indicates that close attention should be given to the determination of the flow distribution within cooling slots and orifices.

4.3 The Plenum-Mainstream Interaction

The objectives of this section are to illustrate and understand the plenum-mainstream interaction. Calculation of the flow behavior within and around the slot is important for several reasons. The results of sections 4.2.1 and 4.2.2 indicate that such a calculation may be necessary for the successful prediction of wall shear stresses and heat transfer rates downstream of injection. In the absence of measurements or calculations of flow angle within the slot, heat transfer predictions are likely to be inaccurate. Furthermore, calculation of the interaction between the plenum and mainstream flows helps to explain the experimentally observed behavior. This adds to the overall understanding of the physical nature of this flow.

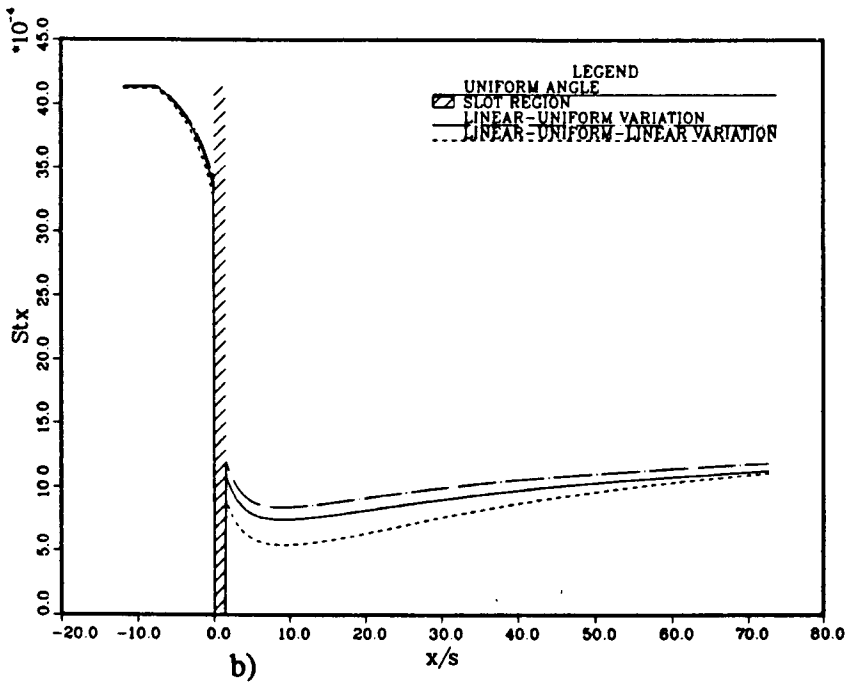
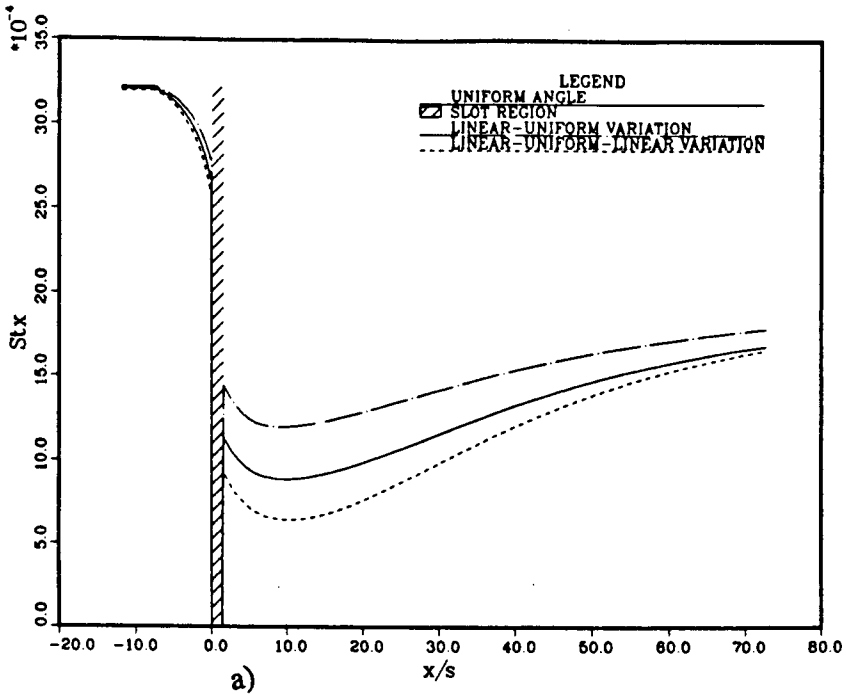


Figure 4.20 Comparison of Stanton Number Variation for Three Flow Angle Distributions for $\alpha = 40$ degrees and a) $M = 0.4616$, (case 401) b) $M = 1.239$, (case 403)

Preliminary results are presented here for the case of normal, (90 degree), injection. This case is examined, rather than an inclined slot, because of limitations in the computer code. A thorough study of the plenum-mainstream flow interaction is beyond the scope of the present research. Such a study is left for future work. As such, only information relevant to the interface behavior is given here.

The flow in question here is restricted to laminar, isothermal flow corresponding to a mass flow ratio of 0.4. Figure 4.21 clearly indicates the interaction between the two streams. Not shown in this figure is the velocity field within the plenum section. The calculation of the plenum flow field extends 0.8 slot widths into the plenum. The velocity boundary condition used in the plenum is that of a uniform velocity, V , parallel to the slot. It is interesting to note that the effect of the freestream interaction penetrates at least one slot diameter down into the slot.

The qualitative confirmation of the observed and predicted trends, in Figure 4.21, is reassuring. The vector field indicates that separation is not present in this solution. The lack of separation is probably due to the weakness of the slot flow, (low mass flow ratio), calculated here. Figure 4.22 shows the variation of the calculated mean speed at the slot exit. The trend in this figure is similar to that observed in section 2.3.2. Similarly, Figure 4.23 reflects the variation of flow direction at the slot exit (in the plane of the slot exit). It is interesting to note that the flow angle, β , varies across the exit plane, of the slot, from 5 to 60 degrees.

Future work may entail a calculation of this type for the cases of section 4.2. Such a calculation could be enlightening in that it has the potential to remove some of the disagreement between experimental and numerical results noted in section 4.2.

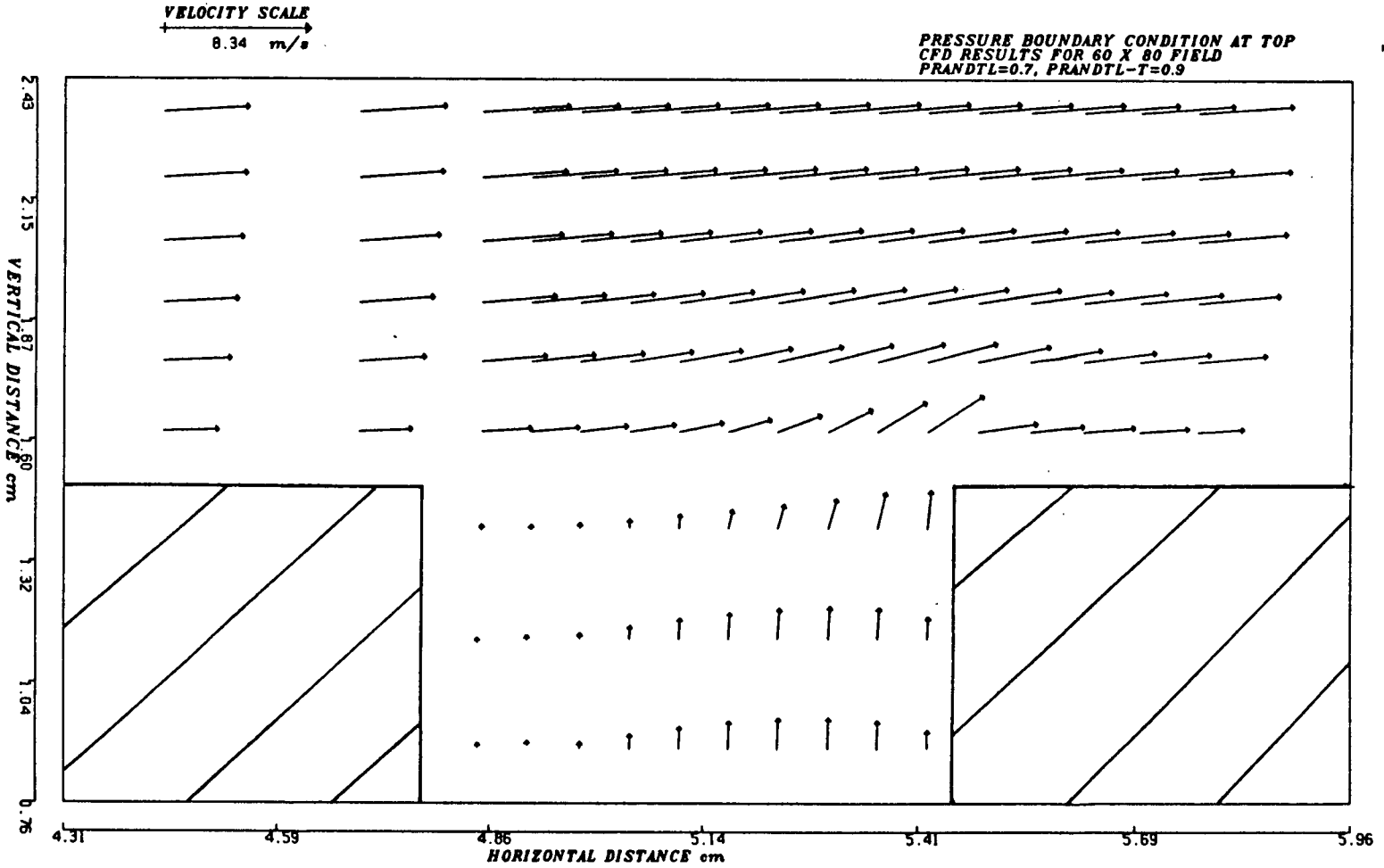


Figure 4.21 Vector Field Showing the Predicted Variation of Magnitude and Direction of the Velocity at the Interface

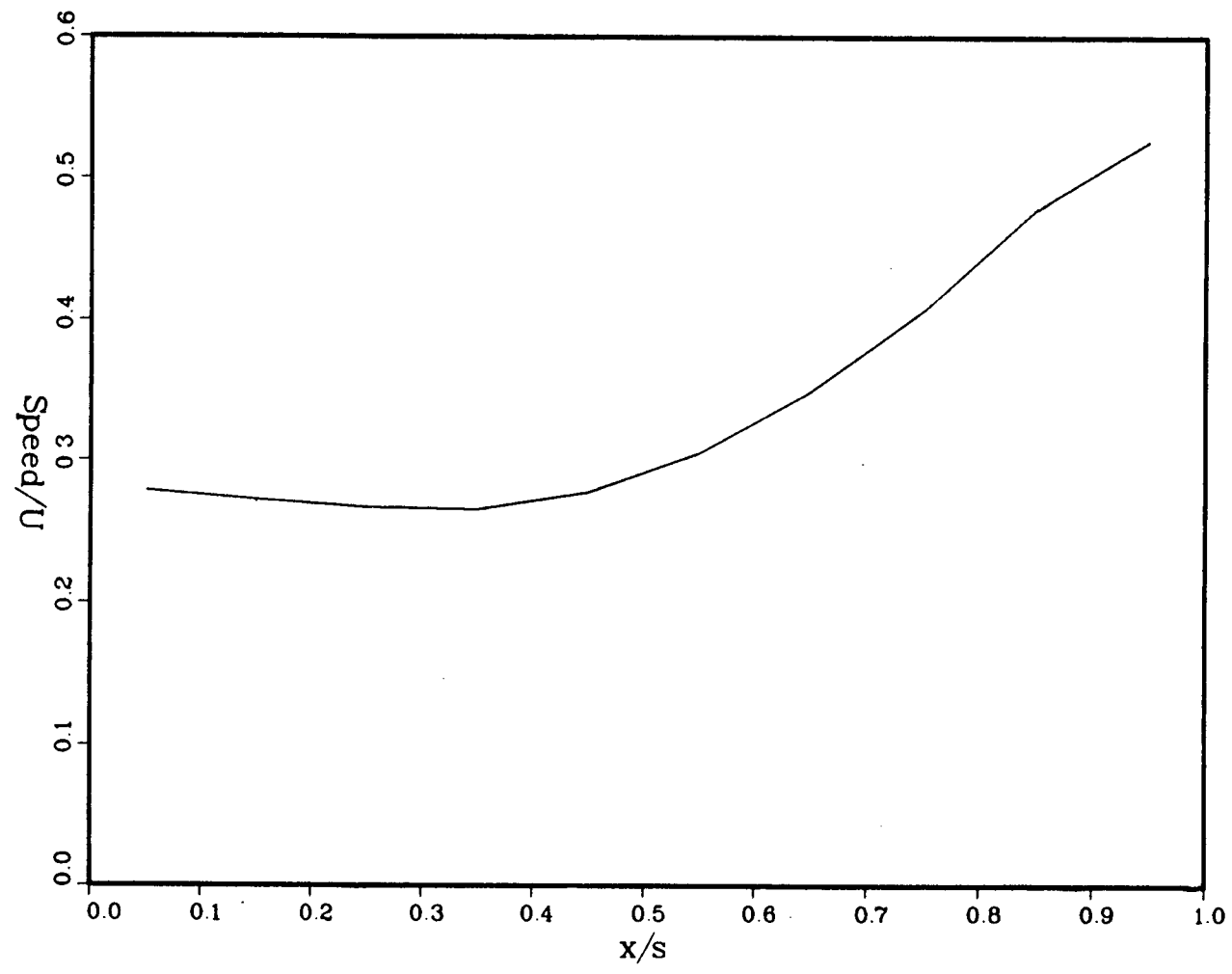


Figure 4.22 Predicted Speed Variation Across the Slot for Normal Injection and $M = 0.4$

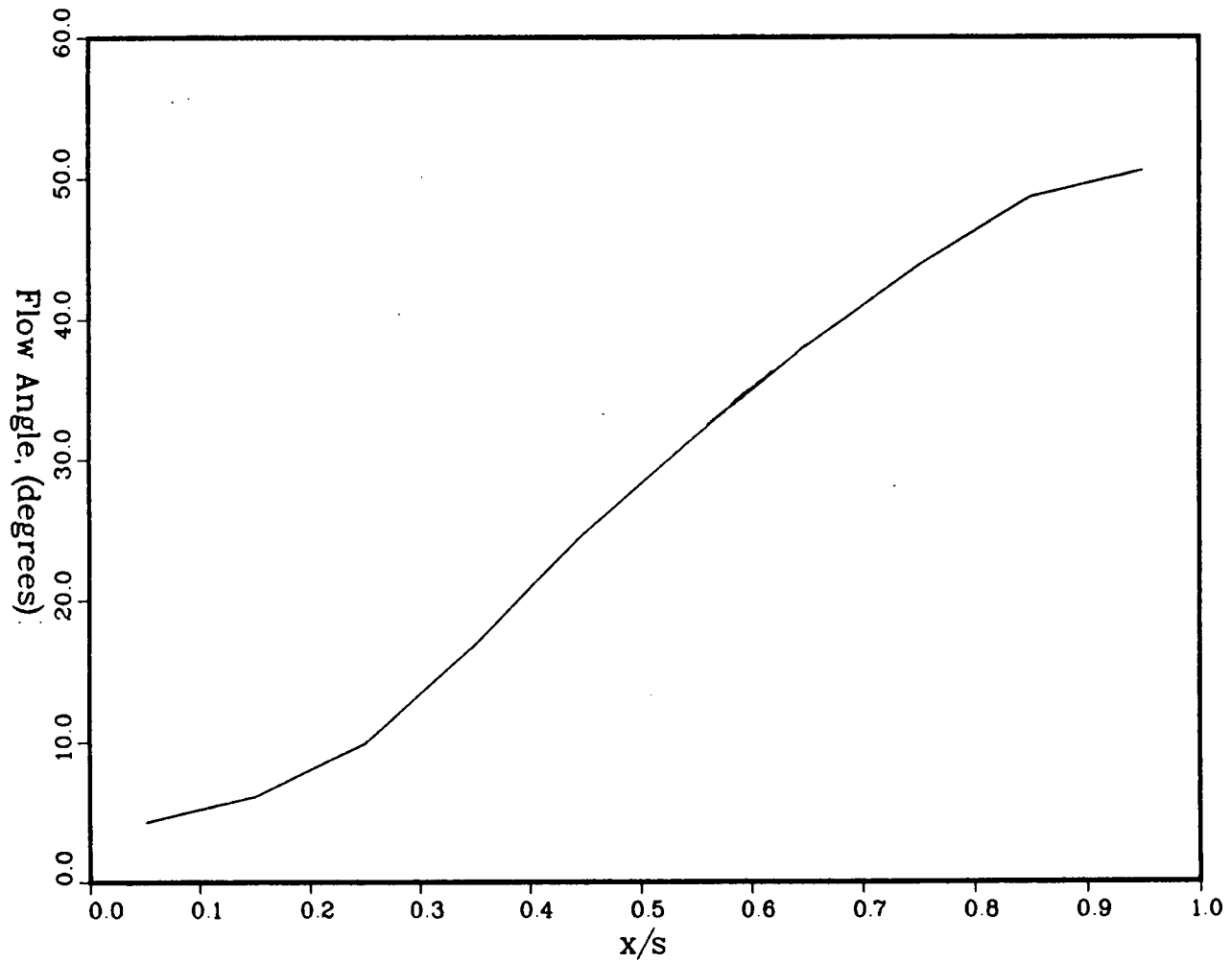


Figure 4.23 Predicted Distribution of Flow Angle for Normal Injection and $M = 0.4$

5.0 CONCLUSIONS

*"To see the world in a grain of sand
and a heaven in a wild flower, hold
infinity in the palm of your hand and
eternity in an hour."*

William Blake

The numerical and experimental work undertaken by this project has answered several fundamental questions. In addition, several questions have been raised from which further film cooling studies can grow.

Physical understanding of the flow is provided for a range of geometries and flow conditions relevant to film cooling flows. The flow from the flush inclined slot was observed to exhibit many interesting features. Hot wire anemometer measurements of the speed profile across the slot indicate that the majority of fluid leaving the slot does so from the downstream portion of the slot. Non-uniformity of the direction of the velocity vectors at the slot exit is inferred from integration of the slot speed profiles. Furthermore, the extent of the observed and inferred non-uniformities depends on the relative strengths of the main and secondary streams.

The deviation of the average flow angle from the slot angle is examined qualitatively. Flow visualization and measurements indicate, quite clearly, that weak slot flows, (low mass flow ratio), are significantly blown towards the downstream end of the slot region. Increasing the mass flow ratio appears to have the effect of decreased mixing of the main and secondary streams. This statement is based on the observation that the

speed profile across the slot becomes more uniform for higher mass flow ratios. This indicates that less flow is blown to the downstream portion of the slot which, in turn, indicates a smaller streamwise velocity component. Flow visualization confirms this behavior.

Detailed measurements of the streamwise speed profile development indicate a behavior roughly analogous to a wall jet. That is, the flow immediately downstream of the slot has high momentum near the wall which is gradually diffused and convected into the mainstream as the flow makes its way downstream. This analogy is best applied to the measurements for the 20 degree slot geometry. The velocity profiles for the 40 degree geometry show that the point of maximum velocity is raised off the surface for a certain distance downstream of injection. This indicates that the flow leaves the 40 degree slot in a fairly distinct jet. The jet gradually dissipates farther downstream of the slot and the flow develops in a way roughly similar to that of the wall jet.

The numerical calculations presented herein represent an improvement over practices in the literature because the measured speed profiles are incorporated. The predictions are in qualitative agreement with the experimental measurements. Quantitatively, only the predictions for the 20 degree geometry are in good agreement with the measurements. The reason for the disagreement between results for the 40 degree case is not clear. Poor numerical resolution of the near wall region may be at fault. The flow may also be sufficiently different from a boundary layer flow such that the near wall model is not applicable.

A great deal of effort was spent to examine the significance of flow direction at the plenum-mainstream interface. The calculations, for three different profiles of flow direction, indicate that flow direction does not have a large effect on the flow field downstream of injection and away from the wall. The flow direction can, however, have a large effect on the shear stress coefficient and the Stanton number. Preliminary heat

transfer calculations indicate changes of 80 to 100 percent in the wall heat flux for small changes in the assumed flow direction in the slot. This observation points to the significance of this work as it relates to film cooling predictions.

Calculation of the flow from the plenum, through the slot and into the mainstream indicates qualitative agreement with experimentally observed trends. This result is encouraging because it shows the potential for predicting complicated film cooling flow interactions.

6.0 RECOMMENDATIONS

Many questions have been raised during the course of this research. Some have been answered, but many remain. Some suggestions for future work are given here.

1. Recalibrate the rotameter used in these experiments to check the values quoted in this thesis. If a systematic error is confirmed, recalculate the numerical results, with corrected values of the mass flow ratio, for comparison with the experimental results. Little qualitative difference is expected from this possible change, but the effects need to be examined for detailed improvements in the comparisons.
2. Create and measure temperature fields and wall heat fluxes for the set of flows studied here. Temperature measurements complementing a detailed set of flow measurements are not found in the literature.
3. Perform numerical work to predict the measurements of temperature and Stanton number. This work should include the plenum-mainstream interaction to account for the flow direction in the slot.
4. Conduct experiments to measure the direction of flow exiting the slot for the cases examined in this study and recalculate the flow field for the cases presented here.

5. Measure the variation of wall shear stress for the cases presented here and compare the results with the calculated shear stresses.
6. The numerical model presented here for the flush, inclined slot should be improved to accurately predict the flow for the 40 degree geometry. This might include low Reynolds number models in the near wall region.
7. The effect of altering the slot length to width ratio should be examined in detail.
8. Use the plenum module with a variety of geometries, eg. curved floors, to simulate the geometric effects of the various surfaces of film cooled turbine blades.
9. Repeat the present study for favourable and adverse pressure gradients to simulate pressure conditions occurring on the surface of actual turbine blades.

REFERENCES

1. Koppers K.H., "Temperaturmessungen an zwei wendigen Gasturbinen - Schaufelprofilen mit Grenzschichtkühlung", DVL-St.-Bericht Nr 82, 1944.
2. Liess, C. and Carnel, J., "Application of Film Cooling to Gas-Turbine Blades", AGARD Conference Proceedings, No. 73, pp. 23-1 to 23-9, Sept. 1970.
3. Kacker, S.C., Pai, B.R. and Whitelaw, J.H., "The Prediction of Wall Jet Flows with Particular Reference to Film Cooling", Progress in Heat and Mass Transfer, Vol. 2, pp. 163-186, MacMillan (Permagon), New York, 1969.
4. Goldstein, R.J., "Film Cooling", Advances in Heat Transfer, Vol. 7, pp. 321-377, 1971.
5. Dixon, S.L., Fluid Mechanics, Thermodynamics of Turbomachinery, Permagon Press, Oxford, 1982.
6. Lander, R., Fish, R. and Suo, M., "External Heat Transfer Distribution on Film Cooled Turbine Vanes", J. Aircraft, Vol. 5, No. 10, pp. 707-714, October 1972.
7. Kiock, R., Hoheisel, H., Dietrichs, H.J. and Holmes, A.T., "The Boundary Layer Behaviour of an Advanced Gas Turbine Rotor Blade Under the Influence of Simulated Film Cooling", AGARD Conference Proceedings (No. 42).
8. McDonald, H. and Fish, R.W., "Practical Calculations of Transitional Boundary Layers", Int. J. of Heat and Mass Transfer, Vol. 16, pp. 1729-1744, 1973.
9. Crane, R.I., Leontsakos, G. and Sabzuari, J., "Transition in Pressure Surface Boundary Layers", J. of Turbomachinery, Vol. 109, pp. 296-302, April 1987.
10. Rodi, W. and Scheuerer, G., "Calculation of Laminar-Turbulent Boundary Layer Transition on Turbine Blades", AGARD Conference Proceedings-390, May 1985, pp. 18-1 to 18-13.
11. Hoheisel, H., Kiock, R., Lichtfuss, H.J., and Fottner, L., "Influence of Free-Stream Turbulence and Blade Pressure Gradient on Boundary Layer and Loss Behaviour of Turbine Cascades", J. of Turbomachinery, Vol. 109, pp. 210-219, April 1987.
12. Hay, N., Lampard, D. and Saluja, C.L., "Effects of the Condition of the Approach Boundary Layer and of Mainstream Pressure Gradients on the Heat Transfer Coefficient on Film Cooled Surfaces", J. of Engineering for Gas Turbines and Power, Vol. 107, pp. 99-104, January 1985.

13. Kuhl, W., "Investigations on the Local Heat Transfer Coefficient of a Convection Cooled Rotor Blade", AGARD Conference Proceedings (No. 7).
14. Pedersen, D.R., Eckert, E.R.G., and Goldstein, R.J., "Film Cooling with Large Density Differences Between the Mainstream and the Secondary Fluid Measured by the Heat-Mass Transfer Analogy", J. of Heat Transfer, Vol. 99, pp. 620-627, November 1977.
15. Forth, C.J.P., Loftus, P.J. and Jones, T.V., "The Effect of Density Ratio on the Film Cooling of a Flat Plate", AGARD Conference Proceedings (No. 10), May 1985.
16. Bayley, F.J. and Milligan, R.W., "The Effect of Free Stream Turbulence Upon Heat Transfer to Turbine Blading", AGARD Conference Proceedings (No. 37).
17. Kadotani, K. and Goldstein, R.J., "On the Nature of Jets Entering a Turbulent Flow Part A - Jet - Mainstream Interaction", J. of Engineering for Power, Vol. 10, pp. 459-465, July 1979.
18. Kadotani, K. and Goldstein, R.J., "On the Nature of Jets Entering a Turbulent Flow Part B - Film Cooling Performance", J. Engineering for Power, Vol. 101, pp. 466-470, July 1979.
19. Yavuzkurt, S., Moffat, R.J. and Kays, W.M., "Full Coverage Film Cooling - Part I. Three Dimensional Measurements of Turbulence Structure", J. Fluid Mech., Vol. 101, Part 1, pp. 129-158, 1980.
20. Anderson, O.L., "Calculation of Three Dimensional Boundary Layers on Rotating Turbine Blades", J. of Fluids Engineering, Vol. 109, pp. 41-50, March 1987.
21. Kikkawa, S. and Onkura, T., "Experimental and Theoretical Investigation on Three-Dimensional Film Cooling of a Flat Plate", Transactions of the JSME, Vol. 48, No. 426, pp. 325-332, 1982.
22. Rastogi, A.K. and Whitelaw, J.H., "The Effectiveness of Three Dimensional Film Cooling Slots - I. Measurements", Int. J. of Heat and Mass Transfer, Vol. 16, pp. 1665-1672, 1973.
23. Patankar, S.V., Rastogi, A.K., and Whitelaw, J.H., "The Effectiveness of Three Dimensional Film Cooling Slots - II. Predictions", Int. J. of Heat and Mass Transfer, Vol. 16, pp. 1673-1681, 1973.
24. Goldstein, R.J. and Chen, H.P., "Film Cooling on a Gas Turbine Blade Near the End Wall", J. of Engineering for Gas Turbines and Power, Vol. 107, pp. 117-122, January 1985.
25. Sivasegaram, S. and Whitelaw, J.H., "Film Cooling Slots: The Importance of Lip Thickness and Injection Angle", J. Mech. Eng. Sci., Vol. 11, pp. 22-27, 1969.
26. Papell, S.S., "Effect on Gaseous Film Cooling of Coolant Injection Through Angled Slots and Normal Holes", NASA TND-299, 1960.

27. Metzger, D.E., Carper, H.J. and Swank, L.R., "Heat Transfer With Film Cooling Near Nontangential Injection Slots", *Journal of Engineering for Power*, Vol. 90, pp. 157-163, 1968.
28. Metzger, D.E., Biddle, J.R. and Warren, J.M., "Evaluation of Film Cooling Performance on Gas Turbine Surfaces", AGARD Conference Proceedings High Temperature Gas Turbines, AGARD CP 73, Sept. 1970.
29. Mayle, R.E., Kopper, F.C., Blair, M.F. and Bailey, D.A., "Effect of Streamline Curvature on Film Cooling", *Journal of Engineering for Power*, Vol. 8, pp. 77-82, 1977.
30. Ko, Shao-Yan and Liu, Deng-Ying, "Experimental Investigations on Effectiveness, Heat Transfer Coefficient, and Turbulence of Film Cooling", *AIAA Journal*, Vol. 18, No. 8, pp. 907-913, 1980.
31. Bergeles, G., Gosman, A.D. and Launder, B.E., "The Turbulent Jet in a Cross Stream at Low Injection Rates: A Three-Dimensional Numerical Treatment", *Numerical Heat Transfer*, Vol. 1, pp. 217-242, 1978.
32. Bergeles, G., Gosman, A.D. and Launder, B.E., "The Prediction of Three Dimensional Discrete-Hole Cooling Processes: Part 1: Laminar Flow", *Journal of Heat Transfer*, Vol. 98, No. 3, pp. 379-386, 1976.
33. Bergeles, G., Gosman, A.D. and Launder, B.E., "The Prediction of Three Dimensional Discrete-Hole Cooling Processes: Part 2: Turbulent Flow", *Journal of Heat Transfer*, Vol. 103, pp. 141-145, 1981.
34. Demuren, A.O., Rodi, W. and Schonung, B., "Systematic Study of Film Cooling with a Three Dimensional Calculation Procedure", *Journal of Turbomachinery*, Vol. 108, pp. 124-130, 1986.
35. Yavuzkurt, S., Moffat, R.J. and Kays, W.M., "Full-Coverage Film Cooling, Part 2. Prediction of the Recovery Region Hydrodynamics", *Journal of Fluid Mechanics*, Vol. 101, Part 1, pp. 159-178, 1980.
36. Stewart, Capt. A.C., "An Investigation of Forebody Aerodynamics", M.A.Sc. Thesis, University of British Columbia, Vancouver, Canada, 1988.
37. Bradshaw, P., An Introduction to Turbulence and its Measurement, Pergamon Press, Oxford, 1975.
38. Pope, A. and Harper, J., Low Speed Wind Tunnel Testing, John Wiley and Sons, New York, 1966.
39. Merzkirch, W., Flow Visualization, Academic Press Inc., London, 1974.
40. Schlichting, H., Boundary-Layer Theory, 7th edition, McGraw-Hill, New York, 1979.

41. Glauert, M.B., "The Wall Jet", *Journal of Fluid Mechanics*, Vol. 1, Part 6, pp. 625-643, 1956.
42. Bird, R.B., Stewart, W.E. and Lightfoot, E.N., Transport Phenomena, John Wiley and Sons, New York, 1960.
43. Anderson, D.A., Tannehill, J.C. and Pletcher, R.H., Computational Fluid mechanics and Heat Transfer, Hemisphere Publishing Corporation, New York, 1984.
44. Kim, J., Moin, P. and Moser, R., "Turbulence Statistics in Fully Developed Channel Flow at Low Reynolds Number", *Journal of Fluid Mechanics*, Vol. 177, pp. 133-166, 1987.
45. Moin, P. and Kim, J., "The Structure of the Vorticity Field in Turbulent Channel Flow. Part 1. Analysis of Instantaneous Fields and Statistical Correlations", *Journal of Fluid Mechanics*, Vol. 155, pp.441-464, 1985.
46. Rodi, W., "Turbulence Models and Their Application in Hydraulics - A State of the Art Review", *Institute fur Hydromechanik, University of Karlsruhe, Karlsruhe, Federal Republic of Germany*, 2nd edition, 1984.
47. Reynolds, A.J., Turbulent Flows in Engineering, John-Wiley & Sons, London, 1974.
48. Hinze, J.O., Turbulence, 2nd edition, McGraw-Hill, New York, 1975.
49. Nallasamy, M., "Turbulence Models and Their Applications to the Prediction of Internal Flows: A Review", *Computers and Fluids*, Vol 15, No. 2, pp. 151-194, 1987.
50. Patel, V.C., Rodi, W. and Scheuerer, G., "Turbulence Models for Near-Wall and Low Reynolds Number FLOws: A Review", *AIAA Journal*, Vo. 2, No. 9, pp. 1308-1319, September 1985.
51. Hirata, M., Tanaka, H., Kawamura, H. and Kasagi, N., "Heat Transfer in Turbulent Flows", *Proceedings of the 7th International Heat Transfer Conference*, Vol. 1, pp. 31-57, 1982.
52. Jones, W.P. and Launder, B.E., "The Calculation of Low Reynolds Number Phenomena with a Two-Equation Model of Turbulence", *J. Heat Mass Transfer*, Vol. 16, pp. 1119-1130, 1972.
53. Blair, M.F., "The Effects of Freestream Turbulence on the Turbulence Structure and Heat Transfer in Zero Pressure Gradient Boundary Layers", *AFOSR TR-83-0149*, November, 1982.
54. Launder, B.E. and Spalding, D.B., "The Numerical Computation of Turbulent Flows", *Computer Methods in Applied Mechanics and Engineering*, Vol. 13, pp. 269-289, 1974.

55. Lai, K.Y.M., "Numerical Analysis of Fluid Transport Phenomena", Ph.D. Thesis, Imperial College (University of London), 1983.
56. Issa, R.I., "Solution of the Implicitly Discretized Fluid Flow Equations by Operator - Splitting", *Journal of Computational Physics*, Vol. 62, pp. 40-65, 1985.
57. Benodekar, R.W., Gosman, A.D. and Issa, R.I., "The TEACH-II Code for the Detailed Analysis of Two-Dimensional Turbulent Recirculating Flow", Department of Mechanical Engineering, Imperial College, Report FS/83/3, 1983.
58. Ideriah, F.J.K., "Turbulent Natural and Forced Convection in Plumes and Cavities", Ph.D. Thesis, Imperial College (University of London), 1977.
59. Raithby, G.D., "A Critical Evaluation of Upstream Differencing Applied to Problems Involving Fluid Flow", *Comp. Methods Appl. Mech. Engng.*, Vol. 9, pp. 75-103, 1976.
60. Benodekar, R.W., Goddard, A.J., Grosman, A.D., and Issa, R.I., "Numerical Prediction of Turbulent Flow Over Surface-Mounted Ribs", *AIAA Journal*, Vol. 23, No. 3, pp. 359-366, March 1985.
61. Leschziner, M.A. and Rodi, W., "Calculation of Annular and Twin Parallel Jets Using Various Discretization Schemes and Turbulence-Model Variations", *Journal of Fluids Engineering*, Vol. 103, pp. 352-360, 1981.
62. Snijders, A.L., Koppius, A.M. and Nieuwvelt, C., "An Experimental Determination of the turbulent Prandtl Number in the Inner Boundary Layer for Air Flow Over a Flat Plate", *Int. J. of Heat and Mass Transfer*, Vol. 26, No. 3, pp. 425-431, 1983
63. Eckert, E.R.G. and Drake, R.M., Analysis of Heat and Mass Transfer, Mc Graw-Hill, New York, 1972.

Appendix A

Reproduction of Table 4.1 for Easy Cross Reference of Cases

Table A.1

Reproduction of Table 4.1 for Easy
Cross-Reference of Cases

Case Number	Slot Angle	M_{num}	M_{expt}	Flow Angle Distribution
201-U	20	0.53	0.46	Uniform
201-LU	20	0.46	0.46	Linear-Uniform
201-LUL	20	0.46	0.46	Linear-Uniform-Linear
202-U	20	0.85	0.90	Uniform
203-U	20	1.23	1.4	Uniform
203-LU	20	1.43	1.4	Linear-Uniform
203-LUL	20	1.43	1.4	Linear-Uniform-Linear
401-U	40	0.56	0.46	Uniform
401-LU	40	0.46	0.46	Linear-Uniform
401-LUL	40	0.46	0.46	Linear-Uniform-Linear
402-U	40	0.97	0.91	Uniform
403-U	40	1.28	1.2	Uniform
403-LU	40	1.24	1.2	Linear-Uniform
403-LUL	40	1.24	1.2	Linear-Uniform-Linear